ABSTRACT

Title of dissertation:	LONGWAVE RADIATIVE TRANSFER THROUGH 3D CLOUD FIELDS: TESTING THE PROBABILITY OF CLEAR LINE OF SIGHT MODELS WITH THE ARM CLOUD OBSERVATIONS.
	Yingtao Ma, Doctor of Philosophy, 2004
Dissertation directed by:	Professor Robert G. Ellingson
	Department of Meteorology

Clouds play a key role in regulating the Earth's climate. Real cloud fields are non-uniform in both the morphological and microphysical sense. However, most climate models assume the clouds to be Plane-Parallel Horizontal (PPH) plates with homogeneous optical properties. Three characteristics of 3D clouds have been found to be important for longwave radiative transfer. They are: (1) the 3D geometrical structure of the cloud fields, (2) the horizontal variation of cloud optical depth, and (3) the vertical variation of cloud temperature. One way to incorporate the 3D geometrical effect in climate studies is through the use of an effective cloud faction, for which a major component is the Probability of Clear Line Of Sight (PCLOS). The PCLOS also plays an important role in accounting for longwave 3D effects caused by variable cloud

optical depth and vertical change of cloud temperature.

Aimed at improving the parameterization of longwave radiative transfer through 3D clouds, this study formulated a set of PCLOS models and tested the models with the Atmospheric Radiation Measurement (ARM) cloud observations.

In order to investigate the sampling issue that arises from attempting to obtain domain-averaged information from time series of observations, an evaluation technique was developed and tested with Cloud Resolving Model (CRM) and Large Eddy Simulation (LES) model data.

Various cloud properties that are necessary for the PCLOS models such as the absolute cloud fraction (N), cloud thickness, cloud spacing, and horizontal size were inferred from the ARM observations. A set of automated inference techniques were developed. The modeled PCLOS was then tested with the PCLOS inferred from time series of total sky images.

Based on parameters obtained, most models yield PCLOS values that agree with the observations within ±0.2 for the zenith angle range from 10° to 80°. Models that assume the clouds are Poisson distributed give better results than those that explicitly specify the cloud spacing and size distributions.

Ignoring the 3D geometrical effect, the PPH approximation underestimates the downward flux by about 3.7 ± 2.5 Wm^{-2} for the fair weather cumulus over the ARM Southern Great Plains (SGP) site. The limiting factor for the models to generate reliable estimates of the effect may be the uncertainties in the cloud parameters obtained to date.

LONGWAVE RADIATIVE TRANSFER THROUGH 3D CLOUD FIELDS:

TESTING THE PROBABILITY OF CLEAR LINE OF SIGHT MODELS WITH THE

ARM CLOUD OBSERVATIONS

By

Yingtao Ma

Dissertation submitted to the Faculty of the Graduate School of the
University of Maryland, College Park in partial fulfillment
of the requirements for the degree of
Doctor of Philosophy
2004

Advisory Committee:

Professor Robert G. Ellingson, Chairman/Advisor
Professor Ferdinand Baer
Professor Robert Hudson
Professor Zhanqing Li
Professor Theodore J. Rosenberg

ACHNOWLEDGEMENTS

TABLE OF CONTENT

iv

Chapter 1

Introduction

1.1   Background

Clouds can reflect solar radiation thereby cooling the climate system; they can also trap thermal radiation and heat the system. One measure of the cloud radiative effects on the climate system is cloud forcing, which is the difference between the clear-sky and all-sky net radiation at the top of the atmosphere. The Earth Radiation Budget Experiment (ERBE) indicates that clouds can result in a global mean shortwave forcing of -44 Wm^{-2} and a longwave forcing of 31 Wm^{-2}. The net forcing is -13 Wm^{-2} (Ramanathan et al. 1989), which means that, were the clouds to be removed suddenly from the atmosphere while keeping all other radiative properties unchanged, the global mean earth-atmosphere system would realize an instantaneous increase of the net radiation flux density to it of about 13 Wm^{-2}, an increase of about 5.5%.

The earth climate system is very sensitive to the changes of radiation balance. An inter-comparison of 19 different global climate models showed that the differences between model results may stem mainly from the climate induced changes of cloud radiative forcing (Cess et al. 1990). This indicates that relatively small systematic errors in either or both forcing components may greatly affect the performance of the models in predicting the responses of the climate system to the increase of the greenhouse gases. The high sensitivity of the climate models to the changes of radiative forcing requires an accurate treatment of the cloud-radiation process in Global Climate

Model (GCM).

Most GCMs approximate radiation fluxes and heating rates as the cloud amount
weighted average of clear and overcast values, i.e.,

$$F = NF_{cloud} + (1-N)F_{clear} \tag{1.1}$$

where F_{clear} and F_{cloud} are the clear and overcast (upward or downward) fluxes (F),
respectively. The weighting factor N is the absolute cloud fraction, which by definition
is the fractional area of the vertical projection of clouds. F_{clear} and F_{cloud} are calculated
using 1D radiative transfer model assuming both the atmosphere and clouds are
horizontally homogeneous. This simplification neglects the 3D structure of the real
cloud field and inhomogeneity of the optical properties within individual clouds. It is
equivalent to modeling the clouds as plane-parallel horizontal (PPH) plates with
homogeneous optical properties. Some models make an additional assumption that
clouds are black in the longwave region.

Real cloud fields are non-uniform in both morphological and microphysical
senses. Morphological properties that describe a cloud field include: cloud fraction or
number of clouds, spatial distribution of clouds, vertical and horizontal dimensions of
individual clouds, shape of clouds and cloud height. Microphysical properties include:
liquid water content, particle size distribution, phase composition, and temperature
inside clouds. In combination, the morphological and microphysical properties
determine the optical characteristics of a cloud field. A cumulus cloud field is an
example of a real cloud field with high spatial variability.

A cumulus cloud field consists of a group of individual clouds with finite

horizontal and vertical dimensions separated by clear air. The horizontal dimension of an individual cloud is the order of 0.1-10 km, which is much smaller than the resolution of the state-of-art GCMs. In addition to the bulk geometrical brokenness of the cloud field, there is also great spatial variation inside the clouds. A fine structure with significant variations may occur over a few meters inside a cumulus cloud. All these together make the optical properties in a cumulus cloud field highly inhomogeneous.

The error due to neglecting the 3D cloud effects in radiative transfer calculations may be large enough to be climatically significant (Harshvardhan and Weinman 1982; Ellingson 1982; Heidinger and Cox 1996; Han and Ellingson 1999; Takara and Ellingson 2000). Based on Eq 1.1, the cloud forcing at the surface, defined as $CF = F - F_{clear}$, where F is the downward flux at the surface, may be written as $CF = N (F_{cloud} - F_{clear})$. Thus the error in CF due to the variations of N at a given level may be estimated as $\delta N (F_{cloud} - F_{clear})$. For low or middle clouds (cloud base less than 6 km) and $N = 0.5$, a cloud fraction change of no more than 5% would generate an error in the surface longwave CF of the same magnitude as the direct forcing from CO_2 doubling, which is about 1 Wm^{-2} at the surface. As noted by the references cited directly above, the effects of neglecting 3D cloud effects are often much larger than this.

By using the ASTEX (Atlantic Stratocumulus Transition Experiment) data, Heidinger and Cox (1996) estimated that longwave surface flux schemes that ignored the vertical dimensions of clouds typically underestimated the longwave surface forcing by about 9 Wm^{-2} on average.

Harshvandhan (1982) made a study on the sensitivity of the outgoing longwave

and incoming shortwave radiative fluxes to the changes in global cloud cover. He concluded that, compared to the PPH approximation, the magnitude of the individual sensitivity terms (the shortwave sensitivity term and longwave sensitivity term) may be altered two- or three-fold under certain conditions if the cloud brokenness was taken into account. These indicate that using the PPH approximation to deal with the radiative transfer under cloudy conditions may not be valid for some climate studies.

1.2   Previous work

The transfer of radiation through non-PPH clouds has received considerable attention for the past three decades. Using the cumulus observations of Plank (1969), Niylisk (1972) studied the possibility of computing the area averaged downward longwave flux using a modified plane-parallel calculation while taking into account the cloud side effects. He suggested the use of an effective cloud fraction, which incorporates the cloud side effect, instead of the absolute cloud fraction in Eq 1.1 to improve the calculation of the area-averaged fluxes. In addition, he presented a model for calculating the probability of clear line of sight (PCLOS), which is a geometrical characteristic of a 3D cloud field and also a key factor when discussing the cloud side effect or formulating the effective cloud fraction.

In a study of the effects of cloud dimensions on longwave irradiance and heating rate calculations, Ellingson (1982) developed a simplified effective cloud fraction model to incorporate the effects of cloud geometry and vertical temperature variation within the cloud layer. The model is an extension of the approach of

4

Avaste et al. (1974). It parameterized clouds as randomly distributed black but non-isothermal right circular cylinders with constant cloud base height. Based on the model, he found that the irradiance and heating rate are nonlinear functions of the absolute cloud amount, cloud size, and cloud base and top altitude. Incorporation of cloud dimensions in the calculation results in more downward irradiance at the surface (1 - 4%) and less escaping the atmosphere (up to 8%) than from the PPH approximation. The subcloud layer experiences more heating (as much as 20%), whereas the tropospheric column experiences more cooling (up to 10%).

Harshvandhan and Weinman (1982) studied upward longwave radiative transfer through a regular array of cuboidal clouds. Clouds are either black or uniformly non-black. One of their conclusions is that the geometrical considerations often dominate over the microphysical aspects of radiative transfer through the clouds. Their example shows that the difference in simulated 10 μm brightness temperature between black isothermal cubic clouds and cubic clouds of optical depth 10 is less than 2 K for zenith angle less than 50° for all cloud fractions. While neglecting the cloud side effects may result in 2 - 8 K error in brightness temperature for cubic clouds over a wide range of zenith angles. In their study, they also gave an expression for the effective cloud fraction for a regular array of cubic clouds. Different from previous studies, their expression is not derived directly from the PCLOS but is based on a numerical fit to the transmission of diffuse light through an opaque array of cuboids.

Barker and Wielicki (1997) examined the impacts of the horizontal variation of optical depth and cloud sides on the grid-averaged longwave flux transmittance. They revealed the effect of variable optical depth on the longwave radiative transfer. Like the

cloud side and variable temperature, variable optical depth is another aspect that affects the longwave radiative transfer through a non-PPH cloud field. They concluded that the magnitude of the effect due to variable optical depth is larger than that from cloud sides and suggested a scheme to parameterize area-averaged cloud transmittance. Their study was based on fields of optical depth inferred from 45 Landsat images and the PCLOS was simulated using Monte Carlo technique from the optical depth fields.

Han and Ellingson (1999, 2000) made the first attempt to test the various effective cloud fraction expressions with experimental data. Observations from the Atmospheric Radiation Measurement (ARM; Stokes and Schwartz 1994)) Southern Great Plains (SGP) Clouds and Radiation Tested (CART) site were used to derive the absolute cloud fraction, cloud size, spacing and many other cloud field variables. The effective cloud fraction was extracted from hemispheric flux observations. To derive area-averaged variables from time series observations, all their variables were averaged over a sampling period of 10 minutes. Their conclusions were: (1) Cloud bulk geometrical parameters significantly affect the difference between the effective cloud fraction and the absolute cloud fraction; and (2) Cloud horizontal distributions do not significantly influence cloud mutual shading and the effective cloud fraction for cloud fields with small aspect ratios and absolute amount.

Takara and Ellingson (1996, 2000) investigated scattering effects on longwave radiative transfer through a field of randomly distributed right cylindrical clouds. The spectral interval was limited to the 8 - 12 μm window region where it is expected that the longwave 3D cloud effects and scattering effects will be most significant. Their results show that compared to the cloud side effect, cloud scattering can be neglected

6

for optically thick water clouds in summer and tropical soundings. The errors due to neglecting cloud scattering are largest close to the cloud layer and decrease as the distance from the cloud layer increases.

Many attempts have been made to find methods to incorporate 3D cloud effects into radiative transfer calculations while, at the same time, save computational resources. For example, the effective cloud fraction has been suggested to account for the cloud side effect (Niylisk 1972; Ellingson 1982; Harshvandhan and Weinman 1982; Naber and Weinman 1984; Han and Ellingson 1999; Masunaga and Nakajima 2001). Area-averaged cloud transmittance or emittance has been parameterized to account for the variable optical depth effect (Barker and Wielicki 1997; Li and Barker 2002).

Much of the aforementioned research explicitly employed various forms of the PCLOS, which characterizes the radiative-transfer-relevant bulk geometrical effect of clouds with finite vertical dimensions. The PCLOS describes the probability that a line of sight can pass through a cloud field without intersecting a cloud. It is a function of absolute cloud fraction, cloud distribution, cloud size and shape. Figure 1.1 shows an example of the PCLOS for randomly distributed cylindrical clouds with a constant cloud base altitude. If clouds have any vertical dimension, the PCLOS decreases with increasing zenith angle. This is due to the so-called cloud side effect. At a zenith angle $\theta > 0$, cloud sides will also obscure part of the sky. Given the same cloud fraction and distribution, the greater the cloud vertical dimensions, the larger the cloud side effect until mutual shading occurs. At the zenith, the PCLOS = $(1 - N)$, here N is the absolute cloud fraction.

The PCLOS is a property of 3D cloud field. Its involvement in the longwave 3D

effect is very complicated, but correctly specifying the PCLOS in a parameterization scheme for longwave radiative transfer through 3D cloud field is very important. Most previous research focused on theoretical calculations and a variety of PCLOS models have been suggested, based on different assumptions concerning the cloud field properties and different approaches of modeling (Kauth and Penquite 1967; Niylisk 1972; Ellingson 1982; Naber and Weinman 1984; Killen and Ellingson 1994; Han and Ellingson 1999). Few efforts have been spent on the validation of the various models. It is not clear which if any represents real clouds.

Although there are some observational investigations in the literature (Lund and Shanklin 1972, 1973; Rapp et al. 1973; Yu et al. 1986), they were aimed at obtaining the climatic value of the PCLOS and did not have detailed information about the cloud field properties available. For example, the PCLOS data from Lund and Shanklin (1972, 1973) was an average of three years of summer-season observations taken at Columbia Mo. It ignored variations caused by diurnal cycles, weather conditions and cloud altitudes, and did not have detailed cloud morphological information available. As such they are not useable for validating the PCLOS models we address in this study. The experimental data from the ARM program (Stokes and Schwartz 1994) has a detailed description of the clouds and radiation field over its CART sites. This enables us to extract the PCLOS and the variables that were not available before but are necessary for calculating the PCLOS from models, and hence makes the validation of the PCLOS models feasible.

1.3 Study objective and outline

To contribute to the goal of improving parameterization of longwave radiative transfer through 3D clouds, this study has three objectives:

(1) Give a systematic discussion of the PCLOS models and make extensions based on increased understanding of the morphological properties of cloud fields (Chapter 3).

The PCLOS models used by previous researchers are scattered in various papers. A systematic discussion will enhance our understanding of the various PCLOS models and facilitate the testing process. The PCLOS models will be grouped based on different modeling approaches and basic assumptions. Besides detailing the previous derivations, several improvements and extensions will also be attempted.

(2) Develop a method to investigate the sampling issue that arises from attempting to obtain area-averaged information from time series of observations at one location (Chapter4).

Most of the ARM cloud observation instruments are fixed at the ground and detect the clouds only in the zenith direction. Continuously operated instruments generate time series of cloud observations. The desired spatially averaged quantities are usually obtained by averaging the series over a period of time (assuming the frozen turbulence approximation, that is, the statistical properties of the cloud field do not change as the clouds advect with the mean wind speed or develop over the site). Issues that are very important to our testing work, and also to anyone who wants to infer spatially averaged variables from time series observations, are the length of the time series and the frequency of the observations within the series. Over how long a

time period should the average be taken? How do observation frequencies of the different instruments affect the result? How well does the time-averaged value represent the area-averaged value? In this study, a random field approach will be taken to address the problem. The method evaluates the accuracy of various averaging schemes by making use of the variance and auto-correlation function of the field. The method will also be tested using several cloud fields generated by cloud resolving or large eddy simulation models.

(3) Extract the various cloud variables from the ARM observations and test the PCLOS models (Chapter 5).

For the purpose of testing the PCLOS models, cases with broken clouds present are desired. In this study, we concentrate on cumulus cloud fields to test the PCLOS models because they tend to have the most apparent bulk properties; they have significant frequency of occurrence and spatial coverage especially over low and middle latitudes (Hahn and Warren 1999), and they are also difficult to be represented in large-scale models. To avoid the complexity of overlapping cloud layers, only single layer cumulus cloud fields are selected from the comprehensive observations and used in the testing. Comparisons will be made between model calculated PCLOS and values determined from a variety of ground-based instruments including sky dome images, cloud radar, lidar, radar wind profiler and a narrow field-of-view radiometer.

Current GCMs do not explicitly account for 3D radiative effects. As an important parameter for longwave radiative transfer through 3D cloud fields, the PCLOS has the potential to be used in future radiation parameterization schemes. In this

study, through the systematic discussion of various PCLOS models, we explicitly point out the needed variables for various PCLOS models, that is, the physical parameters necessary to make use of the PCLOS in the parameterizations. Also, through the comparison of models with the ARM observations, the performance of the models and the validity of the various assumptions used by the models can be tested. This will facilitate the selection of the models for eventual use in climate simulations. In the long run, the results from this study will be useful to the development of better GCM parameterizations of radiative transfer in cloudy atmospheres, which in turn will contribute to improved climate simulations.

Chapter 2 gives background descriptions concerning 3D cloud effects on longwave radiative transfer and the ARM cloud observing instruments that are relevant to testing the PCLOS models. Chapter 6 summarizes and concludes the research and gives directions for future work.

Chapter 2

3D cloud effects on longwave radiative transfer and the ARM cloud observations

2.1   3D cloud effects on longwave radiative transfer

Three characteristics of 3D clouds have been found to be significant to longwave radiative transfer and have drawn much attention in the literature. They are (1) the 3D geometric shape of clouds, (2) the horizontal variation of the cloud optical depth, and (3) the vertical variation of cloud temperature. (Ellingson 1982; Harvandhan and Weinman 1982; Takara and Ellingson 1996; Barker and Wielicki 1997; Han and Ellingson 1999, 2000; Masunaga and Nakajima 2001).

The most apparent effect due to the 3D shape of the clouds is the increase of the probability of seeing a cloud when the line of sight goes from the zenith to horizon. This influences the effective cloud fraction and hence the radiation fluxes under the cloudy condition.

That the variable optical depth can affect the longwave radiative transfer is a result of the nonlinear dependence of the longwave transmittance on the optical depth.

The cloud temperature links directly to the longwave radiation through the Planck function. However, it is the brokenness of the cloud field or the presence of non-opaque clouds that allows the vertical temperature variation to alter the longwave radiation under cloudy condition. Details will be given in the following sections.

Figure 2.1 gives an illustration of the 3D cloud effect on longwave radiative transfer due to the three characteristics of the clouds.

To help explain the 3D cloud effect, consider a quasi-3D cloudy atmosphere (Fig. 2.2) comprised of a horizontally homogeneous atmosphere with a layer of azimuthally averaged clouds in it. All quantities are azimuthally averaged values. There is only one layer of clouds and all clouds are constrained in the layer between z_b and z_t, denoting cloud base height and cloud top height, respectively. Scattering is neglected. We consider the area-averaged downward longwave radiation flux at a level z under the cloud layer. Following Niylisk (1972) and Ellingson (1982),

$$\overline{F}_{3D}(z) = 2\pi \int_0^1 I_0(z,\mu) P_0(\mu) \mu d\mu + \frac{2\pi}{A} \int_0^1 \mu d\mu \int_{A_c(\mu)} I_{c,3D}(z,x,y,\mu) dx dy \qquad (2.1)$$

where $I_0(z,\mu)$ and $I_{c,3D}(z,x,y,\mu)$ are the radiances received at level z from the clear and cloudy portions of the sky above, respectively. Since the atmosphere is horizontally homogeneous, $I_0(z,\mu)$ is independent of horizontal position, while $I_{c,3D}(z,x,y,\mu)$ is a function of horizontal position, because of the inhomogeneity of the cloud field. $P_0(\mu)$ is the azimuthally averaged probability of a clear line of sight. μ is the cosine of zenith angle. $A_c(\mu)$ is the projection area of the clouds at direction μ. A is the total area of the domain.

Using the same form as Eq 2.1, the area-averaged flux for the PPH approximation can be written as

$$\overline{F}_{PPH}(z) = 2\pi \int_0^1 I_0(z,\mu)(1-N) \mu d\mu + 2\pi \int_0^1 \mu d\mu \, I_{c,PPH}(z,\mu) N \qquad (2.2)$$

where N is the absolute cloud fraction and $I_{c,PPH}(z,\mu)$ is the radiance coming from a PPH

cloud. Since N is independent of μ, and since $F(z) = 2\pi \int_0^1 I(z,\mu)\mu d\mu$, Eq 2.2 reduces to

Eq 1.1.

      We are interested in the difference between the area-averaged fluxes from the

PPH approximation and the 3D clouds.

$$\Delta\overline{F}(z) = \overline{F}_{PPH}(z) - \overline{F}_{3D}(z) = 2\pi \int_0^1 I_0(z,\mu)(1 - N - P_0(\mu))\mu d\mu$$

$$+ 2\pi \int_0^1 \left[I_{c,PPH}(z,\mu)N - \frac{1}{A}\int_{A_c(\mu)} I_{c,3D}(z,x,y,\mu)dxdy \right]\mu d\mu$$

$$(2.3)$$

      In the above equation, the pencil of radiance passing through the 3D cloud field

and reaching on level z may be written as

$$I_{c,3D}(z,x,y,u) = I_0(0 - z_t,\mu)\, T_{c,3D}(z_t - z_b,x,y,\mu)\, T_0(z_b - z,\mu)$$

$$+ I_{c,3D}(z_t - z_b,x,y,\mu)\, T_0(z_b - z,\mu) \qquad (2.4)$$

$$+ I_0(z_b - z,\mu)$$

where $0 - z_t$ denotes the mass along a slant path at a direction μ between the top of

atmosphere and the level z_t. Thus, $I_0(0 - z_t, \mu)$ denotes the radiance incident at z_t in

direction μ generated by atmosphere above the cloud layer, and $I_0(z_b - z, \mu)$ is the

radiance at z in direction μ generated by atmosphere below the cloud layer. $T_0(z_b - z, \mu)$

is the transmissivity of the atmosphere below the cloud layer along μ. In the following,

we will ignore the absorption by atmospheric gases within the cloud layer for discussion

purposes. Thus, $z_t - z_b$ denotes only the cloud mass. $T_c(z_t - z_b, x,y,\mu)$ is the cloud

transmissivity through the cloud layer in direction μ corresponding to a horizontal

position denoted as (x, y). $I_{c,3D}(z_t - z_b, x, y, \mu)$ is the radiance at z in direction μ from the clouds. $I_{c,PPH}(z,\mu)$ would have the same form as Eq 2.4, only the transmissivity and the radiance from the cloud are independent of horizontal positions.

2.1.1 Geometrical effect

Consider the 3D clouds to be isothermal blackbodies. This will eliminate the optical depth and temperature variations. Only the cloud bulk geometric property can contribute to this 3D effect. The cloud layer transmissivity $T_{c,PPH} = T_{c,3D} = 0$. The PPH cloud is assumed to be a black plane-parallel cloud. Under these assumptions, the flux difference at level z may be written as

$$
\begin{aligned}
\Delta \overline{F}(z) = {} & 2\pi \int_0^1 I_0(z,\mu)(1 - N - P_0(\mu))\mu d\mu \\
& + 2\pi \int_0^1 \left[I_{c,PPH}(z_t - z_b, \mu)N - I_{c,3D}(z_t - z_b, \mu)(1 - P_0(\mu)) \right] T_0(z_b - z, \mu)\mu d\mu \\
& + 2\pi \int_0^1 I_0(z_b - z, \mu)(N - 1 + P_0(\mu))\mu d\mu
\end{aligned}
$$

$$(2.5)$$

where $I_{c,PPH}(z_t - z_b, \mu)$ and $I_{c,3D}(z_t - z_b, \mu)$ are downward radiance at level z_b from the PPH cloud and 3D black clouds, respectively. If the PPH cloud takes the same temperature at the 3D isothermal black clouds, $I_{c,PPH}(z_t - z_b, \mu) = I_{c,3D}(z_t - z_b, \mu)$.

Thus the difference between the PPH approximation and 3D black clouds can be rewritten as

$$\Delta \overline{F}(z) = 2\pi \int_0^1 \left[I_0(z,\mu) - I_c(z,\mu) \right](1 - N - P_0(\mu))\,\mu\,d\mu \qquad (2.6)$$

Eq. (2.6) shows that, for isothermal black clouds, the difference between the area-averaged fluxes from the PPH approximation and 3D black clouds is caused by the difference between $P_0(0) = 1 - N$ and $P_0(\mu)$. Note that $(1 - N) \geq P_0(\mu)$ for all μ, and on the other hand, since the atmosphere temperature generally decreases with height, the clear-sky radiance is usually less than that from the cloudy-sky, i.e. $I_0(z,\mu) - I_c(z,\mu) \leq 0$. Thus, the PPH approximation would underestimate the downward flux at level z.

Referring to Fig. 2.1, the geometric effect can also be described intuitively. The PPH approximation uses the absolute cloud fraction N as a weighting factor to calculate the domain-averaged fluxes. N is the fractional cloud cover projected vertically downward on the ground. It is equivalent to say that the PPH approximation uses this same cloud fraction for all zenith angles to count the radiance from clouds. No matter the zenith angle, only those beams that fall in the N portion of the cloud projection (the homogeneous rectangular boxes in the figure) are counted as the beams from clouds (beam (B) for example). Whereas in a broken cloud field, the existence of spacing between clouds allows radiation from cloud sides to reach at level z as well (beam (A) in Fig. 2.1). However, since these beams fall outside the PPH cloud vertical projection, they will be neglected by the PPH approximation and instead be counted as clear.

When clouds are broken and have vertical dimensions, viewed at any angle $\theta > 0$, the clouds will expose a larger area to an observer than that from the PPH

approximation. A larger projection area means a larger fraction of sky being obscured by clouds. That is, there is an increment in *N*. Since the increment will always be positive, if clouds are assumed as blackbodies, compared to the PPH approximation, the brokenness of the cloud field will increase the downward flux under the clouds and decrease the upward flux above the clouds.

The extent of the longwave geometric effect depends on the vertical dimension of the clouds, the distribution of the spacing between clouds and the shape of the clouds. The larger the vertical extent of the clouds and the spacing between clouds, the larger the geometric effect of the clouds. The spacing between clouds closely relates to the cloud fraction. As the cloud fraction becomes larger and larger, the spacing between clouds becomes smaller and smaller. This will depress the geometric effect because of the increase in the mutual obscuration. The shape of the clouds also has an impact on the geometric effects. Given a same vertical extent, a cloud with a large, flat top tends to obscure more sky than a cloud with a small, round top, and thus will have more pronounced geometric effect.

From Eq. (2.6) we notice that there is another term that also controls the impact of clouds on a level outside the cloud layer. The term $I_0(z,\mu) - I_c(z,\mu)$ is the difference between clear and cloudy radiance at level *z*, and

$$I_0(z,\mu) - I_c(z,\mu) = \left[I_0(z_b,\mu) - I_c(z_b,\mu)\right] T_0(z_b - z,\mu),$$

where $\left[I_0(z_b,\mu) - I_c(z_b,\mu)\right]$ is the difference between clear and cloudy radiance at cloud base level z_b. The transmissivity $T_0(z_b - z, \mu)$ represents the attenuation by the atmosphere between the cloud base z_b and the level *z*. If the intervening atmosphere is

17

very opaque, the 3D cloud effect or any cloud effects at level z will be largely attenuated. This implies two consequences. First, especially at lower levels of the atmosphere, due to the large amount of absorbing gases, the 3D effects will mostly affect the layers that are close to the cloud layer. Second, the 3D cloud effect will be more significant in the window region because there is a large difference between $I_o(z_b, \mu)$ and $I_c(z_b, \mu)$ and $T_o(z_b - z, \mu)$ is close to 1. These are actually general properties of longwave radiative transfer in a cloudy atmosphere and are not limited to the 3D cloud effect.

2.1.2 Variable cloud optical depth effect

Liquid water clouds are not always black, as there may be a substantial amount of thin clouds present in a broken cloud field. The optical depth may span a wide spectrum of values. Due to the nonlinear dependence of the cloud transmission and emission on the optical depth, neglecting the inhomogeneity in the optical depth may be another source of bias in the PPH approximation (Barker and Wielicki 1997).

To illustrate the impact of the variable optical depth, assume the 3D clouds are non-black and isothermal, and for simplicity also ignore the geometric effect, i.e., $P_0(\mu) = 1 - N$. The PPH cloud is assumed to be a non-black plane-parallel homogeneous cloud. The flux difference between the PPH approximation and 3D clouds at level z can be written as

$$\Delta \overline{F}(z) = 2\pi N \int_0^1 \left[I_0(0 - z_t, \mu) \, \Delta T_c(\mu) + \Delta I_c(\mu) \right] T_0(z_b - z, \mu) \, \mu d\mu \qquad (2.7)$$

where
$$\begin{cases} \Delta T_c(\mu) = T_{c,PPH}(z_t - z_b, \mu) - \int T_{c,3D}(z_t - z_b, \tau_c^\mu, \mu) \, p(\tau_c^\mu \mid \mu) \, d\tau_c^\mu \\ \Delta I_c(\mu) = I_{c,PPH}(z_t - z_b, \mu) - \int I_{c,3D}(z_t - z_b, \tau_c^\mu, \mu) \, p(\tau_c^\mu \mid \mu) \, d\tau_c^\mu \end{cases}$$

are the transmissivity and radiance differences between the PPH approximation and the 3D clouds for the cloud layer. The area averages have been replaced by averages over the optical depth ensemble, i.e.,

$$\frac{1}{A} \int_{A_c(\mu)} X(z_t - z_b, x, y, \mu) \, dx \, dy = (1 - P_0(\mu)) \int X(z_t - z_b, \tau_c^\mu, \mu) \, p(\tau_c^\mu \mid \mu) \, d\tau_c^\mu$$

$$X = T_{c,3D}(\mu) \text{ or } I_{c,3D}(\mu)$$

τ_c^μ is the cloud optical depth measured along the slant path described by μ. $p(\tau_c^\mu \mid \mu)$ is the probability distribution of the slant path optical depth conditional upon μ (Barker and Wielicki 1997). Again for discussion purposes we neglect the absorption by atmospheric gases within the cloud layer. Note that with the isothermal assumption, the radiance difference may be further written as

$$\begin{aligned} \Delta I_c(\mu) &= B_c \left[\varepsilon_{c,PPH}(z_t - z_b, \mu) - \int \varepsilon_{c,3D}(z_t - z_b, \tau_c^\mu, \mu) \, p(\tau_c^\mu \mid \mu) \, d\tau_c^\mu \right] \\ &= -B_c \left[T_{c,PPH}(z_t - z_b, \mu) - \int T_{c,3D}(z_t - z_b, \tau_c^\mu, \mu) \, p(\tau_c^\mu \mid \mu) \, d\tau_c^\mu \right] \end{aligned}$$

where B_c is the Planck function at the cloud temperature. $\varepsilon_{c,PPH}(z_t - z_b, \mu)$ and $\varepsilon_{c,3D}(z_t - z_b, \tau_c^\mu, \mu)$ are the slant path emissivities for the PPH cloud and 3D clouds, respectively. The flux difference (Eq. (2.7)) can be rewritten as

$$\Delta \overline{F}(z) = 2\pi N \int_0^1 \left[I_0(0 - z_t, \mu) - B_c \right] \Delta T_c(\mu) T_0(z_b - z, \mu) \, \mu \, d\mu \qquad (2.8)$$

Where

$$\Delta T_c(\mu) = T_{c,PPH}(z_t - z_b, \mu) - \int T_{c,3D}(z_t - z_b, \tau_c^\mu, \mu) \, p(\tau_c^\mu \mid \mu) \, d\tau_c^\mu$$

$$= e^{-\tau_{c,PPH}/\mu} - \int e^{-\tau_c^\mu(\mu)} p(\tau_c^\mu \mid \mu) \, d\tau_c^\mu$$

The manifestation of the effect of neglecting the horizontal variation of the optical depth in the PPH approximation is through the transmission (or emission) difference between the PPH approximation and 3D clouds. The difference results from the nonlinear dependence of the transmission on the optical depth. The transmission at the average optical depth may not equal the average transmission, i.e.,

$e^{-\tau_{c,PPH}/\mu} \neq \int e^{-\tau_c^\mu(\mu)} p(\tau_c^\mu \mid \mu) \, d\tau_c^\mu$. The sign and size of the effect due to the variable

optical depth depend on the choice of $\tau_{c,PPH}$ and the distribution of $\tau_c^\mu(\mu)$. It has been

shown that if $\tau_{c,PPH}$ takes the mean of $\tau_c^\mu(1)$, i.e. the mean value of the vertical optical

depth, the PPH approximation will overestimate the downward flux at the surface.

The expression for the flux difference due to the variable optical depth (Eq. (2.8)) is similar to that due to the geometric effect (Eq. (2.6)). Both of them imply that the state of the atmosphere above the cloud layer or intervening the cloud layer and level z will also affect the 3D cloud effect observed at level z. For example, consider the $\left[I_0(0 - z_t, \mu) - B_c \right]$ term in Eq. (2.8). For downward longwave radiation, if the absorbing gases above the cloud layer are so dense that they emit radiation at a temperature close to the cloud temperature, there will be little contrast between the clouds and their background. Neither the geometric change nor the optical depth variation will have much impact on the downward flux at level z for this condition. This is an important consideration away from the window regions; however, the atmosphere

is always sufficiently transparent that there is a spectrally integrated difference between

the emission from the clear and overcast portions of the sky.

2.1.3 Variable temperature effect

The third aspect of the longwave 3D cloud effect is due to the non-uniform

temperature within the cloud layer. To simplify the explanation of the effect, assume the

3D clouds are non-isothermal and opaque, and ignore the geometric effect, i.e.

$P_0(\mu) = 1 - N$. Only the vertical variation of temperature is considered. The PPH cloud

is assumed to be a black plane-parallel plate. The downward flux difference between the

PPH approximation and 3D cloud may be written as

$$
\begin{aligned}
\Delta \overline{F}(z) &= 2\pi N \int_0^1 \left[I_{c,PPH}(z_t - z_b, \mu) - \frac{1}{A} \int_{A_c(\mu)} I_{c,3D}(z_t - z_b, x, y, \mu)\, dxdy \right] T_0(z_b - z, \mu)\, \mu d\mu \\
&= 2\pi N \int_0^1 \left[B_{c,PPH} - \int B_{c,3D}(z', \mu)\, p(z' \mid \mu)\, dz' \right] T_0(z_b - z, \mu)\, \mu d\mu
\end{aligned}
$$

$$(2.9)$$

where $B_{c,PPH}$ is the Planck function for the PPH cloud. $B_{c,3D}(z',\mu)$ is the Planck function

for the 3D clouds at altitude z'. z' is the height of the location on the cloud side from

where a pencil of radiance emits downward to level z at direction μ. z' ranges from the

cloud base height, z_b, to the cloud top height, z_t. $p(z' \mid \mu)$ denotes the probability

distribution of z' conditional on μ. Like that in Eq. (2.7), the ensemble average over z'

has been substituted for the average over area. The size and sign of the flux difference

depend on the choice of the temperature of the PPH cloud and the distribution of

$p(z' | \mu)$. Since the temperature of a real cloud will usually decrease with increasing altitude, if the PPH cloud is set at the cloud base temperature, the PPH cloud will overestimate the downward flux, as has been shown by Ellingson (1982). The reason for this is because the portion of radiation from cloud sides is emitted at a temperature that is lower than the cloud base temperature, which is the one the PPH cloud assumed. For upward flux, the PPH approximation usually emits radiation at the cloud top temperature. This may underestimate the upwelling flux. Compared with the geometric effect, the impact of the variable temperature is of opposite sign.

In the above discussions, the three aspects of the 3D effects were addressed separately, but in reality, the three aspects act simultaneously. That is, a real cloud field may have simultaneous variations in the cloud vertical dimension, optical depth and vertical temperature gradient. The longwave fluxes though the 3D cloud field is a combined result of all three aspects of the 3D effects. The PCLOS plays a major role in determining the radiative transfer through the broken cloud field for each effect, although it is primarily connected with the geometrical effect. The effective cloud fraction, suggested by some researchers to address the geometrical effect, is almost solely dependent on the PCLOS. Nonetheless, the PCLOS is an important modulating factor for the longwave 3D cloud effects. Thus, a close study of the PCLOS of broken cloud fields will surely contribute to the general understanding of the longwave 3D radiative transfer.

2.2   The ARM cloud observation instruments.

The Central Facility (CF) of the ARM SGP CART site is located between Lamont and Billings, Oklahoma (36.61N, 97.49W, 315 m above sea level). A variety of instruments have been deployed at the site aimed for mapping the three-dimensional structure of the atmosphere, cloud and radiation field in a continuously and automated fashion. In the following, a brief description will be given for several instruments that are relevant to our goal of testing the PCLOS models. Detailed information can be found at http://www.arm.gov. Table 2.1 lists the desired cloud field properties and the instruments from which the properties will be determined in this study.

Table 2.1: The desired cloud properties and the instruments used to measure or infer them.

Variable	Instruments
PCLOS(θ)	TSI, WSI
Absolute cloud fraction	NFOV, TSI, Lidar/Ceilometers, MMCR, ARSCL
Cloud spacing distribution	NFOV, Lidar/Ceilometers, MMCR, ARSCL
Cloud horizontal size distribution	NFOV, Lidar/Ceilometers, MMCR, ARSCL
Cloud base height	Lidar/Ceilometers, MMCR, ARSCL
Cloud top height	MMCR, Lidar, BBSS
Wind speed	RWP915, BBSS

TSI – Total Sky Imager

WSI – Whole Sky Imager

NFOV – Narrow Field of View Sensor

MMCR – Millimeter wave Cloud Radar

RWP915 – 915-Mhz Radar Wind Profiler and radio acoustic sounding system

BBSS – Balloon-Borne Sounding System

ARSCL - Active Remotely-Sensed Clouds Locations

The all sky images taken by the Total Sky Imager (TSI) and Whole Sky Imager (WSI) will be used to infer the PCLOS as a function of zenith angle. The TSI is an automatic, full-color sky imager system. It records visual images of the sky dome from a heated, rotating hemispherical mirror at an adjustable sampling rate, which is set at one per 20 seconds at the SGP site. The field of view of the TSI is about 160°. The resolution of the output image is 352x288 pixels. The TSI data available at the ARM data archive starts in July 2000 and includes the raw sky images and classified 'cloud decision' images. The availability of the classified images greatly facilitates our retrieval of the PCLOS. Detailed information on inferring the PCLOS from the TSI and WSI is presented in Chapter 5.

The WSI is a ground based imaging system that monitors the upper hemisphere using a fisheye lens and four spectral filters (near IR, red, blue and neutral). Besides the cloud presence and distribution, the WSI can also measure the radiance in an approximately $1/3^o$ increment over the entire sky dome (180°). The chief advantage of the TSI compared to WSI is its higher time resolution. The time interval between images for the TSI is 20 seconds, whereas for the WSI, it is 6 minutes. The WSI is capable of acquiring images under daylight, moonlight, and starlight conditions. The data has been available from the SGP site since 1995.

The Narrow Field of View Zenith Radiometer (NFOV) is a ground-based radiometer that looks vertically upward. It operates at a wavelength of 869 nm and senses a spectral interval that has a Full Width at Half Maximum (FWHM) of 10 nm. The field of view of the instrument is 5.7^o. The output of the instrument is a time series of 1-sec observations of the downwelling spectral radiance at the zenith. Two main

features of the NFOV pertinent to our study are its high sampling rate and narrow field of view. These features enable us to precisely measure the horizontal sizes of the clouds and spacing between clouds as will be discussed in detail in Chapter 5.

Since the horizontal size and spacing are inferred using the frozen turbulence assumption, wind speed is a must for this study. It is obtained from the 915-Mhz Radar Wind Profiler (RWP915). The RWP915 makes observations in a cyclic sequence of five pointing directions, one in vertical and four in near-vertical directions (two in the north-south vertical plane, and two in the east-west vertical plane). The radial components of the wind speed are determined for each of the directions from Doppler-shifted return signals. Horizontal wind speed and direction are then obtained by combining the radial components. Profiling is achieved by measuring the time delay of the radar pulses. The measurement range of the RWP915 at the SGP site is 0.1 – 5 km. The wind speed data from the radar is a 50-minute averaged value with an accuracy of about 1 m/s.

The Millimeter wave Cloud Radar (MMCR) is a 35 GHz zenith-pointing cloud profiling radar. It measures the radar reflectivity (dBZ) of the atmosphere up to 20 km at a time resolution of 10s. Its Doppler capability also allows the measurement of the vertical velocities of cloud constituents. The main purpose of this radar is to determine cloud boundaries (e.g., cloud bottoms and tops). Although the short operating wavelength gives the MMCR the capability of observing almost all clouds including the non-precipitating clouds, large amounts of non-hydrometeor particulates over the SGP CART site, such as insects and bits of vegetation, make the radar difficult to use for detecting lower lever clouds during the warm seasons.

Information from various laser instruments can be used to complement the MMCR cloud detection. Several Lidars relevant to this study are the Micropulse Lidar (MPL), the Vaisala Laser Ceilometer (VCEIL) and the Raman Lidar (RL). These instruments emit short, powerful laser pulses in the vertical direction, and measure the light intensity backscattered by haze, fog, clouds and atmospheric molecules (RL only) as the laser pulses traverse the sky. The MPL and VCEIL are elastic backscatter systems that measure the return signal at the same wavelength as the transmitted beam. Based on the delay time between the transmitted pulse and the returned scattering signal the MPL and VCEIL can detect the cloud base height and, for some thin clouds, the top height. The RL measures the Raman scattering signals at 387 and 408 nm due to nitrogen and water vapor molecules, respectively. A range-resolved water vapor mixing ratio can then be deduced from the ratio of the water vapor signal to the nitrogen signal. The water vapor mixing ratio profiles may help us to determine the availability of the water vapor to cloud formation at the cloud top level and thus acts as a complementary information source for the determination of the cloud top height.

The Active Remotely-Sensed Clouds Locations (ARSCL) is ARM's attempt to produce an objective determination of hydrometeor height distributions, their radar reflectivities, vertical velocities, and Doppler spectral widths from the combination of data from the various remote sensing instruments including the MMCR, the Lidars and a Microwave Radiometer (MWR) (Clothiaux et al. 2001). It contains information about the cloud boundary heights (cloud base and cloud top) for each cloud layer detected, as a function of time. However, due to the lack of a satisfactory solution to the airborne clutter problem at the present, the cloud top data from the ARSCL is in its tentative

state, especially for those boundary clouds that occur with the clutter layer present and

extended to above the cloud top.

Table 2.2 summarizes specifications of the various cloud observation

instruments that are relevant to our work of testing the PCLOS models.

Table 2.2 The ARM cloud observation instruments and their specifications.
(More details concerning the above instruments can be found at:
http://www.arm.gov)

Instrument	Primary quantities obtained	Spectral characteristic	Field of View	Temporal resolution	Vertical resolution	Measurement Accuracy
Total Sky Imager (**TSI**)	Time series of hemisphere sky images.	Full color visible	160° (352 x 288 pixels)	20 sec.		
Whole Sky Imager (**WSI**)	Sky radiance; Cloud cover.	650 nm, (FWHM = 70nm); 450 nm, (FWHM = 70nm); 800 nm, (FWHM = 70nm); 400 – 900 nm.	180° (34 mrad Angular resolution)	1 – 10 min. (6 min at SGP)		±5% (radiance)
Narrow Field of View Sensor (**NFOV**)	Zenith spectral radiance.	869 nm (FWHM = 10nm)	5.7^o	1 sec.		±15% (radiance)
915-MHz Radar Wind Profiler and Radio Acoustic Sounding System (**RWP915**)	Wind profiles (0.1 – 5 km); Virtual temperature (0.1 – 1.5 km).	915 MHz		60 min.	0.06 – 1 km	1 m/s (wind speed)
Millimeter Wave Cloud Radar (**MMCR**)	Radar reflectivity; Doppler spectra; Cloud boundaries; Cloud constituent vertical velocity. (0.1 – 15 km)	35 GHz	0.2^o	10 sec.	45 m, 90 m	0.1 m/s (vertical velocity) 0.5 dB (reflectivity)
Micropulse Lidar (**MPL**)	Cloud boundary. (0.12 – 20 km)	523 nm	0.1 mrad. (beam divergence)	1 min.	300 m, 75 m	
Vaisala Ceilometer (**VCEIL**)	Cloud base height. (0.2 – 7.5 km)	905 nm	0.66 mrad (beam divergence)	15 sec.	15 m	
Raman Lidar (**RL**)	Vertical profiles of water vapor mixing ratio or aerosol scattering ratio.	408 nm (H2O) 355 nm (aerosol) 387 nm (N2)	0.1 mrad (beam divergence)	10 min.	78 m	
Balloon-Borne Sounding System (**BBSS**)	Vertical profiles of temperature, relative humidity, wind speed and direction.			Every 6 hours at 0530, 1130, 1730, 2330	2 s (sampling rate)	0.3^{o}c (temp.) %1 (R.H.) 0.5m/s (wind)

Chapter 3

Formulation of the PCLOS Models

The PCLOS is the probability of a clear line of sight through a cloud field at a given zenith angle. Assuming the cloud field is isotropic in horizontal directions, the PCLOS is not a function of azimuth. We will address three ways to model the PCLOS. (1) Since the PCLOS is equivalent to $1 - N(\theta)$, where $N(\theta)$ is the cloud fraction seen at zenith angle θ or the fractional projection area projected at θ onto a horizontal plane, finding $N(\theta)$ is equivalent to determining the PCLOS. (2) Following the definition of "PCLOS", one can trace a line of sight to determine its chance of passing through a clear section of the cloud field, provided that one has statistical information concerning the cloud field along the line of sight. (3) Following Han and Ellingson (1999), PCLOS can be modeled as the fractional number of cloud pairs that are separated from each other by a critical distance.

For each method mentioned above, depending on the assumptions made about the cloud field, there are differences among various PCLOS models. For example, for the method of calculating $N(\theta)$, if we assume clouds are regularly distributed on a plane, we obtain one model of the PCLOS. Or if we assume clouds are randomly distributed on a plane, we get another model of the PCLOS. In this chapter, we will discuss the three methods of modeling the PCLOS and give expressions for the various models.

3.1 Modeling the PCLOS by computing $N(\theta)$

Depending on the method of describing a cloud field, three methods of modeling $N(\theta)$ will be addressed in this section. The first method describes the cloud field by explicitly specifying cloud size and spacing distributions. The second method assumes the clouds with arbitrary sizes are randomly distributed on a horizontal plane. The third method arranges the clouds regularly on a horizontal plane.

3.1.1 Given cloud size and spacing distributions

This type of model was first used by Niylisk (1972), and latter by Killen and Ellingson (1994) and Han and Ellingson (1999). Here we will give a systematic discussion of the model. The model infers $N(\theta)$ from a vertical section of a cloud field. Fig. 3.1 illustrate such a section of a cloud field. For such a 2D cloud field, $1-N(\theta)$, which is equivalent to the PCLOS, is given by

$$p(\theta) = 1 - N(\theta) = \frac{\sum s_c(\theta)}{total\ length\ of\ the\ domain\ line} = \frac{\overline{s_c(\theta)}}{mean\ length\ of\ the\ cloud\ element}$$

(3.1)

where $s_c(\theta)$ represents a clear section on a horizontal line parallel to the line of the cloud base that is not covered by the projections of the clouds at zenith angle θ.

As seen from Fig. 3.1, a feature of this 2D cloud field is that for every cloud there is a corresponding spacing associated with it. The number of clouds is the same as the number of spacings. We may define a combination of a cloud and the spacing to its

left as a cloud element. A cloud field consists of many such cloud elements. Fig. 3.2 illustrates a single cloud element.

The absolute cloud fraction N, which by definition is the fraction of the total lengths occupied by the vertical projections of clouds for such a 2D cloud field, may be given as

$$N = \frac{\sum d}{\sum d + \sum s} = \frac{\bar{d}}{\bar{d} + \bar{s}} \tag{3.2}$$

where $\bar{s} = \overline{s_c(0)}$, and $\bar{d} + \bar{s}$ is the mean length of the cloud elements. Eq. (3.2) connects the mean cloud horizontal size to the mean cloud spacing through the absolute cloud fraction. With a given N, $p(\theta)$ can be written as

$$p(\theta) = (1 - N) \frac{\overline{s_c(\theta)}}{\bar{s}} \tag{3.3}$$

Eq. (3.3) indicates that when the line of sight is in the zenith direction, $\overline{s_c(\theta)}$ equals $\bar{s}$ and the PCLOS becomes (1-N). When the zenith angle of the line of sight approaches 90°, (the horizontal), $\overline{s_c(\theta)}$ goes to zero and PCLOS approaches zero.

Given a zenith angle θ, every cloud element has a corresponding $s_c(\theta)$ which is the portion of s uncovered by the projection of the cloud on the horizontal line at θ. Assuming the cloud elements are independent of each other, the mean $s_c(\theta)$ can be given by

$$\overline{s_c(\theta)} = \iint_{(all\ cloud\ elements\ with\ s_c > 0)} s_c(\theta, s, h)\ p(s, h)\ ds\ dh \tag{3.4}$$

where $p(s, h)dsdh$ is the joint probability of a cloud element with its spacing lies in $[s,\ s+ds]$ and height in $[h,\ h+dh]$. If we further assume that the cloud spacing and

size are independent of each other, in other word, $p(s,h) = p(s)p(h)$, then the mean $s_c(\theta)$ can be written as

$$\overline{s_c(\theta)} = \iint\limits_{(all\ cloud\ elements\ with\ s_c > 0)} s_c(\theta,s,h)\ p(s)p(h)\ ds\ dh \qquad (3.5)$$

In the above discussion, the three characteristic parameters of a cloud element s, d and h are all independent of each other. There is no restrictive relations among them, except Eq. (3.2).

Plank (1969) found that the cloud height and the cloud diameter for fair weather cumulus may be fitted to a function of the form

$$\frac{h}{d} = \beta\left(\frac{d}{d_{max}}\right)^a$$

where d is the cloud diameter, d_{max} is the maximum diameter of the clouds, and a and β are fitting parameters. He also found that the average value of a is close to 0.0. Thus, the cloud height can be related to cloud diameter simply by $h = \beta d$, i.e., a fixed aspect ratio. This result has been used by several other authors (Han and Ellingson 2000; Killen and Ellingson 1994). The simple linear relationship between the h and d qualifies them to have a same distribution. That is $p(h)$ and $p(d)$ will have same functional form and parameters. Instead of using (s, h), we use $(s, d = h/\beta)$ to characterize a cloud element. Eq. (3.5) can be rewritten as

$$\overline{s_c(\theta)} = \iint\limits_{(all\ cloud\ elements\ with\ s_c > 0)} s_c(\theta,s,d)\ p(s)p(d)\ ds\ dd \qquad (3.6)$$

Now a general form of PCLOS for the 2D cloud field can be given as

$$p(\theta) = \frac{(1-N)}{\overline{s}} \iint\limits_{(all\ cloud\ elements\ with\ s_c > 0)} s_c(\theta,s,d)\ p(s)p(d)\ ds\ dd \qquad (3.7)$$

31

So far our discussion is in a general sense. No specific form of $p(s)$, $p(d)$ and cloud shape have been assumed. There can be various combinations of $p(s)$, $p(d)$ and cloud shapes. The power law distribution, Weibull distribution, exponential distribution and the lognormal distribution are four theoretical distributions that have been used to model cloud size and/or cloud spacing distributions (Plank 1969; Lopez 1977; Joseph and Cahalan 1990; Zhu et al. 1992; Han and Ellingson 1999). The cloud shapes that have been used by various authors include right-cylinder, semi-ellipse, isosceles-trapezoid and so on. In the following sections we will discuss some combinations of the aforementioned distributions and cloud shapes.

To facilitate the following discussion, we give a naming convention for the various PCLOS models according to the different $p(s)$, $p(d)$ and cloud shape each model employed. All the PCLOS models will be named in the form of

"Domain Dimension _ (sd/xd/cd) _ Type of $p(s)$ _ Type of $p(d)$ _ Cloud Shape"

where the domain dimension, 1D or 2D, indicates the dimension of the space that the cloud bases occupy. A 1D domain is a horizontal line, and every cloud is assumed to be a 2D geometric object that lies on the line. "sd/xd/cd" indicates the type of cloud spacings (see Fig. 3.3). 'sd' denotes that the cloud spacing is defined as the distance between the edges of two adjacent clouds. "xd/cd" type of cloud spacing will be mentioned in the following sections. As an example of the naming convention, "1D_sd_Power_Power_IsoscelesTrapezoid" means a PCLOS model which assumes an

one dimensional cloud base domain, 'sd' type of the cloud spacing, power-law

distributions for both the cloud size and spacing, and an isosceles-trapezoidal cloud

shape.

3.1.1.a 1D_sd_Power_Power_IsoscelesTrapezoid

For an isosceles trapezoidal cloud, $s_c(\theta)$ can be written as

$$s_c(\theta, s, d) = s - d\beta(\tan\theta - \tan\eta) \tag{3.8}$$

where s is the cloud spacing, d is the cloud size and β is the aspect ratio (= h/d). The

angle η is the inclination angle of the isosceles trapezoidal cloud. To compute the

PCLOS we need to calculate the mean s_c as shown in Eq. (3.7). When performing the

integration, one should pay attention to the integration limits in Eq. (3.7), as some

combinations of s and d may generate unrealistic negative values of s_c. As seen from

Fig. 3.2, s_c is the clear section of s at zenith angle θ. It decreases with increasing θ, but

should not be less than 0. The zero value occurs when the spacing is totally covered by

the cloud projection. Thus, one has to carefully select the limits of the integration to

fulfill the condition $s_c \geq 0$. This condition implies $s \geq d\beta(\tan\theta - \tan\eta)$ or

$d \leq s/\beta(\tan\theta - \tan\eta)$. Another condition for Eq. (3.8) is that the equation applies only

when $\theta > \eta$. Note that, when a line of sight is at a zenith angle $\theta < \eta$, it will either see

the clear sky or be blocked by the cloud base, but not see the cloud side.

If there exist minimum values for the cloud size and spacing, the integral

domain will have different shapes for θ greater or less than $\theta_c = \tan^{-1}(s_{min}/h_{min} + \tan\eta)$,

where $s_{\min}$ and $d_{\min}$ ($= h_{\min}/\beta$) denote the minimum spacing and size, respectively. All

these conditions combined to determine the integral domain for $\overline{s_c(\theta)}$, as illustrated in

Fig. 3.4.

When $\theta > \theta_c$, the shadow of the cloud with any height will be greater than $s_{\min}$.

Thus the integral domain is

$$
\begin{cases}
d: & d_{\min} \to \dfrac{s}{\beta(\tan\theta - \tan\eta)} \\
s: & d_{\min}\beta(\tan\theta - \tan\eta) \to \infty
\end{cases}
$$

When $\theta < \theta_c$, the shadow of a cloud is very short, and even the cloud elements

with smallest spacing will have $s_c > 0$. Thus the integral domain is

$$
\begin{cases}
d: & d_{\min} \to \dfrac{s}{\beta(\tan\theta - \tan\eta)} \\
s: & s_{\min} \to \infty
\end{cases}
$$

Considering the appropriate integral domain, Eq. (3.7) for isosceles trapezoidal

clouds can be rewritten as

$$
p(\theta) =
\begin{cases}
\dfrac{(1-N)}{\overline{s}} \displaystyle\int_{s_{\min}}^{\infty} p(s)\ ds \int_{d_{\min}}^{\frac{s}{\beta(\tan\theta - \tan\eta)}} [s - d\beta(\tan\theta - \tan\eta)]\ p(d)\ dd, & \text{for } \eta < \theta < \theta_c \\[3em]
\dfrac{(1-N)}{\overline{s}} \displaystyle\int_{d_{\min}\beta(\tan\theta - \tan\eta)}^{\infty} p(s)\ ds \int_{d_{\min}}^{\frac{s}{\beta(\tan\theta - \tan\eta)}} [s - d\beta(\tan\theta - \tan\eta)]\ p(d)\ dd, & \text{for } \theta \geq \theta_c
\end{cases}
$$

$$(3.9)$$

Assume the cloud spacing and horizontal size both have power law distributions

given as,

$$p(s) = (u-1) \ s_{\min}^{u-1} \ s^{-u}$$
$$p(d) = (v-1) \ d_{\min}^{v-1} \ d^{-v}$$

(3.10)

where u and v are parameters, and $s_{\min}$ and $d_{\min}$ denote the minimum values of s and d, respectively. The PCLOS for a 1D domain, isosceles trapezoidal shape and power law distributions for both cloud spacing and size may be written as

$$p(\theta) = \begin{cases} (1-N) & \text{for } \theta \leq \eta \\[2ex] (1-N) \left[aF(\theta)^{v-1} - bF(\theta) + 1 \right] & \text{for } \eta < \theta \leq \theta_c \\[2ex] (1-N) \left[a - b + 1 \right] F(\theta)^{2-u} & \text{for } \theta > \theta_c \end{cases}$$

(3.11)

where $\quad a = \dfrac{\mu - 2}{(v-2)(\mu + v - 3)}, \quad b = \dfrac{(v-1)(\mu - 2)}{(v-2)(\mu - 1)}$

$$F(\theta) = \frac{\tan\theta - \tan\eta}{\tan\theta_c - \tan\eta} \quad \text{and} \quad \tan\theta_c = \frac{s_{\min}}{\beta d_{\min}} + \tan\eta$$

When θ approaches η, PCLOS goes to (1-N). When θ approaches 90°, PCLOS approaches zero. Please note that the above equations implicitly assume $u > 2, \quad u + v > 3, \quad v \neq 1, \quad v \neq 2$.

3.1.1.b 1D_sd_Power_Power_SemiEllipse

In this section we address a model that is different from the above one only with the cloud shape changed to a semi-ellipse. Cloud shape is incorporated into the model by giving different s_c and limits to the integrals in Eq. (3.7). The derivation of the s_c for

35

a semi-ellipse cloud is illustrated in Fig. 3.5. In the figure, a cloud is placed in an x-y plane with the cloud base centered at the origin of the coordinates. The cloud horizontal size is d. A line of sight that is tangent to the cloud is written as

$$y = \frac{x}{\tan\theta} + \frac{d}{2\tan\theta}(\sqrt{1+4\beta^2\tan^2\theta}) \tag{3.12}$$

By setting $x = 0$ in Eq. (3.12), we can obtain $s_c(\theta)$ for a semi-ellipse cloud as

$$s_c(\theta) = s - \frac{d}{2}(\sqrt{1+4\beta^2\tan^2\theta}-1) \tag{3.13}$$

where β is the aspect ratio ($= h/d$). By the same arguments as for the isosceles-trapezoid clouds, one can determine the integration limits for s and d for the semi-ellipse clouds

$$\begin{cases} d: & d_{min} \to \dfrac{s}{\dfrac{1}{2}\left(\sqrt{1+4\beta^2\tan^2\theta}-1\right)} \\[4mm] s: & \dfrac{d_{min}}{2}\left(\sqrt{1+4\beta^2\tan^2\theta}-1\right) \to \infty \end{cases} \qquad \text{for } \theta > \theta_c$$

$$\begin{cases} d: & d_{min} \to \dfrac{s}{\dfrac{1}{2}\left(\sqrt{1+4\beta^2\tan^2\theta}-1\right)} \\[4mm] s: & s_{min} \to \infty \end{cases} \qquad \text{for } \theta \le \theta_c$$

Assuming the same power law distributions as Eq. (3.10) for both cloud spacing and cloud size, Eq. (3.7) yields $p(\theta)$ for the "1D_sd_Power_Power_SemiEllipse" model

$$p(\theta) = \begin{cases} (1-N) & \text{for } \theta \le \eta \\[3mm] (1-N)\left[aF(\theta)^{\nu-1} - bF(\theta) + 1\right] & \text{for } \eta < \theta \le \theta_c \\[3mm] (1-N)\left[a - b + 1\right]F(\theta)^{2-u} & \text{for } \theta > \theta_c \end{cases} \tag{3.14}$$

36

where $a = \dfrac{\mu - 2}{(\nu - 2)(\mu + \nu - 3)}$, $b = \dfrac{(\nu - 1)(\mu - 2)}{(\nu - 2)(\mu - 1)}$

$$F(\theta) = \frac{\sqrt{1 + 4\beta^2 \tan^2 \theta} - 1}{\sqrt{1 + 4\beta^2 \tan^2 \theta_c} - 1} \quad \text{and} \quad \tan\theta_c = \frac{1}{2\beta} \sqrt{\left(\frac{2s_{\min}}{d_{\min}} + 1\right)^2 - 1}$$

As seen, it has the same form as Eq. (3.11), except the different form for $F(\theta)$ and $\tan\theta_c$.

Since a semicircle is a special case of a semi-ellipse, we can obtain $p(\theta)$ for

"1D_sd_Power_Power_Semicircle" model by setting $\beta = 0.5$.

3.1.1.c   1D_sd_Exp_Exp_SemiEllipse and 1D_sd_Exp_Exp_IsoscelesTrapezoid

In addition to the power law distribution one may also assume other

distributions for cloud spacing and size distributions. Here we assume exponential

distributions for both the spacing and size,

$$\begin{aligned} p(s) &= u\,e^{-us} \\ p(d) &= v\,e^{-vd} \end{aligned} \tag{3.15}$$

where μ and ν are distribution parameters. These yield the formulas for $p(\theta)$ as

$$p(\theta) = \frac{1 - N}{1 + \dfrac{\mu}{\nu} F(\theta)} \tag{3.16}$$

where $\quad F(\theta) = \begin{cases} \dfrac{1}{2}\left(\sqrt{1+4\beta^2 \tan^2 \theta} - 1\right) & \text{for semi-ellipse clouds} \\ \\ \beta(\tan\theta - \tan\eta) & \text{for isosceles-trapezoid clouds} \end{cases}$

The expression for $p(\theta)$ obtained by assuming the exponential distributions is relatively simple compared with the one assuming the power law distributions. For the power law distributions, due to the requirement of the existence of minimum values for the cloud spacing and size, $p(\theta)$ has to be divided into two parts, one for $\theta > \theta_c$ and one for $\theta < \theta_c$, while for the exponential distributions, there is no such inconvenience.

3.1.2 Poisson distributed Clouds

The aforementioned models explicitly specify the cloud size distribution (by giving $p(d)$) and characterize the cloud spatial distribution using the distance between clouds. Another way to describe a cloud field is to assume that clouds of arbitrary sizes are randomly placed on a 1D or 2D domain according to a Poisson law. Use of the Poisson distribution in PCLOS modeling was seen in the work of Kauth and Penquite (1967), where he derived a PCLOS model for a cloud field consisting of randomly distributed ellipsoidal clouds. In this section we will use his method for both 1D and 2D domains and consider cloud shapes of semi-ellipses, isosceles-trapezoids and truncated-cones, not necessarily because these shapes are better but because they yield results comparable to other PCLOS models we address in this work.

Consider a 1D domain cloud field. Each cloud in the field will cover a certain part of the domain. Assuming the domain is infinite in length, the increment in the total fractional length by adding a new cloud would be an infinitesimal $dt(\theta)$, where $t(\theta)$ is the total fractional length covered by the projections of the clouds at angle θ, which is computed by summing the fractional length contributed by every cloud and multiply-covered lengths would be counted multiply. As more clouds are added onto the line, a greater chance for overlap will occur. When overlapping cases occur, the increment in cloud cover at θ, or the increment in the probability of observing a cloud in the line of sight at θ, will be

$$dN(\theta) = \left[1 - N(\theta)\right] dt(\theta) \tag{3.17}$$

Taking the initial condition $N(\theta) = t(\theta) = 0$, rearranging and integrating (3.17), yields

$$N(\theta) = 1 - e^{-t(\theta)}$$

Since $N(\theta) = 1 - p(\theta)$, $p(\theta)$ is given as

$$p(\theta) = e^{-t(\theta)} \tag{3.18}$$

Defining $f(\theta) = t(\theta)/t(0)$, and noting that $(1-N) = p(0) = e^{-t(0)}$ enables $p(\theta)$ to be written as

$$p(\theta) = (1 - N)^{f(\theta)} \tag{3.19}$$

Since a PCLOS model of this kind assumes a Poisson distribution for the cloud spatial distribution and does not explicitly incorporate cloud size distribution, the only variable factor that can lead to variant forms of $p(\theta)$ is the cloud shape. This can be seen from Eq. (3.19) as well, where only $f(\theta)$ is unspecified.

According to the definition, $f(\theta)$ is a function of only cloud shape and should be calculated as

$$f(\theta) = \frac{\int a(\theta, r, h,...) \ p(r, h,...) \ dr \ dh...}{\int a(0, r, h,...) \ p(r, h,...) \ dr \ dh...} \qquad (3.20)$$

where r is the radius of the cloud base and h the cloud height. $a(\theta, r, h, ...)$ is the shadow area of a single cloud with the characteristic parameters r, h, and any other parameters. $p(r, h, ...)drdh...$ is the probability of a cloud with r lying between r and $r+dr$, h between h and $h+dh$, and so on.

If a cloud shape can be described by solely specifying r and h, like the simple shapes as semi-ellipse, right cylinder, et al., then $f(\theta)$ can be written as

$$f(\theta) = \frac{\int a(\theta, r, \beta) \ p(\beta) \ p(r) \ d\beta \ dr}{\int a(0, r, \beta) \ p(\beta) \ p(r) \ d\beta \ dr}$$

Here we have introduced the aspect ratio, which is defined as $\beta = h/2r$. In practice, we may further assume β is a constant. That is, all clouds can vary in their size but will keep their aspect ratio fixed. With this further assumption, $f(\theta)$ can be further simplified as

$$f(\theta) = \frac{\int a(\theta, r) p(r) dr}{\int a(0, r) p(r) dr} \qquad (3.21)$$

3.1.2.a   1D_Poisson_IsoscelesTrapezoid and 1D_Poisson_SemiEllipse

Here we follow a naming convention similar to that described in section 3.1.1. The cloud domain can be 1D or 2D. There is no need to specify the "sd/xd/cd" term, since the cloud positions are assumed to be distributed according to a Poisson distribution. Also, there is no explicit specification of the cloud size distribution for this type of PCLOS models.

Using Eq. (3.21), $f(\theta)$ for isosceles trapezoidal clouds may be written as

$$f(\theta) = \frac{t(\theta)}{t(0)} = \frac{\int [d + d\beta(\tan\theta - \tan\eta)]\, p(d)dd}{\int d\, p(d)dd} = 1 + \beta(\tan\theta - \tan\eta)$$

where d is the cloud horizontal size and $p(d)$ is probability density function for d. For semi-ellipse clouds (see Fig. 3.5), $f(\theta)$ is given as

$$f(\theta) = \frac{t(\theta)}{t(0)}$$
$$= \frac{\int \frac{d}{2}\left(\sqrt{1 + 4\beta^2 \tan^2\theta} + 1\right) p(d)\, dd}{\int d\, p(d)\, dd}$$
$$= \frac{1}{2}\left(\sqrt{1 + 4\beta^2 \tan^2\theta} + 1\right)$$

Thus, $p(\theta)$ for the 1D Poisson distributed isosceles-trapezoid clouds, denoted as "1D_Poisson_IsoscelesTrapezoid", may be written as

$$p(\theta) = (1 - N)^{1 + \beta(\tan\theta - \tan\eta)} \tag{3.22}$$

and for the "1D_Poisson_SemiEllipse" model,

$$p(\theta) = (1 - N)^{\frac{1}{2}\left(\sqrt{1 + 4\beta^2 \tan^2\theta} + 1\right)} \tag{3.23}$$

When $\beta = 1/2$, a semi-ellipse cloud reduces to a semicircle.

3.1.2.b 2D_Poisson_TruncatedCone and 2D_Poisson_Ellipsoid

The above derivation for a 1D domain also applies to a 2D domain. In this section we derive $p(\theta)$ for truncated-cone clouds randomly distributed on a 2D plane. For a truncated-cone cloud (Fig. 3.6), the shadow can be seen as a set of circles aligned along a straight line, which is the projection of the central-symmetrical axis of the truncated cone. The area of the shadow is the area within the circumference of the set of circles and can be given as

$$a(\theta) = \left(r_{cb} H \tan\theta \cos\frac{\delta}{2} + \pi r_{cb} \frac{\pi+\delta}{2\pi} \right) - \left(r_{ct}(H-h)\tan\theta \cos\frac{\delta}{2} - \pi r_{ct} \frac{\pi-\delta}{2\pi} \right)$$

where r_{cb} and r_{ct} are the radii of the base and top of the truncated cone, respectively. H is the height of the cone before being truncated, h the height of the truncated cone and δ the projection of the top angle of the cone. Rearranging the expression, noting that $H = r_{cb}/\tan\eta$, and substituting $a(\theta)$ in Eq. (3.21), $f(\theta)$ may be written as

$$f(\theta) = \frac{t(\theta)}{t(0)} = \frac{\int (r_{cb}+r_{ct})h\tan\theta\cos\dfrac{\delta}{2} + \dfrac{1}{2}\left(\pi r_{cb}{}^2 + \pi r_{ct}{}^2\right) + \dfrac{\delta}{2\pi}(\pi r_{cb}{}^2 - \pi r_{ct}{}^2)\; p(r_{cb})\,dr_b}{\int \pi r_{cb}{}^2 p(r_{cb})\,dr_{cb}}$$

$$\delta = 2\cos^{-1}\sqrt{1-\frac{\tan^2\eta}{\tan^2\theta}}\;, \qquad \cos\frac{\delta}{2} = \sqrt{1-\frac{\tan^2\eta}{\tan^2\theta}}\;, \qquad \text{(for } \theta \geq \eta)$$

(3.24)

42

To describe a truncated cone we need three parameters, (r_{cb}, r_{ct}, h) or (r_{cb}, η, β). We have set the β as a constant. Further assume η is also a constant for a given cloud field. With these assumptions and noting that $r_{ct} = r_{cb} - h\tan\theta$, and $h = 2\beta r_{cb}$ Eq. (3.24) can be written as

$$f(\theta) = \frac{4}{\pi}(1 - \beta\tan\eta)\beta\tan\theta\cos\frac{\delta}{2} + \frac{1}{2}\left[1 + (1 - 2\beta\tan\eta)^2\right] + \frac{\delta}{2\pi}\left[1 - (1 - 2\beta\tan\eta)^2\right]$$

$$(\text{for } \theta \geq \eta)$$

$$(3.25)$$

Substituting Eq. (3.25) into Eq. (3.19), one will obtain $p(\theta)$ for the "2D_Poisson_TruncatedCone" model.

As a special case, when $r_{ct} = r_{cb}$, $\eta = \delta = 0$, the truncated cone transforms to a right cylinder, and $f(\theta)$ becomes

$$f(\theta) = 1 + \frac{4}{\pi}\beta\tan\theta \qquad (3.26)$$

Thus, one can obtain

$$p(\theta) = (1 - N)^{1 + \frac{4}{\pi}\beta\tan\theta} \qquad (3.27)$$

for right cylinder clouds, where $\beta = h/2r$, r is the radius of the cylinder. If we define $\beta = h/r$, Eq. (3.27) is exactly the same as the PCLOS model used by Avaste et al. (1974) and Ellingson (1982).

$p(\theta)$ for the "2D_Poisson_Ellipsoid" and "2D_Poisson_SemiEllipsoid" models

were given by Kauth and Penquite (1967) as

$$p(\theta) = (1-N)^{\sqrt{1+\beta^2 \tan^2 \theta}} \qquad \text{for ellipsoidal clouds} \tag{3.28}$$

$$p(\theta) = (1-N)^{\frac{1}{2}\left(\sqrt{1+4\beta^2 \tan^2 \theta}+1\right)} \qquad \text{for semi - ellipsoidal clouds} \tag{3.29}$$

Eq. (3.29) is coincidently the same as Eq. (3.23) for semi-ellipse clouds in a 1D domain.

3.1.3 Regularly distributed clouds (Naber and Weinman model)

This model (Naber and Weinman 1984) is a modification of the regular

distribution model proposed by Harshvandhan and Weinman (1982). Instead of a

completely regular distribution, the model allows each row of clouds to be shifted a

fixed distance with respect to the adjacent row (see Fig. 3.8). Here we present their

resulting equations, namely

$$p(\theta) = \sum_{-2}^{2} w_i p_i(\theta) \tag{3.30}$$

$$p_i(\theta) = \begin{cases} N_i(1-\beta\tan\theta), & \text{for } 0 \le \tan\theta \le \dfrac{\left(1-\sqrt{N_i}\right)}{\beta\sqrt{N_i}} \\ (1-f)\sqrt{N_i} + fN_i(1+\beta\tan\theta), & \text{for } \tan\theta > \dfrac{\left(1-\sqrt{N_i}\right)}{\beta\sqrt{N_i}} \end{cases}$$

where N_0 = absolute cloud fraction, $N_{\pm 1} = N_0 \pm 0.05$, $N_{\pm 2} = N_0 \pm 0.1$, $w_0 = w_{\pm 1} = 0.25$

and $w_{\pm 2} = 0.125$; β is the aspect ratio; $f = x/d$, x is the shift distance of a row with

respect to the adjacent row, and d is the side length of the cuboidal clouds.

3.2 Modeling the PCLOS by tracing a line of sight

This method models the PCLOS by following a beam of light randomly incident on a cloud field. The PCLOS is the probability that the beam will pass through the cloud field without touching any clouds. In order to pass through the cloud field clearly, the beam first has to reach the cloud base level at the (1-N) portion of the sky, where N is the absolute cloud fraction. Within the (1-N) portion of the sky, the beam may fall at any point of the gap between clouds. Not all beams arriving at the (1-N) portion of the sky will pass through the entire cloud field. The factors determining whether the beam will pass the cloud field depend on the height of the nearest cloud to the right of the gap (we assume the beam direction is toward the upper right and only the nearest cloud can block the beam, see Fig. 3.7) and the horizontal distance to the cloud. Let us denote x as the distance between the beam and its nearest cloud measured on the cloud base level. Note that $0 \le x \le s_{\max}$, where $s_{\max}$ is the maximum cloud spacing in the cloud field. Given distributions for x and the cloud height h and assuming $\beta = h/d$, where d represents the cloud horizontal size, the PCLOS can be expressed as

$$p(\theta) = (1 - N) \int_{d_{\min} F(\theta)}^{s_{\max}} p(x) \int_{d_{\min}}^{\frac{x}{F(\theta)}} p(d)\ dd\ dx \qquad (3.31)$$

where $F(\theta)$ depends on cloud shape, as different cloud shapes yield different forms of $F(\theta)$. For example:

$$F(\theta) = \begin{cases} \beta(\tan\theta - \tan\eta), & \theta \ge \eta, & \text{for}\quad \text{truncated - cone}\quad \text{clouds} \\ \dfrac{1}{2}(\sqrt{1 + 4\beta^2 \tan^2\theta} - 1), & & \text{for}\quad \text{semi - ellipse}\quad \text{clouds} \end{cases} \qquad (3.32)$$

The integral in Eq. (3.31) is different from that in Eq. (3.7). The integral in Eq. (3.7) computes the cloud coverage seen at zenith angle θ, while the one in Eq. (3.31) computes the probability that a line of sight will meet a cloud that is either high or near enough to block the sight. The two models require different information about the cloud spatial distribution. Eq. (3.7) requires $p(s)$ – the distribution of the spacing distance s between two neighboring clouds, while Eq. (3.31) requires $p(x)$ – the distribution of the distance x between an arbitrary point on the line of the cloud base level and its nearest cloud (in the half plane formed by the line of sight and its vertical projection).

3.2.1 1D_xd_Weib_Power_SemiEllipse and 1D_xd_Weib_Power_IsoscelesTrapezoid

The naming convention used here is the same as that in section 3.1.1, but here we use "xd" instead of "sd" or "cd" to denote different methods of specifying the cloud spacing distribution (refer to Fig. 3.3).

Since x can take any value from 0 to s_{max} and its minimum is 0, we cannot assume a power law distribution for x, because the probability density function of a power law distribution goes to infinity at $x = 0$. The Weibull and exponential distributions do not have this restriction, so in this and the next section, we will derive $p(\theta)$ by using only the Weibull and exponential distributions to model the cloud spatial distribution. The Weibull distribution is given as (MATLAB$^{\circledR}$ statistics toolbox)

$$p(x) = abx^{b-1}e^{-ax^b} \tag{3.33}$$

46

Assuming the Weibull distribution for x and the power law distribution for cloud size, using Eq. (3.31), $p(\theta)$ for the "1D_xd_Weib_Power_SemiEllipse" model and the "1D_xd_Weib_Power_IsosceleTrapezoid" model may be written as

$$p(\theta) = (1-N)\left\{ e^{-a(d_{\min}F(\theta))^b} - (d_{\min}F(\theta))^{v-1} a^{\frac{v-1}{b}} \left[\Gamma\left(\infty, \frac{b-v+1}{b}\right) - \Gamma\left(a(d_{\min}F(\theta))^b, \frac{b-v+1}{b}\right) \right] \right\}$$

(3.34)

where $\Gamma\left(\infty, \dfrac{b-v+1}{b}\right)$ is a gamma function and $\Gamma\left(a(d_{\min}F(\theta))^b, \dfrac{b-v+1}{b}\right)$ is the incomplete gamma function. $F(\theta)$ is as defined in Eq. (3.32). The incomplete gamma function requires $b > v - 1$.

3.2.2   1D_xd_Exp_Exp_SemiEllipse and 1D_xd_Exp_Exp_IsoscelesTrapezoid

Assuming exponential distributions for both spacing and size and given as

$$\begin{aligned} p(x) &= u\,e^{-ux} \\ p(d) &= v\,e^{-vd} \end{aligned}$$

(3.35)

where μ and v are distribution parameters, $p(\theta)$ may be written as

$$p(\theta) = \frac{1-N}{1+\dfrac{\mu}{v}F(\theta)}$$

(3.36)

where $F(\theta)$ is as defined in Eq. (3.32). Eq. (3.36) has the same form as Eq. (3.16). However, since we have assumed different methods of specifying the cloud spacing

distribution, i.e., the meaning of x is different from s, the value of μ in Eq. (3.36) may be different from the one in Eq. (3.16).

3.3 The Han model

Killen and Ellingson (1994) and Han and Ellingson (1999) proposed a PCLOS model given as

$$p(\theta) = \int_{s_{min}}^{s_{max}} p(s) \int_{r_{min}}^{s^*} p(r)\, dr\, ds \tag{3.37}$$

where

$$s^* = \frac{s}{2\gamma - \gamma\beta \tan\eta + \beta \tan\theta}$$

s represents the cloud spacing measured between the centers of two neighboring clouds (see Fig. 3.3), r represents the larger radius of either the cloud top or base of a truncated cone cloud, γ is a parameter used to integrate the truncated cone and truncated square pyramid into one form. $\gamma = \pi/4$ for a truncated cone and $\gamma = 2\sqrt{2}/\pi$ for a truncated square pyramid. η is the inclination angle. The cloud aspect ratio β is defined as $\beta = h/r$.

Eq. (3.37) is in fact the probability of occurrence of a pair of adjacent clouds with spacing $s \geq r(2\gamma - \gamma\beta \tan\eta + \beta \tan\theta)$. Han and Ellingson (1999) scale the value of $p(\theta)$ at $\theta = 0$ to (1-N) and uses it to model the PCLOS. Their final expression for $p(\theta)$ is given as

$$p(\theta) = \begin{cases} 1 - N\left(1 + \dfrac{\beta \tan\theta}{2\gamma - \gamma\beta \tan\eta}\right)^{\nu-1} & \text{for } \theta < \theta_c \\[4mm] (1-N)\left(1 + \dfrac{\beta \tan\theta}{2\gamma - \gamma\beta \tan\eta}\right)^{2-\mu} & \text{for } \theta \geq \theta_c \end{cases} \tag{3.38}$$

where $\theta_c = \tan^{-1}\left[\left(N^{-\frac{1}{\nu-1}} - 1\right)\left(\dfrac{2\gamma}{\beta} - \gamma\tan\eta\right)\right]$.

49

When obtaining Eq. (3.38), the power law distributions were assumed for both the cloud spacing and radius, i.e.,

$$p(s) = (u-1) \ s_{\min}^{u-1} \ s^{-u}$$
$$p(r) = (v-1) \ d_{\min}^{v-1} \ r^{-v}$$

<div align="right">(3.39)</div>

These have the same form as Eq. (3.10). However, the spacing s in the Han model is defined differently from the spacing in Eq. (3.10), where the spacing is measured between the cloud edges, not the cloud centers. This is different when modeling the PCLOS, as measuring between cloud edges in fact makes the spacing independent of the cloud horizontal size, while measuring between centers implicitly restricted the maximum cloud size. For a given cloud spacing s, the cloud radius r has to be $r < s/2$.

The Han model makes use of the same type of information about the cloud field as the models we discussed in section 3.1, i.e. the spacing distribution, the size distribution and cloud shape. To keep naming uniformity, in the following we will refer it as the "1D_cd_Power_Power_VariableShape (Han)" model.

3.4 Chapter Summary

In this chapter, we discussed three methods of modeling the PCLOS, i.e., by computing $N(\theta)$, tracing a line of sight and the Han's method. A variety of PCLOS models were presented. All these models require geometrical information about the cloud fields. Required information includes cloud spatial distribution, cloud shape distribution, cloud size distribution (those models assuming the Poisson distribution for cloud locations do not require the specification of the cloud size distribution) and cloud shape. The cloud shapes we assumed in this chapter include:

- Isosceles-trapezoid (rectangle as a special case)
- Semi-ellipse (semi-circle)
- Truncated-cone (right-cylinder)
- Semi-ellipsoid (hemisphere)
- Ellipsoid
- Cuboidal.

In this study, all clouds in a same cloud field are assumed to have a fixed aspect ratio. Thus the cloud size distribution can be specified by the distribution of the cloud horizontal size. Assumed cloud horizontal size distributions include the power law, exponential and the Weibull distribution.

The cloud spacial distribution is specified either by the distribution of cloud locations or by the distribution of the distances between clouds (the cloud spacings). Assumed distributions include the Poisson (for cloud locations), power law (for distances), exponential (for distances) and the Weibull (for distances) distribution. Different models use different definitions of the cloud spacing. Three types of spacing

used in this study are shown in Fig. 3.3. The following is a list of the PCLOS models

we addressed in this chapter.

1D_sd_Exp_Exp_SemiEllipse   Eq.(3.16)

Model	Equation
1D_sd_Exp_Exp_SemiEllipse	Eq.(3.16)
1D_sd_Exp_Exp_IsoscelesTrapezoid	Eq.(3.16)
1D_sd_Power_Power_SemiEllipse	Eq.(3.14)
1D_sd_Power_Power_IsoscelesTrapezoid	Eq.(3.11)
1D_xd_Exp_Exp_SemiEllipse	Eq.(3.36)
1D_xd_Exp_Exp_IsosecelesTrapezoid	Eq.(3.36)
1D_xd_Weib_Power_SemiEllipse	Eq.(3.34)
1D_xd_Weib_Power_IsoscelesTrpezoid	Eq.(3.34)
1D_cd_Power_Power_VariableShape(Han)	Eq.(3.38)
1D_Poisson_SemiEllipse	Eq.(3.23)
1D_Poisson_IsoscelesTrpezoid	Eq.(3.22)
2D_Poisson_SemiEllisoid	Eq.(3.29)
2D_Poisson_TruncatedCone	Eq.(3.24)
2D_Poisson_Ellipsoid	Eq.(3.28)
2D_Poisson_Hemisphere	Eq.(3.29)
2D_Poisson_RightCylinder	Eq.(3.27)
2D_ShiftRegular_Cuboidal	Eq.(3.30)

Chapter 4

Sampling Strategy

In Chapter 3, during the development of the PCLOS models, several cloud parameters were introduced to summarize the properties of the cloud field or cloud population. All these parameters are domain-averaged or population-averaged quantities. For example, the absolute cloud fraction is a domain-averaged cloud fraction. The PCLOS is a domain-averaged value for every zenith angle. The parameters μ, ν, a, b (Chapter 3) are population-averaged values used to characterize the cloud size and spacing distributions. Thus, when estimating these parameters, one must take some sort of average, either over a large area or over a collection of individual clouds. However, the ARM cloud sensing instruments are fixed at the surface at the ARM CART site, and most can only sample the cloud field in the zenith direction. In order to estimate the appropriate spatially averaged values from these fixed-point observations, one has to assume a space-time relationship. Here it is assumed that the cloud field statistical properties do not change as the clouds move with the mean wind (the frozen turbulence approximation). Under this assumption, the appropriate domain averaged properties can be inferred from a time sequence of observations. This brings two questions: (1) For a given wind condition, over how long a period or over how many individual clouds does one need to average? (2) What sampling rate will give the most accurate estimate? In other words, given a time series of observations of a known length and sampling rate, how accurately does the average over this time series represent the domain-averaged or population-averaged value?

Answering these questions is critical to the use and interpretation of the ARM data. In previous work, Han and Ellingson (2000) assumed a 10-minute sampling period. His justification for the 10-minute averaging period was his observation of the relative consistency between two absolute cloud fraction estimates sampled using two different period lengths. Here we will investigate these questions in more depth and will attempt to establish criteria based on sampling theory. In section 4.1, a random field approach is taken to evaluate the accuracy of the measurement of the absolute cloud fraction and the PCLOS. The results are also tested with cloud fields generated by a Large Eddy Simulation (LES) or Cloud Resolving Model (CRM). Section 4.2 discusses the sampling problem of the cloud size and spacing.

4.1 The absolute cloud fraction and the PCLOS

4.1.1 A Random Field approach

As we mentioned earlier, we rely on the time sequence of vertical observations to infer the domain-averaged values of the cloud field parameters. For the cloud fraction, the ARM CART observations yield the presence or absence of clouds at the zenith. Given a series of n observations, the average cloud fraction may be estimated as

$$\hat{N} = \frac{1}{n}\sum_{i=1}^{n} N_i \qquad (4.1)$$

where N_i is an indictor function which equals 1 if a cloud is observed or 0 if clear sky is observed at observation i and i is the index of the observations. Based on the assumption of the frozen turbulence, the series of N_i's in Eq. (4.1) can be seen as a series of observations taken along a single sampling line drawn randomly on the cloud field. Our question is how many N_i do we need and what is the sampling error. To address the problem, we follow the random field approach used by Kagan (1997), Matern (1986) and Bell et al. (2001). A systematic investigation of the random field approach can be found in the monograph written by Kagan (1997).

The random field approach models a cloud field as a random process. The cloud field one actually observed is a realization of the process. When making a measurement at a point in the cloud field, one may get an ensemble of values, each corresponding to a particular realization. With this model, the mean-squared error of the estimate $\hat{N}$ (Eq. (4.1)) may be expressed as

$$D^2 = E(\hat{N} - N_a)^2 \qquad (4.2)$$

where N_a denotes the average cloud fraction for a domain of a given size. E denotes taking the average over the ensemble. For a 2D domain with area A, N_a may be expressed as

$$N_a = \frac{1}{A} \iint\limits_A N(x, y) dx dy \tag{4.3}$$

Assuming the cloud field is homogeneous and isotropic, i.e. the mean of the field is constant everywhere and the covariance depends only on the distance between the two points not on their absolute positions and orientations. Neglecting measurement error, Eq. (4.2) can be written as

$$D^2 = \sigma_{\hat{N}}^2 + \sigma_{N_a}^2 - 2\mathrm{cov}(\hat{N}, N_a) \tag{4.4}$$

where $\sigma_{\hat{N}}^2$ is the variance of the $\hat{N}$, which is a function of the length of sampling line and the number of sample points; $\sigma_{N_a}^2$ is the variance of the average over the target domain, i.e. the area for which we intend to estimate the mean using Eq. (4.1) $\mathrm{cov}(\hat{N}, N_a)$ represents the covariance between the averages over the sampling points and the one over the target domain. Kagan (1997) defined a quantity ε^2 to measure the relative error (relative to variance of the field) of representing the domain average with the sample mean, given as

$$\varepsilon^2 = \frac{D^2}{\sigma_N^2} = u_{\hat{N}} + u_{N_a} - 2w(\hat{N}, N_a) \tag{4.5}$$

where $u_{\hat{N}} = \sigma_{\hat{N}}^2 / \sigma_N^2$, $u_{N_a} = \sigma_{N_a}^2 / \sigma_N^2$, σ_N^2 denotes the variance of the cloud field.

Using a cloud classification algorithm, a 2D cloud field can be converted into a binary image with 1 representing cloud and 0 representing clear sky. For such a binary

cloud field, the variance σ_N^2 is simply $N(1-N)$, here N is the cloud fraction. The maximum variance occurs at $N = 0.5$, and the variance decreases with N departing from 0.5.

Equation 4.5 needs information about the arrangement of the sampling points and the size and shape of the target domain. For simplicity, we assume the target domain to be a rectangular area, with the sampling line located at the center of the area along the longer side of the area (Fig. 4.1). For this sampling arrangement, $u_{\hat{N}}$, u_{N_a} and $w(\hat{N}, N_a)$ may be expressed as

$$u_{\hat{N}} = \frac{\sigma_{\hat{N}}^2}{\sigma_N^2} = \frac{1}{n} + \frac{2}{n^2} \sum_{i=i}^{n-1} (n-i)\, r(i\Delta l) \tag{4.6}$$

$$u_{N_a} = \frac{\sigma_{N_a}^2}{\sigma_N^2} = 4 \int_0^1 \int_0^1 (1-x)(1-y)\, r\left(\sqrt{(Lx)^2 + (Wy)^2}\right) dx\, dy \tag{4.7}$$

$$w(\hat{N}, N_a) = \frac{\mathrm{cov}(\hat{N}, N_a)}{\sigma_N^2} = \frac{1}{n} \sum_{i=1}^{n} \int_0^1 \int_0^1 r\left(\sqrt{\left[x_i - L(x-\frac{1}{2})\right]^2 + \left[W(y-\frac{1}{2})\right]^2}\right) dx\, dy$$

$$\tag{4.8}$$

where n is the total number of the observations made along the sampling line; r denotes the correlation function of the cloud field; Δl is the interval between two consecutive observations; L and W are the length and width of the target area, respectively; x_i is the coordinate of the observation point i (see Fig. 4.1).

$\sigma_{\hat{N}}^2 = \sigma_N^2 u_{\hat{N}}$ (Eq. (4.6)) actually gives the variance of the average of n random variables with the relation between variables specified by correlation function $r(\rho)$. The continuous version of Eq. (4.6) has been give by Matern (1986)

$$\sigma_{\hat{N}}^2 = \int_0^{l_s} \text{cov}(\rho) f(\rho) d\rho \tag{4.9}$$

where $\hat{N} = \dfrac{1}{l_s} \int_C N(x, y) dl$, is the estimate of the domain mean by averaging over a curve C of length l_s. $N(x, y)$ is a realization of the random field in a 2-D plane, i.e. an isotropic cloud field. dl is the element of arc length measured along C. $\text{cov}(\rho)$ is the covariance function of the cloud field. ρ is the distance between two points chosen independently on the curve C. If C is a line segment of length l_s, the frequency function of the distance ρ is $f(\rho) = 2(l_s - \rho)/l_s^2$ where $0 < \rho < l_s$.

The most important item in Eqs. (4.6) – (4.8) is the correlation function, which describe the statistical spatial structure of the cloud field. If $r = 0$, i.e., the cloud properties at different locations are totally independent of each other, then $\varepsilon^2 = 1/n$. This is the well-known result for the average of n independent random variables. Usually the cloud properties are not spatially independent. This spatial dependence is taken into account in the above equations by the correlation function. The effects of the arrangement of the sample points and the interval between sample points enter into the above equations through the formation of the integrand.

In the above discussions it is assumed that the observations are taken on a set of points along a straight line centered in the domain. This sampling arrangement applies to the measurement of the absolute cloud fraction. Later we will give equations for the

average over a set of circles, which applies to the estimation of the PCLOS as a function of the zenith angle.

The correlation function $r(\rho)$ has the following properties: (1) $r(0) = 1$; (2) $r(\rho) = r(-\rho)$, i.e., $r(\rho)$ is an even function; and (3) $|r(\rho)| \leq r(0)$, i.e., the maximum of $r(\rho)$ occurs at $r(0)$. For a truly random process, $r(\rho)$ will usually decay to zero with increasing ρ. The shape and the rate of the decay depend on the underlying processes. Various forms of correlation functions have been suggested. Matern (1986) and Vanmarke (1983) gave some detailed discussions about the choice of the correlation function for a random field. In this study, as justified below, we assume a negative exponential form of correlation function

$$r(\rho) = e^{-\frac{\rho}{\rho_0}} \tag{4.10}$$

where ρ denotes the distance between two points, ρ_0 is a parameter which characterizes the decay rate of the correlation.

The estimated correlation functions for the cumulus cloud fields over the ARM CART site is shown in Fig. 4.2. The correlation function was estimated from the Narrow Field Of View Sensor (NFOV) data (details about the processing of the NFOV data are discussed in Chapter 5). In all, 45 days with single layer cumulus clouds present were selected from July 2000 through October 2001. The correlation functions were estimated for each of the 45 days. The mean correlation function and its standard deviation (the shadowed area in Fig. 4.2) together with the fitted correlation model (Eq. (4.10)) are shown in the figure. As seen, the observed correlation function does not approach zeros at the same rate as the negative exponential model. This may be an

indication of the existence of large-scale components in some of the cloud fields. For our intent of obtaining a directional hint on the sampling strategy, we ignore the complexity of the multi-scale structure of the cloud field, but simply assume a single-scale correlation function represented by Eq. (4.10) with $\rho_0 = 1267$ m. This value is obtained by fitting the model (Eq. (4.10)) to the mean correlation function. If the model were fit to each of the 45 cases, the average and standard deviation of ρ_0 are 1300 m and 670 m, respectively.

The standard deviation of 670 m shows the dispersion of the estimated ρ_0 for the cumulus cloud fields over the SGP. Note that there may also be errors in the estimated ρ_0. Thus, it is necessary to assess the sensitivity of the mean-squared error D^2

(Eq. (4.4)) or Root-Mean-Squared error (RMS; $= \sqrt{D^2}$) to the uncertainties associated with ρ_0. Later we will show that the variance of the average, $\sigma_{\hat{N}}^2$ ($= \sigma_N^2 u_{\hat{N}}$; Eq. (4.6)), is the dominant term in the expressions for ε^2 and D^2 for a long-sampling-line measurement. Thus, we will focus on this term to address the sensitivity problem. Substituting the correlation function (Eq. (4.10)) into Eq. (4.9), one obtain

$$
\begin{aligned}
\sigma_{\hat{N}}^2 &= \int_0^{l_s} N(1-N)e^{-\frac{\rho}{\rho_0}} \frac{2(l_s - \rho)}{l_s^2} \, d\rho \\
&= 2N(1-N)\frac{\rho_0^2}{l_s^2}\left(\frac{l_s}{\rho_0} - 1 + e^{-\frac{l_s}{\rho_0}} \right)
\end{aligned}
\tag{4.11}
$$

where N is the absolute cloud fraction; l_s is the length of the sampling line. The sensitivity coefficient which is defined as the derivative of the RMS ($\approx \sigma_{\hat{N}}$) with respect to ρ_0 can be written as

$$\frac{d(\text{RMS})}{d\rho_0} \approx \frac{d\sigma_{\hat{N}}}{d\rho_0} = K(\frac{l_s}{\rho_0}, N)\frac{1}{\rho_0} \qquad (4.12)$$

where $K(l_s/\rho_0, N)$ is a function of the scaled sampling line length and the cloud fraction. It can be seen that for a given length of the sampling line (scaled by ρ_0) the sensitivity of the RMS ($\approx \sigma_{\hat{N}}$) is inversely proportional to ρ_0.

Figure 4.3 illustrates the dependence of $K(l_s/\rho_0, N)$ on the scaled sampling line length, l_s/ρ_0 and N. The largest value of $K(l_s/\rho_0, N)$ occurs when $N = 0.5$. For sampling lines longer than $50\rho_0$, the values of $K(l_s/\rho_0, N)$ are less than 0.05 (in the unit of the cloud fraction). A 670 m standard deviation is about half the ρ_0 estimated for the cumulus cloud field over the ARM CART site. Hence, the error of $\sigma_{\hat{N}}$ due to the uncertainties in ρ_0 will be about or less than 0.025, if one take a sampling line longer than $50\rho_0$.

Figure 4.4 shows an example of ε^2, $u_{\hat{N}}$, u_{N_a} and $w(\hat{N}, N_a)$ as functions of the length of the sampling line. In this example all dimensions have been scaled by ρ_0. The size of the domain is set to $W/\rho_0 = 100$, $L/\rho_0 = 100$. The sampling line is located along L at the center of the domain. As seen from the figure, ε^2 decreases as the length of the sampling line increases. Among the three terms in the right-hand side of Eq. (4.5), $u_{\hat{N}}$ is the dominant quantity. u_{N_a} and $w(\hat{N}, N_a)$ are very small and contribute little to ε^2. Thus we may use Eq. (4.6) alone to evaluate the accuracy of the observations.

Please note that using $u_{\hat{N}}$ to approximate ε^2 only applies when the size of the target domain is much larger than the 'size' of the sampling line. Here the 'size' of the line may be thought of as the small neighborhood area around the line. Figure 4.5 shows the ratio between $\left| u_{N_a} - 2w(\hat{N}, N_a) \right|$ and $u_{\hat{N}}$, which is obtained when the target domain is set to be a square and the length of the sampling line is the same as the domain side. As can be seen from the figure, when the size of the square is larger than $30\rho_0 \times 30\rho_0$, the error resulting from the use of $u_{\hat{N}}$ to approximate ε^2 will be less than 10%.

ε^2 gives the amount of the mean-squared error D^2 relative to the variance of the cloud field. To be more specific for our goal of estimating the cloud fraction, we may define a Relative Root-Mean-Squared error (RRMS) as

$$\text{RRMS} = \frac{\text{RMS}}{N} = \frac{\sqrt{\sigma_N^2 \varepsilon^2}}{N} \approx \frac{\sqrt{\sigma_N^2 u_{\hat{N}}^2}}{N} \tag{4.13}$$

where N is the cloud fraction, RMS is the root-mean-squared error. The RRMS is a function not only of the cloud field variance, shape and size of the target domain, length of the sampling line, but also of the cloud fraction, since $\sigma_N^2 = N(1-N)$ for a binary cloud field. Figure 4.6 illustrates the RRMS as functions of the various parameters. Given a sampling line of a known length, the larger the cloud fraction, the less the RRMS will be. In other words, to achieve the same relative accuracy, one may need a longer time of observations for a cloud field with smaller cloud fraction than for a cloud field with larger cloud fraction. Please note that this statement is for the RRMS. An absolute error of 0.1 for a cloud field with $N = 0.1$ will give a RRMS of 100%, while for

a cloud field of $N = 0.9$, it will be only 11%. If we are interested in the absolute error, then the maximum will occur at $N = 0.5$.

From Fig. 4.6 one may notice that, for a cloud field with very small cloud fraction, for example $N = 0.1$, even if one uses a sampling line of $100\rho_0$, the RRMS of representing the domain mean by this line average will be as large as 40%, assuming the size of the domain is $100\rho_0$ x$100\rho_0$. As we will see later, the most frequent cloud fraction of the fair weather cumulus fields over the SGP is between 0.3 and 0.5. Thus, if we make an observation length of $50\rho_0$, we may expect a RRMS of about 30%.

The above discussion is about the length of the sampling line, and addressed the question of the accuracy one may expect for a given length of observation. Another question that needs to be addressed is the frequency of the observations. How does the sampling rate affect the accuracy of the cloud parameters? The real observations are made in a discrete fashion, and different instruments have different sampling rates. Additional observations may bring in more information about the cloud field. However, due to the correlation structure of the field, points close to each other will be not independent from each other. That is, they will contain much redundant information.

Figure 4.7 shows the RRMS as a function of the number of observations for various cloud fractions when the domain size is $100\rho_0$ x$100\rho_0$. The length of the sampling line is $100\rho_0$ and is located at the center of the domain. Observation points are regularly distributed on the sampling line with an interval $\Delta l = 100\rho_0/n$, where n denotes the total number of observation points. As shown in the figure, the error decreases as the number of the observations increases, i.e., as the sampling rate increases. However, for a sampling line of a given length, the accuracy improvement

63

resulting from increasing n has its limit. As the observation points become closer and closer, the decrease of the RRMS becomes slower and slower. The limiting value occurs when $n \to \infty$. However, when $n > 100$, or when the interval becomes less than ρ_0, the improvement of accuracy by adding more points becomes less and less noticeable.

It is well known that the variance of the average of n independent random variables with the same individual variance is given by

$$\sigma_{\bar{\xi}}^2 = \frac{\sigma_\xi^2}{n} \tag{4.14}$$

where $\bar{\xi}$ denotes the average of n independent random variables and σ_ξ^2 is the variance of the variables being averaged. Analogous to Eq. (4.14), an effective number of observations may be defined as

$$n_e = \frac{\sigma_N^2}{D^2} = \frac{1}{\varepsilon^2} \tag{4.15}$$

n_e gives an indication of the number of the independent measurements needed to achieve the same accuracy as using n correlated measurements and using Eq. (4.1) as the estimator. Figure 4.8 illustrates the relation between n_e and n. The domain size, the length and the position of the sampling line and the arrangement of the observation points is the same as that for Fig. 4.7. When $n < 30$, or the interval greater than $3\rho_0$, the linear relation roughly holds between n_e and n, which means that two observations made $3\rho_0$ apart may be considered as independent of each other. When the interval between observations become less than ρ_0, adding more observations in a given length of sampling line leads to no significant increase in n_e. Please note that this statement only

applies to the measurement of the quantities like N, PCLOS or other cloud field properties that can be assumed as functions of spatial position. For the measurement of the cloud horizontal size or spacing, the higher the sampling rate the better the measurement accuracy. (see the next section).

The PCLOS is measured from whole sky images taken at a fixed surface location. Like the absolute cloud fraction, we still have to employ the frozen turbulence approximation and rely on the horizontal advection of the cloud field to obtain an estimate of the large area average. The PCLOS is a function of the zenith angle and PCLOS(0) = (1 – N). For a certain zenith angle θ, PCLOS can be estimated from observations on a set of circles with their centers regularly aligned on the sampling line. If the PCLOS(θ) can be seen as the complementary fraction of the projections of the clouds on the cloud base plane at zenith angle θ, then the radius of the circles is $R = H \tan\theta$, where H denotes the cloud base height (Fig. 4.9).

Assuming the same correlation function given by Eq. (4.10), and all distances scaled by ρ_0, the expressions for $u_{\hat{P}}$ and $w(\hat{P}, P_a)$ for PCLOS measurement may be written as

$$u_{\hat{P}} = \frac{1}{4\pi^2 n^2}\left[\sum_{i=1}^{n-1}(n-i)\int_0^{2\pi}\int_0^{2\pi}(e^{-d_i}+e^{-d_{-i}})\,d\theta_1 d\theta_2 + n\int_0^{2\pi}\int_0^{2\pi}e^{-d_0}\,d\theta_1 d\theta_2\right] \tag{4.16}$$

$$w(\hat{P}, P_a) = \frac{1}{2\pi n}\sum_{i=1}^{n}\int_0^{2\pi}\int_0^1\int_0^1 e^{-s_i}\,d\theta\,dx\,dy \tag{4.17}$$

$$d_k = \sqrt{(k\Delta l + \rho\cos\theta_1 - \rho\cos\theta_2)^2 + (\rho\sin\theta_1 - \rho\sin\theta_2)^2} \qquad k = -i, i, 0$$

$$s_i = \sqrt{\left[x_i + \rho\cos\theta - L(x - \frac{1}{2})\right]^2 + \left[\rho\sin\theta - W(y - \frac{1}{2})\right]^2}$$

65

where n is the total number of circles along the sampling line. Δl is the interval between two consecutive centers. L and W are the length and width of the target rectangle, respectively. x_i is the coordinate of the observation point i. d_i and d_{-i} represent the distances between two points positioned on two circles with the coordinates $(x+\rho\cos\theta_1, \rho\sin\theta_1)$ and $(x+k\Delta l +\rho\cos\theta_2, \rho\sin\theta_2)$, where $k\Delta l$ is the distance between two circle centers. d_0 represents the distance between two points positioned on the same circle. s_i represents the distance between two points, one on the circle i and the other within the domain with coordinates being (x,y), $L/2 \geq x \geq -L/2$ and $W/2 \geq y \geq -W/2$. The shape of the domain is the same as that for N, thus u_{P_a} takes the same form as Eq. (4.7). Also like that for N, Eq. (4.16) and Eq. (4.17) can only be evaluated numerically.

Given the same number of observations (number of circles), one should expect a higher accuracy for the PCLOS than that for N, since the PCLOS is averaged over a circle that contains more observations than a single point. Figure 4.10 gives an example of the accuracy of the PCLOS. The domain size is once again $100\rho_0$ x $100\rho_0$. Circles with radius $R = \rho_0$, which corresponds to a zenith angle of 45° for a cloud base height ρ_0, are regularly lined along the centerline of the domain with interval $\Delta l = 0.6\rho_0$. Comparing with Fig. 4.6, we notice that for a $50\rho_0$ long sampling line, for the case of the PCLOS(0) equals 0.4, the RRMS of the PCLOS averaged over circles of radius $R = \rho_0$ is about 5% less than the that for N.

Figure 4.11 shows that the RRMS decreases with increasing circle radius (i.e., increasing zenith angle). From $\theta = 0^o$ to $\theta = 80^o$ (cloud base height equals ρ_0), an

66

accuracy increase of about 15% can be seen for PCLOS(0) = 0.4. The accuracy change

for the smaller PCLOS(0) is more significant than for the larger PCLOS(0). For

example, the change for PCLOS(0) = 0.2 is about 20%, while for the PCLOS(0) = 0.8 it

is only 5%.

In the above discussions we ignored a factor that will also affect the accuracy of

the measurement of the PCLOS. In practice, the PCLOS is estimated by averaging over

an annular ring but not a circular line. This is because the whole sky pictures consist of

pixels having finite angular resolution. Every pixel has a finite field-of-view. This field-

of-view will generate a finite "foot print" on the cloud field. Thus when taking an

average over a ring of pixels, we are actually averaging over a ring-shaped area on the

cloud field. This means that we may get a more accurate measurement than just

averaging over a circular line as modeled above. On the other hand, the size of the "foot

print" varies with the zenith angles of the pixels. A larger zenith angle corresponds to a

larger "foot print". As the zenith angle approaches 90°, the corresponding "foot print"

approaches infinity. Thus, when measuring the PCLOS, we may expect a higher

accuracy at larger zenith angles than around the zenith.

4.1.2 Application to LES/CRM simulated cloud fields

To test its validity, the technique developed above was applied to cloud fields

generated by a Cloud Resolving Model (CRM) or a Large Eddy Simulation (LES)

model. Four cloud fields are illustrated on Fig. 4.12. These are cloud fields selected for

use in the Intercomparison of Radiation Codes in Climate Models (ICRCCM) phase III

(). In the figure, (a) is a shallow sparse cumulus field simulated using data from the Barbados Oceanographic and Meteorological Experiment (BOMEX) by Siebesma and Cuijpers (1995). The domain size is 6.8 km^2 and the horizontal grid-spacing is 0.05 km. The cloud fraction is 0.16; (b) is a cloud field simulated by Bjorn Stevens (refer to the ICRCCM homepage) using observations made during the Atlantic Tradewind Experiment (ATEX). The domain size is 6.8 km^2, the horizontal grid-spacing is 0.1 km and the cloud fraction is 0.57; (c) is from Vanda Grubisic's (refer to the ICRCCM homepage) simulation of open cellular clouds. The Domain size is 50 km^2 with 0.4 km horizontal grid-spacing. The cloud fraction is about 0.92; (d) is from Grabowski et al.'s (1998) simulation of phase III of the Global Atmospheric Research Programme Atlantic Tropical Experiment (GATE), which contains very deep convective clouds and extensive anvils. The domain size is 400 km^2 with 2 km horizontal grid-spacing and the cloud fraction is about 0.46.

Figure 4.13 shows the simulated root-mean-square error, RMS*(l_s), and relative root-mean-square error, RRMS*(l_s), as function of the sampling line length and the cloud fraction N. The RMS*(l_s) and RRMS*(l_s) were evaluated in the following way: First, for each of the above four cases, the cloud field was extended by cyclically repeating it in both x and y directions. Then, for each length from a set of lengths ranging from 1 to 600 (in the unit of point) at a step-length of 5 points, we made n simulated single-line measurements. These n single-line measurements yield n estimates of the cloud fraction $\hat{N}_{l_s,i}$ ($i = 1, n$), where l_s ($= 1, 600$) is the length of the n sampling lines. The RMS*(l_s) and RRMS*(l_s) based on these n estimates of the cloud fraction were then calculated for each length as

$$\text{RMS}^*(l_s) = \sqrt{\frac{1}{n}\sum_{i=1}^{n}(\hat{N}_{l_s,i} - N)^2}$$

$$\text{RRMS}^*(l_s) = \text{RMS}^*(l_s)/N$$

where N is the desired domain-averaged cloud fraction. This procedure was repeated until the sampling line length reached 600 points. Also shown in the figure is the modeled RMS ($\approx \sqrt{\sigma_N^2 u_{\hat{N}}^2}$) and RRMS ($\approx \sqrt{\sigma_N^2 u_{\hat{N}}^2}/N$), assuming the correlation function with the negative exponential form as given in Eq. (4.10). The parameters of the correlation functions were estimated by fitting Eq. (4.10) to the mean autocorrelations of the cloud fields. The mean autocorrelation of a cloud field was obtained by averaging over 1000 autocorrelations estimated from 1000 sampling lines of 3000 points long and being randomly placed on the cloud field with random starting points and orientations. It is seen from Fig. 4.13 that, given the appropriate value of the parameter of the correlation function, the sampling error estimated using Eq. (4.13) agrees well with the simulated one.

The above calculations are based on the unit of point, i.e. the length is measured in the unit of grid point. If we take into account the size of the grid box, the same number of points will correspond to different physical length. For example the same 100 points will be translated to 5, 10, 40 and 200 km for the BOMEX, ATEX, OPENCELL, and the GATE clouds, respectively. This implies that the length of the sampling line needed to achieve certain accuracy depends on the scale of the pattern. The scale may be defined as $S = 2\int_0^{\infty} r(\rho)d\rho$ (Vanmarcke 1983; Taylor 1922), where, $r(\rho)$ is the correlation function. Among the four simulated cloud fields shown in

69

Fig. 4.12, the BOMEX field has the finest scale with $S \approx 0.32$ km. By extending the

cloud field cyclically in both the x and y directions, we actually constructed a

homogeneous cloud field of scale S ≈ 0.32 km. For this cloud field, a sampling line of

30 km (= 600 x 0.05) can achieve a RRMS of 20%, given the cloud fraction $N = 0.16$

(Fig. 4.13). On the other hand, the GATE cloud field is a simulation of a deep

convective cloud system over the Atlantic. The simulated domain is 400 km^2. The scale

of the constructed homogeneous cloud field is $S \approx 24$ km. Provided the existence of the

so constructed homogeneous cloud field, to achieve the same accuracy as for the

BOMEX cloud field, one needs a sampling line of length equaling 600 km (= 300 x 2).

4.2 The cloud horizontal size and spacing

All models developed in Chapter 3 need a value for the cloud horizontal size. Some models also need a value for cloud spacing. For the 2D models, the horizontal size is defined as the diameter of the cloud base; for the 1D models, the horizontal size is the length of the cloud base in a vertical cross section. The spacing is used in the 1D models and is also measured in a vertical cross section (or a x-z plane). Different models have different definitions of the cloud spacing (see Chapter 3).

The 1D version of the cloud size can be measured directly from the observations, as can the spacing. Error arises from two primary sources, (1) the limited sampling rate of the instruments, and (2) the limited number of clouds or spacings observed. The first error is analogous to that of measuring the length of a line using a ruler with a limited resolution. A ruler tells the integer part of the length, which is an integer increment of the ruler, but will round off the decimal part of the length and thus cause measurement error. The only difference here is that the "ruler" (the sampling line) is randomly placed on the cloud field, thus the starting edge of a cloud or a space between clouds could be at any position within a sampling interval (Fig. 4.14).

In a paper addressing the accuracy of one-dimensional systematic sampling (sampling design with random start and with equally spaced measurement along a spatial or temporal axis) and its application to the estimation of the volume of rat hearts, Mattfeldt (1989) gives an expression for the precision of the "*Cavalieri estimation of the volume of a set with constant cross-sectional area*". That is, estimating the volume of an object by integrating the profile areas of the object on a series of equally spaced cut sections.

Appling the same ideas to our cloud size and spacing measurement, the RRMS error of measuring a cloud base size or spacing using the periodic sampling method may be written as

$$RRMS = \frac{\sigma_D}{D} = \frac{\sqrt{[d - rem(D,d)]\, rem(D,d)}}{D} \qquad (4.18)$$

where σ_D is the standard deviation of the cloud size. D is the real length of the cloud base or spacing between clouds. d is the sampling interval. "*rem*" denotes the remainder of D divided by d. If the cloud size is exactly an integer times the interval, the error will be zero. This is illustrated in Fig. 4.15, where the RRMS is plotted as a function of D, with the interval d set to 25. Also shown on the figure is the upper limit of RRMS, which is

$$RRMS \leq \frac{d}{2D} \qquad (4.19)$$

Eq. (4.19) indicates that the error is proportional to the interval distance, or inverse of the sampling rate. Thus for the measurement of the cloud size or spacing, the higher the sampling rate the less the sampling error. At the ARM CART site, the Micro-Pulse Lidar (MPL) has a sampling interval of 20 seconds. If we assume the wind speed is 10 m/s, then the standard error (standard deviation) of the MPL due to the limited sampling rate will be less than $d/2 = 100$ m. The sampling interval of the NFOV is 1 second, thus the standard error of the NFOV due to the limited sampling rate will less than 5 m for a 10 m/s wind speed.

The second error is connected to the number of clouds or spacings observed. The variance of the mean of n independent samples is $\sigma_{\bar{D}}^2 = \sigma_D^2 / n$, which depends on

the population variance σ_D^2 and *n*. Noting that the RRMS can be written as

$$RRMS = \sigma_{\bar{D}} \Big/ \overline{D} \, ,\text{ then } n \text{ can be related to RRMS by } n = \left(\sigma_D \Big/ \overline{D} \cdot RRMS \right)^2 .\text{ For the}$$

cumulus clouds over the SGP, the standard deviation of the cloud size σ_D is about

1500 m (Chapter 5) and $\overline{D}$ is about 1000 m, thus to achieve a RRMS less than 20% one

needs n ≥ 57. That is, at least 57 cloud samples are needed to achieve 20% accuracy in

measurement of the mean cloud size.

For the 2D version of the cloud size, beside the aforementioned two errors, there

is another source of error when inferring the cloud size from the observations made on a

line. Because the observations only yield a set of chord lengths, one has to derive the

cloud base size from the chord lengths. This process will induce new uncertainties into

the estimated cloud size. The problem turns out to be very complicated, and the same

problem is the subject of the study in "stereology", which by definition is "*a body of*

mathematical methods relating three-dimensional parameters defining the structure to

two-dimensional measurements obtainable on sections of the structure" (DeHoff &

Rhines 1968; Weibel 1979). Although a few methods for such estimates have been

developed, at least at present, all the methods are based on an assumption that the

objects, for which we intend to obtain the parameters, are of simple shape, like spheres,

ellipsoids or at least convex solids. A convex solid is a solid for which any line segment

connecting any two points in the solid lie totally within the solid. In other words, a line

traversing the solid forms only one chord or intercept. This is the main difficulty when

trying to apply the methods to measurement of the cloud size, since the shapes of the

cloud base are not convex. This is a very complex problem that requires much more

work. In this study, we simply approximate the cloud diameters with the observed chord lengths. The mean of the cloud diameters is approximated by the mean of the chord lengths and the distributions of the cloud diameters are also approximated by the distributions of the cloud chord lengths (see Chapter 5).

4.3 Chapter summary

In this chapter, we discussed methods of assessing measurement accuracy of the various cloud field properties. For cloud fraction, a random field approach was used to address the sampling problem. A cloud field is modeled as a homogeneous random process. Assuming the frozen turbulence approximation, a time series of observations can be considered as a series of observations taken along a spatial line randomly drawn in the cloud field. The accuracy of the estimation of the domain average from the average of observations on the sampling line can be expressed as a function of the correlation function of the cloud field, the length of the sampling line and the cloud fraction.

The correlation function is the key factor in the assessment of the measurement accuracy. It gives information about the spatial structure and the scale of the cloud field. A negative exponential form of correlation function is assumed in this study. Using the NFOV observations, the correlation functions for the cumulus cloud field over the ARM CART site were estimated and a model correlation function was obtained by fitting to the mean of these correlation functions. The e-folding parameter of the correlation function was estimated to be $\rho_0 = 1267$ m. For a long-sampling-line measurement, given the relative length of the sampling line with respect to ρ_0, the sensitivity of the predicted measurement error is inversely proportional to the scale of the cloud field. For our case i.e., the cumulus cloud field over the SGP, a 50% uncertainty in the estimated ρ_0 may result in an error of about 0.025 (cloud fraction unit) in the predicted measurement error, which is negligible for most of the cases except for cloud fields with $N \leq 0.1$.

Given the form of the correlation function and the value of ρ_0, for the most frequent shallow cumulus fields ($N = 0.3$ to 0.5) over the ARM CART site, one may expect a RRMS of about 30%, for an observation length of about 60 km ($\approx 50\rho_0$). Assuming a 10 m/s wind speed, the spatial length of 60 km corresponds to a time span of 100 minutes. Due to the limited life span of the shallow cumulus clouds and requirement of the frozen turbulence approximation i.e., the statistical properties of the cloud fields do not change with the advection of the cloud field, 100 minutes may be a practical compromise between the accuracy and the changing characteristics of the cloud field with time.

Also defined in this chapter is the effective number of observations. It gives the number of independent observations that would yield the same accuracy as a number of correlated observations. Its counterpart in the time domain is the effective sampling rate.

The absolute cloud fraction N is a special case of the 1 - PCLOS(θ), which occurred when $\theta = 0^o$. The sampling problem of the PCLOS can be addressed using the same technique developed for N. For any $\theta > 0^o$, there are more sampling points available for the estimation of the PCLOS than for the absolute cloud fraction, since the PCLOS is estimated by averaging over the circumference of a circle. Thus, one may expect a higher accuracy for the PCLOS than for N, given that the two were sampled at the same rate.

The technique was tested on four LES/CRM generated cloud fields. Given the appropriate estimates of the parameter of the correlation function, the technique can yield reasonable predictions of the measurement error.

The cloud size and spacing need a different approach to assess their measurement errors. For a single cloud, the error in measurement of the horizontal size through randomly started periodic sampling is less than $d/2$, where d is the spatial interval corresponding to a time step of the sampling instrument. To assess the accuracy of the estimated mean of the cloud base size and spacing, one may employ the central limit theorem and the number of clouds observed can be related to the RRMS by

$n = \left(\sigma_D \middle/ \overline{D} \cdot RRMS \right)^2$. The problem of inferring the cloud diameter from the measurements of the cloud chord lengths is important but is not addressed in detail in this study, due to the complexity of cloud shapes. Here the average cloud diameter and the diameter distribution are approximated by the mean of the observed chord lengths and their distribution, respectively.

Chapter 5

Extraction of Cloud Parameters and Comparison between Models and Observations

To determine whether the PCLOS models are valid for an actual cloud field, we need to extract the necessary model parameters from observations and compare the model PCLOS with the observed PCLOS. Table 5.1 summarizes the various parameters used by the PCLOS models we consider in this study. Each model has different parameters. The number of parameters ranges from one for the "2D_Poisson_Hemisphere" model to eight for the Han and Ellingson (1999) model (the "1D_cd_Power_Power_VariableShape" model). To facilitate the following discussion, we group the models into two groups based on the information required by the models:

Group-1: Models require the cloud spatial distributions to be specified by the

distribution of the distances between clouds or the distances between an arbitrary

point to its nearest cloud. The cloud size distribution is also explicitly required. All

Group-1 models are 1D model. Examples are:

- 1D_xd_Weib_Power_SemiEllipse,
- 1D_sd_Exp_Exp_IsoscelesTrapezoid, and
- 1D_cd_Power_Power_VariableShape(Han).

Group-2: Models assume clouds are randomly or regularly distributed in a cloud field.

The cloud size can be arbitrary. The domain can be 1D or 2D. Examples are:

- 1D_Poisson_IsoscelesTrapizoid,
- 2D_Poisson_Hemisphere, and

- 2D_ShiftRegular_Cuboidal (uniform cloud size)

The Group-1 models explicitly specify the cloud size distributions; hence they usually need more parameters than the Group-2 models (see Table 5.1). Those models which assume the cloud shape as truncated-cone or isosceles-trapezoid have one more parameter, η, the inclination angle, than the other models.

In this chapter, we will first develop a technique to obtain the PCLOS using the time series of sky images taken at the ARM CART site. We will also derive the various cloud parameters listed in Table 5.1 from the ARM surface cloud observations and make a comparison of the model PCLOSs with the observed PCLOS.

Table 5.1 PCLOS Model Parameters.

2D_Poisson_Hemisphere	N
1D_Poisson_SemiEllipse 2D_Poisson_SemiEllipsoid 2D_Poisson_Ellipsoid 2D_Poisson_RightCylinder	N, β
1D_Poisson_IsoscelesTrapizoid 2D_Poisson_TruncatedCone	N, β, η
2D_ShiftedRegular_Cuboidal	N, β, f
1D_xd_Exp_Exp_SemiEllipse 1D_sd_Exp_Exp_SemiEllipse	N, β, μ, ν ; μ : parameter of the Exponential distribution for cloud spacing. ν : parameter of the Exponential distribution for cloud size.
1D_xd_Exp_Exp_IsoscelesTrapezoid 1D_sd_Exp_Exp_IsoscelesTrapezoid	N, β, μ, ν, η ; μ, ν : same as the Exp-Exp-SemiEllipse model.
1D_xd_Weib_Power_SemiEllipse	$N, \beta, a, b, \nu, d_{\min}$; a, b : parameters of the Weibull distribution for cloud spacing ν : parameter of the Power Law distribution for cloud size.
1D_xd_Weib_Power_IsoscelesTrapezoid	$N, \beta, a, b, \nu, d_{\min}, \eta$; a, b, ν : same as the Weibull-Power-SemiEllipse model.
1D_sd_Power_Power_SemiEllipse	$N, \beta, \mu, \nu, s_{\min}, d_{\min}$; μ : parameter of the Power Law distribution for cloud spacing. ν : parameter of the Power Law distribution for cloud size.
1D_sd_Power_Power_IsoscelesTrapezoid	$N, \beta, \mu, \nu, s_{\min}, d_{\min}, \eta$; μ, ν : same as the Power-Power-SemiEllipse model
1D_cd_Power_Power_VariableShape (Han)	$N, \beta, \mu, \nu, \gamma, s_{\min}, d_{\min}, \eta$; μ, ν : same as the Power-Power-SemiEllipse model. γ : parameter control the shape of the cloud.

Where N is the absolute cloud fraction; β is the cloud aspect ratio; η is the inclination angle of the cloud; $s_{\min}$ and $d_{\min}$ are the minimum cloud size and cloud spacing, respectively. Models are named with the pattern (1D/2D)_E_C or (1D/2D)_(xd/sd/cd)_A_B_C, where E represents the spatial distribution of the clouds; C represents the assumed cloud shape; A represents the cloud spacing distribution; B represents cloud size distribution. 'sd' means the spacing distribution is specified for, s, the distance between two clouds measured between the edges of two adjacent clouds(refer to Fig. 3.3). 'xd' means the spacing distribution is specified for, x, the distance from an arbitrary point to it nearest cloud to the right. 'cd' means the cloud spacing is measured between centers of two adjacent clouds.

5.1 Determining the PCLOS from the Time Series of Sky Images

The PCLOS is by definition the probability of a line of sight passing through a cloud field at a certain zenith and azimuth angle without being blocked by any clouds. Assuming an isotropic cloud field, the PCLOS is a function of only zenith angle, θ. A whole sky image can give us a snap shot of the sky condition at all zenith angles from the zenith to the instrument horizon. If we have simultaneous whole sky images at many different locations over a large area, the PCLOS as a function of θ can be estimated by taking an average over these images. Since at the ARM CART site, we only have one site with images of the sky condition, we use a time average to replace the area average That is, we approximate the spatial average by taking an average over a time series of whole sky images at one location to infer the PCLOS(θ).

There are two whole-sky-imaging instruments available at the ARM CART site, a Total Sky imager (TSI) and a Whole Sky Imager (WSI). Fig. 5.1 shows an example of the TSI and WSI cloud decision images. The horizontal area of the cloudy sky seen by the imager's FOV is a function of the cloud height: $D = 2H \tan\left(\dfrac{FOV}{2}\right)$, where D is the diameter of the cloudy sky within the FOV and H is the cloud height. As an example, assuming the cloud height is 1.5 km, a 160° FOV imager can see a patch of cloud field with a diameter of 17 km.

Estimation of the PCLOS requires a mapping function that relates the zenith angle to the radial distance of an image point away from the picture center. The WSI function was determined by ARM personnel as part of its calibration. We make use of the sun's position to estimate this function for the TSI. During the summer, at the ARM

SGP site, the solar zenith angle approaches 10° at solar noon, Thus it is possible to calibrate the TSI mapping function by using solar position information on clear days. To perform the TSI calibration, we selected seven clear days in May and June, 2001. For each day, the sun's zenith angles and the corresponding pixel positions were recorded from the time-lapse TSI images. The mapping function was obtained by fitting a cubic curve to the data from the seven-day period. Fig. 5.2 shows the mapping function for the TSI. The fitted curve is slightly diverging from a linear relationship.

Using the time-lapse TSI images for a sampling period of about 100 minutes, the temporal fraction of the occurrence of clear sky for every pixel position was estimated. This estimates the PCLOS at all azimuth and zenith angle within the instrument FOV. PCLOS(θ) is obtained by averaging over azimuth angle within each $1°$ annular ring from zenith to the instrument horizon. The same processes were also applied on the WSI images.

Figure 5.3 shows the differences between the PCLOS estimated from the WSI and the TSI. When estimating the PCLOS, the images from the TSI and the WSI are taken from the same sampling period but with different sampling rates. The result is an average of 77 cases of single layer fair weather cumulus cloud fields obtained over the ARM CART site (there are 86 cases when TSI data are available, but the WSI data are available for only 77 of these). From the figure, we notice that below 60° the $PCLOS_{WSI}$ agree well with the $PCLOS_{TSI}$ with a standard deviation of about 0.07 (in cloud fraction unit). While above 60°, the WSI tends to give larger cloud fraction (or smaller PCLOS). This may be caused by the classification of heavily loaded haze or

dust into cloud by the WSI's cloud classification algorithms. (private communication with Chuck Long, Pacific Northwest National Laboratory (PNNL)).

The standard deviation (the width of the grey stripe along the blue line) is mainly caused by the different temporal resolutions of the TSI and the WSI. The time-lapse images are taken every 6 minutes by the WSI and every 20 seconds by the TSI. For a one-hour time interval, one may get 180 TSI images, but only 10 WSI images. This makes the $PCLOS_{TSI}$ smoother than the $PCLOS_{WSI}$. From the figure we also notice that the standard deviation decreases slightly with the zenith angle increasing from 0 to 35°, this is expected, since the zenith-angle rings at small angles cover less sky area than at larger zenith angles. However, above the 35°, this decreasing trend doesn't continue. This is probably because the differences between the cloud decision algorithms used by the TSI and the WSI.

Figure 5.4 shows $p(\theta)/(1-N)$ for the 86 cases derived from the TSI data. This normalized PCLOS is the conditional probability of a clear line of sight given that the line of sight reaches the cloud base level in the (1-N) portion of the cloud field. Alternatively, $1 - p(\theta)/(1-N)$ is the probability of seeing cloud sides at an angle θ given that the line of sight reaches the cloud base level in the (1-N) portion of the cloud field. The curve changes from 1 as the zenith angle increases depending on the fraction, distribution, size and shape of the clouds as was discussed in Chapter 3. Note that some cases have the conditional probability larger than 1 at some angles. This is likely caused by the presence of a cloud streak or an inhomogeneity in the cloud field.

5.2 Determining the Absolute Cloud Fraction

The absolute cloud fraction, N, is defined as the fractional area of the vertical projections of the clouds on the surface. Without large area imagery data over the ARM CART site, we infer the absolute fraction by applying the frozen turbulence assumption to the zenith pointing instruments. In other words, we assume the cloud field properties do not change significantly as the clouds advect over the site with the mean wind speed. The absolute cloud fraction is estimated as $N = L_c/L_{tot}$, where L_{tot} is the total length of a time series of observations and L_c is the summation of the lengths of the cloud segments. If wind speed does not change during the observation time, the above equation is equivalent to

$$N = \frac{M_c}{M_{tot}} \tag{5.1}$$

where M_c is the number of times when the instrument see the clouds and the M_{tot} is the total number of observations during the period.

Several instruments at the ARM CART site have the potential to be used to infer N because they are sensitive to the presence of clouds and they generate time series of observations. These instruments include the TSI, WSI and a Narrow Field Of View sensor (NFOV). When using TSI and WSI data, N is estimated as the fractional number of cloudy pixels within the 20° circle around the zenith during the observation period. Details concerning the NFOV data processing are given in the following section. Eq. (5.1) was used when inferring N from the NFOV data.

Besides these three instruments, there is also an ARM value-added data product, the Active Remotely-Sensed Clouds Locations (ARSCL), that can be used to obtain N.

The ARSCL product contains a time series of estimates of the cloud base height, which are generated by ARM from ceilometer and Micro-Pause Lidar (MPL) data following a technique developed by Clothiaux et al. (2001). For every times in the ARSCL time series, if there is one or more clouds detected, a positive value denotes the lowest cloud base height observed; otherwise, a negative value marks the clear condition at the time of observation. Like that for the NFOV, N is estimated from the ARSCL cloud base data by using Eq. (5.1).

Figure 5.5 shows a comparison of the N's estimated from the four techniques (N_{TSI}, N_{WSI}, N_{NFOV}, N_{ARSCL}). As seen in the plot, N_{WSI} agrees well with N_{TSI}. The variance between N_{TSI} and N_{WSI} is mainly due to the different sampling rates of the two instruments, as noted previously. Among the four methods of inferring N, N_{NFOV} and the N_{ARSCL} tend to overestimate the cloud fraction by about 20% relative to N_{TSI} or N_{WSI}. The cause of these biases may be due to the sensitivity of the instruments to the various clouds and the cloud decision algorithms used to infer cloudiness. The TSI and the WSI detect only visible and relatively thick clouds, while the NFOV and the laser instruments are sensitive to thin and sub-visible high clouds. This can also explain the trend that is illustrated in the histograms of the N's (Fig. 5.6), where the NFOV and ARSCL tend to have more occurrences of larger cloud fraction. Since our interest is on checking models of near opaque clouds, we are most interested in occurrences of thicker clouds. Furthermore, by using the TSI we can get a wider field-of-view and higher time resolution than with the other instruments. Thus, in this study, we will take the N_{TSI} as our best estimate of the absolute cloud fraction.

5.3 Determining the Cloud Thickness

There are three instruments, a Microwave Millimeter Cloud Radar (MMCR), the MPL and a Vaisala Ceilometer (VCEIL), at the ARM CART site that were designed to profile the cloud field with high temporal and spatial resolutions. The laser instruments infer the cloud variables from measuring the backscattered laser energy. The cloud height is determined from the time delay between the transmitted pulse and the backscattered signal. The MMCR has the same physical principle except it employs microwave energy.

Each type of instrument has advantages and limitations. The laser instruments are capable of detecting almost all clouds, thin or thick, high or low, water or ice, if only the clouds are in the detection range of the instruments. However, the laser energy is easily attenuated by the cloud droplets, hence, they are usually unable to penetrate the cloud and detect the cloud top.

The strength of the MMCR is its ability to penetrate clouds and detect multiple cloud layers aloft, but it is not very sensitive to clouds composed of small hydrometeors. At the ARM CART site, there is also a special MMCR problem that is caused by large amounts of nonhydrometeor particulates, such as insects and bits of vegetation, suspended in the atmosphere. Since the MMCR is very sensitive to these relatively large particulates and this airborne clutter may reach as high as 3 km during summer season, the real hydrometeor returns from lower clouds may be totally hidden by noise from the clutter and thus make the low clouds that are immersed in the clutter practically undetectable.

In addition to the cloud base data mentioned in the previous section, the ARSCL product also contains estimates of cloud top which were obtained by combining the data from the MMCR, laser ceilometer, micro-pulse lidar, and microwave radiometer, although they are labeled as "*More work may need to be done here, so be very careful with this variable*" (Clothiaux et al. 2001). An example of the ARSCL cloud height data is shown in Fig. 5.7. In the figure, the upper panel shows the cloud bases and tops, and the lower panel shows the histogram of the cloud thicknesses corresponding to the upper panel. The thicknesses are evaluated for every observation moment by subtracting the cloud base heights from the corresponding top heights. The mean thickness for this case is 475 m and the standard deviation is 205 m.

When clutter is present, the ARSCAL data may report an incorrect cloud top. Figure 5.8 gives an example. In addition to the ARSCL cloud base and top data shown in panel (c), panels (a) and (b) show the relative humidity profiles from the Raman Lidar (RL) and radiosondes, respectively. Panel (d) shows the MMCR reflectivity data obtained during the same period as the profiles. The ARSCL cloud top is around 3600 m, which matches the MMCR reflectivity top. While the RL or the radiosonde relative humidity profiles show that, around 2300 m, there is a rapid decrease of the relative humidity and, above 2500 m, the relative humidity has decreased to lower than 40%. Under this circumstance, we assume the cloud top is no higher than the level where the relative humidity decreased to 60%. This method is based on Slingo's research (1980, 1987) and has been used by Han and Ellingson (1999). In this study, we first use the ARSCL cloud top data to calculate a first guess of the cloud thickness, and then, this thickness is checked with the relative humidity profiles if available. If the

87

relative humidity profiles do show a rapid decrease, i.e., the relative humidity decreases more than 40% within a 500 m height, and if the level where this decease occurs is very different from the ARSCL cloud top (>300 m), then we take the level where the relative humidity decreases to about 60% as the final cloud top.

The histograms of the cloud thicknesses obtained before and after taking into account the relative humidity information (Fig. 5.9) show that the correction based on the relative humidity profiles mainly eliminates some larger cloud thicknesses reported by the ARSCL data, which we think are mainly caused by the submersion of the clouds in a large amount of nonhydrometeor particulates. Also seen from Fig. 5.9 is that for the fair weather cumulus over the SGP site, the most frequently occurring cloud thickness is less than 500 m.

Since for many cases we have to rely on the relative humidity profiles to infer the cloud thicknesses, we lose detailed information about each cloud and cannot obtain the distribution of the cloud thickness for each selected cloud field. To give a rough picture of the range of variation of the cloud thickness, we use either the standard deviation, if the thickness is calculated solely using the ARSCL data, or half of the changing-range of the heights of the 60% relative humidity, if the thickness is inferred from the relative humidity profiles, as a measure of the cloud thickness variation. Fig. 5.10 illustrates the histogram of the relative thickness variation (thickness variation to cloud thickness). The mode is around 40%, which may be taken as the uncertainty of characterizing the thickness population of a cloud field using the average value.

Most PCLOS models require the cloud aspect ratio, which by definition is the ratio of the cloud thickness to its horizontal size. The aspect ratio is a characteristic

quantity of each individual cloud, and has its own distribution for a given cloud field.

However, not only is it impossible, under current conditions, to obtain the detailed

distribution of the aspect ratio, but PCLOS models have yet to take this into account.

That is, all of them assume the aspect ratio to be a constant for a given cloud field. In

this study, for each case, the aspect ratio is estimated as the ratio of average cloud

thickness to average cloud horizontal size. Fig. 5.11 shows the histogram of the so

obtained aspect ratios. Most cases have $\beta < 1$. The mean and median values are 0.65

and 0.43, respectively. The fair weather cumulus over the SGP are relatively thin

compared with those over Florida (Plank 1969), where Plank observed a typical aspect

ratio of 1 to 2. This is quite likely due to the differences in surface forcing and water

content of the atmosphere between two locations

5.4 Determining the Cloud Spacing and Horizontal Size Distribution

The requirement of information about cloud sizes and spacings is one of the main differences between the broken and the unbroken-plane-parallel cloud radiation problems. In this study, assuming that the cloud field properties do not change significantly as they move at mean wind speed, the spacings and horizontal sizes are estimated as the products of wind speed and time lengths of observations. This is a one-dimensional estimate of the cloud horizontal sizes and spacings.

Observational issues are the sampling rate and the field-of-view (FOV) of the instruments. Too small a sampling rate may cause the instrument to miss small clouds or cloud spaces, whereas too wide FOV will smear the cloud boundaries. As seen from Table 2.1, the NFOV has a relatively high sampling rate (1 measurement per second) and a narrow FOV (5.7°). Thus, the NFOV was chosen to measure the cloud horizontal sizes and spacings in this study. The step length between sampling points is a function of wind speed. For typical conditions at the CART site, the wind speed is about 10m/s, which corresponds to a step length of 10 m. The size of viewing area within the FOV is a function of height. For a cloud base of 1.5 km, the aperture diameter of the area is about 150 m. Fig. 5.12 gives an example of the NFOV data, which is a time series of downward diffuse spectral radiance at a wavelength of 869 nm.

For a time interval of less than two hours, the clear sky solar diffuse radiance at 869 nm can be assumed to be a constant or only change linearly with time. This greatly simplifies our determination of the threshold for identifying the cloud segment of the signal. To determine the threshold, we first use the VCEIL data to find the times when the VCEIL doesn't see any cloud. A first-guess threshold for the clear-sky NFOV

radiance data is determined by fitting a line to the NFOV data corresponding to the clear VCEIL periods.

Because the two instruments are not located at exactly the same point on the ground and may not be synchronized well with each other, the VCEIL and NFOV don't see exactly the same volume and may report different sky conditions on some occasions. In other words, at some moments the VCEIL reported clear sky but the NFOV gave cloudy radiances. When this occurs, the aforesaid method cannot find the real clear sky radiance (the green signal shown in Fig. 5.12), but will generate a threshold that is higher than the clear-sky radiance. The real clear-sky radiance will lie between this fist-guess threshold line and zero radiance. In order to get a better estimate of the clear-sky background, our algorithm allows the aforesaid first-guess threshold line to move between the VCEIL-determined threshold and zero radiance.

As mentioned earlier, for a period of one or two hours, the clear-sky solar diffuse radiance is almost constant or changes linearly with time. Also, at 869 nm, the diffuse radiance from a cloud is quite different from that from the clear background. That means, when a cloud moves into the FOV of the NFOV, there will be a big jump in the time series of radiance data. If the clear-sky radiance is really constant, when moving the threshold line in a small neighborhood around the clear-sky radiance value, the number of the points located on the threshold line, i.e., with their radiance equal to the threshold value, will be always be zero unless the threshold line is placed exactly on the value of the clear sky radiance. This way we can find the desired clear background radiance value.

In practice, the clear-sky radiance is not a constant. When moving the threshold, the number of points on the line will be a function of the threshold value. However there must be a maximum between zero and the first-guess threshold. In our algorithm, this position is defined as the clear-sky background. The new threshold line is then set at a position where it is 0.015 w/m^2/nm/sr above the clear-sky background. This is the red line shown in Fig. 5.12. Values greater than the threshold are counted as from cloud. If the clear-sky radiance changes with time, a slope is determined from the data and the slope is taken into account in the aforementioned process of finding the clear sky radiance.

The wind speed at the height of the cloud layer is obtained from measurements by the ARM 915 MHz Radar Wind Profiler (RWP915). The radar data provide 1-hour averaged wind profiles from 0.1 km to 5 km with accuracy of 1 m/s compared with the winds from the balloon borne sounding system. The time-nearest available radar wind profile is used to estimate the wind speed. Fig. 5.13 shows the histogram of the wind speeds obtained for all 93 selected cases. In general, the wind speed is between 1 and 20 m/s. The mode is about 7 m/s.

It should be noted that the sizes and spacings obtained by the above technique are only the cloud chord and gap lengths from a one-dimensional transect of the cloud field. Thus, when we say 'cloud size' in the text, we actually mean the so obtained chord length. Figure 5.14 (a) and (b) show the distributions of the inferred cloud spacings and horizontal sizes, respectively, for all cases. The stair step line in the figure is the histogram of the spacings and sizes. Cloud sizes and spacings are grouped in a set of log-scale bins. In Fig. 5.14, the ordinate values of the histogram have been scaled to

the number of counts per unit length (= Number of counts in a bin / Bin width). When estimating the cloud size and spacing, we have neglected those segments less than 50 m. Thus the minimum value in the figure is 50 m for both the size and spacing.

As seen in the figure, both the size and spacing distributions are asymmetric and have long tails. Also shown in the figure are four maximum-likelihood-fitted theoretical distributions including the power law distribution, the Weibull distribution, the exponential distribution and the lognormal distribution. The power law distribution appears as a straight line in the log-log plots. It doesn't fit the observed cloud size and spacing distributions very well. The Weibull distribution works fine in the range from 600 – 3000 m. Since the exponential distribution is a special case of the Weibull distribution, it has roughly the same performance as the Weibull distribution. Generally, the lognormal distribution gives the best overall fit.

Figure 5.15 shows the cloud size histogram for cloud fractions grouped into three groups, 0 – 0.3, 0.3 – 0.6 and 0.6 – 1. Here the y-axis is a linear scale. The area under the histogram corresponds to the total number of cases in the cloud-fraction group. From the figure, we may notice a slight mode at around 100 – 200 m for the cloud size distributions, especially for small cloud amount cases. Since we obtained the chord length, the real cloud horizontal scale may be different. A relationship between the chord length and a characteristic horizontal scale only exists for very simple geometrical shapes, such as a circle. If we assume the cloud base is a circle and define the diameter, D, as the characteristic scale of the circle, then, the average of the randomly selected chord lengths, L, can be related to D by $D = 1.5L$ (Mathai 1999).

Thus, the most frequently occurring fair weather cumulus over the ARM SGP site have horizontal sizes in the range of about 200-300 m.

To obtain information about the range of variation of the cloud size and spacing for every case, we calculated the median and the 20th and 80th percentile values for every case and display them in Fig. 5.16 and Fig. 5.17. For most selected fair weather cumulus cases, the average (median value) cloud sizes and cloud spacings are less than 1000 m and 2000 m, respectively. Like the population for all the selected cases, the populations of the size and spacing for every individual case also have the asymmetric distributions (refer to Fig. 5.14), which are indicated in the upper panels in Fig. 5.16 and Fig. 5.17 by the unequal whisker lengths for the 20th and 80th percentiles, respectively. The average ranges between the 20th and the 80th percentiles for the cloud size and spacing are 1000 m and 2000 m, respectively, which are the same order of magnitude as the values of themselves.

Finally we will estimate the spacing and size distribution parameters for every case. These parameters are closely associated with the theoretical distributions used to model the cloud spacings and sizes. Different theoretical distributions have different parameters (refer to Table 5.1). Among the four theoretical distributions mentioned in the preceding text, we use three of them in this study. They are the exponential, the power law and the Weibull distributions. Although it may fit the data better, the lognormal distribution was disregarded because it is difficult to use in a PCLOS model.

As discussed in chapter 3, we addressed three types of cloud spacings in a 1D section of the cloud field (refer to Fig. 3.3). These are: (1) spacing is measured between the edges of two adjacent clouds, i.e., the "sd" type; (2) spacing is measured between an

arbitrary point and its nearest cloud in the view direction, i.e., the "xd" type; and (3)

spacing is measured between cloud centers of two adjacent clouds, i.e., the "cd" type.

Each may assume various distributions, the possible combinations of which are shown

in Table 5.2.

Table 5.2 Combinations of types of the cloud spacing and their assumed distributions. Where 'X' means a possible combination. For example, the "sd" type of spacing may assume the exponential, the power law and the Weibull distributions.

	Exponential $p(x) = \mu e^{-\mu x}$	Power law $p(x) = (\mu - 1)x_{min}^{\mu - 1} x^{-\mu}$	Weibull $p(x) = abx^{b-1}e^{-ax^b}$
"sd"	X	X	X
"xd"	X		X
"cd"	X	X	X

As seen from the Table 5.2, for cloud spacing, we may have eight combinations.

Each exponential or power law distribution has one parameter, and each Weibull

distribution has two parameters. Thus, for cloud spacing, there are 11 parameters.

Counting the 4 parameters for the cloud size distributions (two for exponential and

power law and two for Weibull), there are 15 parameters in total that need to be

estimated from the data.

The "cd" type spacing is measured between an arbitrary point and its nearest

cloud. When inferring its distribution, a random number was first generated in the range

from 0 to the length of the NFOV observation interval. If the point corresponding the

random number lies within a spacing then the distance between the point and the cloud

to its left is taken as a sample of the "cd" type spacing. This process was repeated until

we obtained 200 samples or the iteration number exceeds 5000. The results are used as the sample space to estimate the parameters of the various assumed distributions.

Following the conventions in Chapter 3, we denote μ as the parameter of the exponential and the power law distributions for the cloud spacing, and ν for the cloud size. For the Weibull distribution, a, b are used for both cloud spacing and size. Figures 5.18 - 5.21 show the maximum likelihood estimates of the various distribution parameters for the cloud size distributions (Fig. 5.18), the cloud spacing distributions of the "sd" type (Fig. 5.19), the cloud spacing distributions of the "cd" type (Fig. 5.20), and the cloud spacing distributions of the "xd" type (Fig. 5.21). Also shown in the figures are 95% confidence intervals.

From the figures, we notice that some cases (case #: 7, 8, 9, 27, 28, 29, 34, 37, 42, 53, 70, 92) tend to generate "outlier" estimates or "abnormal" (too wide or zero wide) confidence intervals. Except cases 8 and 9, all of them are due to the very low cloud amount (< 0.1). The low cloud amount makes it difficult for the surface instruments to capture enough cloud samples to infer reliable values for the parameters. Cases 8 and 9 are sampled on the same day when the wind speed is only 1 m/s, which is the minimum among all cases. Remember, we rely on advection of the clouds with wind to infer cloud size and spacing. A low wind speed means few cloud samples can be obtained during a finite period. Like the low cloud amount, this will also lead to low-quality estimates.

Table 5.3 lists the means and ranges for the various parameters (μ, ν, a and b). The exponential parameter (μ for cloud spacing and ν for cloud size) is the inverse of the mean of population. Thus, the mean cloud size for our cases is about 700 m. Please

note that due to the positive skewness of the cloud size distribution, the most frequently

occurred cloud size will be smaller than the value estimated in preceding section. The

mean spacing between two adjacent cloud centers ("cd"), cloud edges ("sd") and a

random point to a cloud ("xd") are estimated as 2500 m, 1100 m and 1400 m,

respectively.

Table 5.3 Means and ranges of the estimated distribution parameters for the various combinations of the cloud size or spacing for the three distributions**.**

	Exponential		Power law		Weibull			
	$\overline{\mu}$ or $\overline{\nu}$ (x 10^{-3}) (1/m)	Range	$\overline{\mu}$ or $\overline{\nu}$ (pure No.)	Range	$\overline{a}$ (x 10^{-3}) (1/m^b)	Range	$\overline{b}$	Range (pure No.)
Spacing, "sd"	0.9	0.06 – 3.8	1.5	1.3 – 3.4	3.5	0 – 17	1.0	0.5 – 4.4
Spacing, "xd"	0.7	0.07 – 3.0			1.6	0 – 12	1.0	0.7 – 1.5
Spacing, "cd"	0.4	0.06 – 0.8	1.8	1.3 – 5.2	0.2	0 – 3	1.5	0.7 – 8.1
Size	1.4	0.3 – 5.2	1.6	1.3 – 3.7	1.4	0 – 12	1.2	0.6 – 4.9

The Weibull distribution is a generalization of the exponential distribution.

When b = 1, a Weibull distribution reduce to an exponential distribution. As seen from

Figs. 5.18 – 5.21, the values of b is close to 1 for the cloud size and spacings of the "sd"

and "xd" types. This indicates that the three distributions do not depart much from the

exponential distribution.

The power law slope of the cloud size distribution has drawn a lot attention in

recent decades, because it relates to the fractal property of the clouds (Lovejoy 1982;

Cahalan and Joseph 1989; Sengupta et al. 1990; Joseph and Cahalan 1990). Cahalan

and Joseph (1989) concluded that the cumulus cloud size distribution is best represented

by a double power law distribution. For fair weather cumulus the break point is around 500 m. With the cloud base diameters less than 500 m their estimate of the power law slope $\nu = 0.6$, and for cloud diameters larger than 500 m, $\nu = 2.3$. In this study, we did not break the cloud sizes into two groups. The mean of our estimates of ν is 1.6, which is in between the above results. Our value also agrees with the results from Sengupta et al. (1990). They found the power law slopes for small cumulus are ranging from $\nu = 1.4$ to $\nu = 2.35$. It should be mentioned that the results in this study are based on chord lengths obtained in vertical cross sections of the cloud fields, provided the frozen turbulence assumption is valid. They are different from the effective cloud base diameters used by the aforementioned researchers, although the two quantities may closely relate to each other. Here the effective cloud base diameter is the diameter of a circle that has the same area as the cloud base.

In the derivation of the $p(\theta)$ for the "1D_sd_Power_Power_SemiEllipse" and "1D_sd_Power_Power_IsoscelesTrapezoid", we have shown that the models require $\mu > 2$. (refer to Chapter 3). From Fig. 5.20 we find that for most of the cases, $\mu < 2$. This means that, for this model, our assumption that the cloud spacing can range from s_{min} to infinity is inappropriate. If we define the cloud spacing as the "sd" type and want to model its distribution with the power law distribution, we have to assume the spacing has finite lower and upper limits, i.e., $s_{min} \leq s \leq s_{max}$. This was not done in the present study. Hence the above two models are not used in the comparisons presented in the next section.

5.5 Comparison of the model PCLOS's with the observations

Knowing the parameters listed in Table 5.1, we can calculate the PCLOS using the models (PCLOS$_{model}$) and compare them with the PCLOS measured from the TSI (PCLOS$_{TSI}$). Figures 5.22(a, b) and 5.23(a, b) show comparisons of observations with Group-1 and Group-2 model calculations, respectively. In panels (a) of Fig. 5.22 and Fig. 5.23, PCLOS$_{model}$/(1-N) is compared with PCLOS$_{TSI}$/(1-N) (denoted as $\overline{\text{CPCLOS}}$ in the following). As mentioned in section 5.1, $1 - \text{PCLOS}(\theta)/(1-N)$ gives the conditional probability of seeing a cloud side in clear regions of the sky. Panels (b) of Fig. 5.22 and Fig. 5.23 show the differences between the PCLOS$_{model}$ and PCLOS$_{TSI}$ (denoted as $\overline{\Delta\text{PCLOS}}$ in the following). All curves in the figures are averages over 38 cases (these 38 cases are the non- streak cases whose cloud thicknesses were confirmed with the relative humidity data):

$$\overline{\text{CPCLOS}(\theta)} = \frac{\displaystyle\sum_{all\ cases} \text{PCLOS}(\theta, case) \Big/ (1 - N(case))}{No.\ of\ Cases} \qquad \text{for panels (a), or}$$

$$\overline{\Delta\text{PCLOS}(\theta)} = \frac{\displaystyle\sum_{all\ cases} \text{PCLOS}_{model}(\theta, case) - \text{PCLOS}_{TSI}(\theta, case)}{No.\ of\ Cases} \qquad \text{for panels (b).}$$

The various model calculations were performed using the values of the parameters N, β, μ, ν, a, b (refer to Table 5.1 for definitions of the parameters) inferred from the observations using the techniques discussed in the preceding sections. The minimum cloud spacing and cloud size required by the power low distributions are set

to 50 m. The Shift Regular-Cuboidal model has a parameter *f* that is the shift distance of a row with respect to its adjacent rows (see Table 5.1). Its value is set to 0.2/*N*, which is the value used by Naber and Weinman (1984).

The models that assume the cloud shape to be truncated-cones or isosceles-trapezoids require, η, the inclination angle as an additional parameter. As η varies from 0 to η_{max}, the cloud shape changes from right-cylinders or rectangles to right-cones or isosceles triangles. η_{max} is the maximum value that an inclination angle may assume. Keeping the aspect ratio as a constant, the maximum η occurs when the top length of an isosceles trapezoid or the top diameter of a truncated cone equals zero. Thus

$\eta_{max} = \tan^{-1}(\frac{D}{2H}) = \tan^{-1}(\frac{1}{2\beta})$. For example, for the fair weather cumulus over the

ARM CART site, the mean aspect ratio is 0.65 (see section 5.3), which translates to $\eta_{max} = 38^{\circ}$.

At present, there is no information available for η from the ARM observations, except η_{max}, which can be inferred from the cloud aspect ratio as mentioned above. In this study, η was specified using the following considerations. To facilitate the description, the "2D_Poisson_SemiEllipsoid" and "2D_Poisson_TruncatedCone" models are used as examples. The two models differ only in their assumptions about the cloud shape. The latter has one additional adjustable parameter, the inclination angle. Giving an arbitrary value to η will induce additional uncertainty in the comparison of the two models. To minimize the uncertainty, we set η to the value at which the two models have the least average difference in the predicted PCLOS over the selected 38 cases. In other words, we fix the truncated-cone model to have the same or close

performance as the semi-ellipsoid model in this comparison. But keep in mind that the truncated-cone model has one more parameter that can be adjusted to fit the more general conditions.

There are six models that require a value for η. Except for the Han model, all η values are determined using the above considerations. The Han model does not have a counterpart of a round-top cloud shape. Its value of η is set to be the average of the other values listed in Table 5.4. The values listed in Table 5.4 are relative factors that range from 0 to 1, with 0 corresponding to $\eta = 0^\circ$ and 1 to $\eta = \eta_{max}$. For example, when $\eta = 0.53\eta_{max}$, the "2D_Poisson_TruncatedCone" model is roughly equivalent to the "2D_Poisson_SemiEllipse" model for the cases we selected over the ARM CART site.

Table 5.4 Values for the inclination angle, η.

Model	Value for η (x η_{max})
1D_Poisson_IsoscelesTrapizoid	0.74
2D_Poisson_TruncatedCone	0.53
1D_xd_Exp_Exp_IsoscelesTrapezoid	0.68
1D_sd_Exp_Exp_IsoscelesTrapezoid	0.68
1D_xd_Weib_Power_IsoscelesTrapezoid	0.47
1D_cd_Power_Power_VariableShape (Han)	0.62

In figures 5.22 and 5.23, all model PCLOSs, except the Han model, tend to decrease more rapidly for $\theta < 50^\circ$ and more slowly for $\theta > 60^\circ$. Both groups of models tend to underestimate the PCLOS in the middle range of the zenith angles ($30^\circ < \theta < 70^\circ$), although the Group-2 models give better results than the Group-1

models. For all Group-2 models, except the "2D_Poisson_RightCylinder" model and the "2D_ShiftRegular_Cuboidoal" model, the average $PCLOS_{model}/(1-N)$ agrees with the TSI observations within about ±0.1 of the cloud fraction unit (panel (a) in the Fig. 5.23).

The average $(PCLOS_{model}-PCLOS_{TSI})$ curves disperse with increasing zenith angle (Fig. 5.22(b) and Fig. 5.23(b)). The fact that all the curves start from zero at 0° is simply because we have set the parameter $N = N_{TSI}$, thereby forcing the models to have zero difference with the TSI observations at $\theta = 0$. Assuming the TSI inferences of the PCLOS are accurate, the dispersion of the curves at larger zenith angles reflects the different performance of the various models, which depends on the validity of the model assumptions and the accuracy of the various model parameters, including N. As seen, for most of the zenith angles the dispersion is less than 0.15 (in units of cloud fraction).

Also noticed from the figures is the big difference between the "2D_Poisson_RightCylinder" model and the "2D_Poisson_TruncatedCone" model, although the former is just a special case of the latter. The only difference between these two models is the different cloud shapes. This indicates that the cloud shape (inclination angle in this case) may be an important factor when modeling the PCLOS.

Figure 5.24 shows the standard deviation of the difference between the models and the TSI observations as a function of zenith angle for the different models. For most models, the maximum standard deviation of $(PCLOS_{model}-PCLOS_{TSI})$ is less than 0.2 (in cloud fraction units), except the "1D_cd_Power_Power_VariableShape (Han)" and

"2D_ShiftRegular_Cuboidal" models. Among the models, the

"2D_Poisson_Hemisphere" model tends to have the smallest bias and variance.

To further compare the performance of the various PCLOS models, we define a

quantity,

$$CSE = 2\int_0^1 \left[1 - N - PCLOS(\mu)\right]\mu \, d\mu$$

where $\mu = \cos(\theta)$, and the $PCLOS(\mu)$ is the probability of a clear line of sight at angle θ.

The CSE denotes the Cloud Side Effect, which represents the contribution of the cloud

sides to the effective cloud fraction N_e. In fact, $CSE = N_e - N$ for isothermal black

clouds. The factor CSE can be viewed as a summary quantity that provides us an overall

measure of the cloud side effect on the cloud coverage. Figure 5.25 shows summary

statistics of the model predictions of CSE and those inferred from the TSI observations.

In the figure, the bottom and the top of the box give the 25th and 75th percentiles of the

sample. The line in the middle of the box is the sample median. The plus signs are

outliers in the data (i.e, values that are more than 1.5 times the box length away from

the top or bottom of the box). The last column in the figure is CSE computed from the

TSI observations. CSE has units of cloud fraction.

As we mentioned before, CSE denotes the contribution from cloud sides to the

effective cloud fraction. This part of the effective cloud fraction increases the radiation

fluxes from the cloud field relative to flat plates. The y-axis on the right-hand side of the

figure gives the estimated value of the increase of downward flux at the surface due to

the cloud side effect. Since $F = F_{clr} + N_e(F_{cld} - F_{clr})$ and $N_e = N + CSE$,

$\delta F = (F_{cld} - F_{clr}) \cdot CSE$, where F_{clr} and F_{cld} denote the fluxes under clear and overcast

conditions, respectively. The F_{clr} and F_{cld} are calculated using MDTERP (Ellingson and Gille 1978; Takara and Ellingson 2000). The McClatchey midlatitude summer profile is used in the calculation and the cloud base height is assumed to be 1.5 km. The TSI column (the last column in the figure) shows that, for those the fair weather cumulus over the ARM CART site, the mean flux departure at the surface due to the cloud side effect is about 3.7 W/m^2. Table 5.5 lists the mean and standard deviation of the *CSE* values estimated from the various models and the one from the TSI.

Table 5.5 The mean and standard deviation of the *CSE* values estimated from the various models and the one from the TSI. Where STD. denotes standard deviation.

Model or TSI	*CSE*		δF (W/m^2)	
	Mean	STD.	Mean	STD.
1D_sd_Exp_Expl_IsoscelesTrapezoid	0.111	0.094	6.9	5.9
1D_sd_Exp_Exp_SemiEllipse	0.111	0.093	6.9	5.8
1D_xd_Exp_Exp_IsoscelesTrapezoid	0.096	0.089	6.0	5.6
1D_xd_Exp_Exp_SemiEllipse	0.095	0.087	5.9	5.5
1D_xd_Weib_Power_IsoscelesTrapezoid	0.102	0.061	6.3	3.8
1D_xd_Weib_Power_SemiEllipse	0.094	0.059	5.9	3.7
1D_cd_Power_Power_VariableShape (Han)	0.068	0.148	4.2	9.3
1D_Poisson_IsoscelesTrapezoid	0.092	0.092	5.7	5.7
1D_Poisson_SemiEllipse	0.093	0.090	5.8	5.6
2D_Poisson_TruncatedCone	0.092	0.087	5.7	5.4
2D_Poisson_SemiEllipsoid	0.093	0.090	5.8	5.6
2D_Poisson_Hemisphere	0.057	0.029	3.6	1.8
2D_Poisson-Ellipsoid	0.074	0.082	4.6	5.1
2D_Poisson-RightCylinder	0.156	0.112	9.8	7.0
2D_ShiftedRegular _Cuboidal	0.20	0.182	12.9	11.4
TSI observation	0.059	0.040	3.7	2.5

Figure 5.26 shows box plots of the differences between the *CSE* predicted by the models and that from the TSI. Corresponding mean and standard deviation of the differences are listed in Table 5.6. All Group-1 models tend to have positive biases. The "2D_Poisson_Hemisphere" model is a special case of the "2D_Poisson_SemiEllipsoid" model, as the hemisphere model sets the aspect ratio to be a constant, while the semi-ellipsoid model uses the observed aspect ratio. Interestingly, the former gives a better result than the latter. The range of the differences for the hemisphere model is less than that for the semi-ellipsoid model. This might indicate that our estimates of the aspect ratio are slightly positively biased, at least for some of the cases.

Once again, we see a difference between the "2D_Poisson_TruncatedCone" model and the "2D_Poisson_RightCylinder" model. The only difference between the two models is the inclination angle, but they yield quite different predictions of *CSE*. The "2D_Poisson_RightCylinder" model apparently overestimates the cloud side effect.

Among all models, the "2D_Poisson-Hemisphere" generates the best results. However, because the "2D_Poisson-TruncatedCone" model has been fixed to its semi-ellipsoid counterpart and the semi-ellipsoid model is a general case of the hemisphere model, we expect that given appropriate values for the aspect ratio and inclination angle, the "2D_Poisson_TruncatedCone" model and the "2D_Poisson_SemiEllipsoid" model have the potential to generate the same result as the "2D_Poisson_Hemisphere" model.

Table 5.6 The means and standard deviations of the differences between the *CSE* predicted by the models (*CSE*$_{model}$) and those obtained from TSI (*CSE*$_{TSI}$). Where STD. denotes standard deviation.

Model or TSI	*CSE*$_{model}$- *CSE*$_{TSI}$		δF_{model}-δF_{TSI} (W/m^2)	
	Mean	STD.	Mean	STD.
1D_sd_Exp_Expl_IsoscelesTrapezoid	0.052	0.088	3.3	5.5
1D_sd_Exp_Exp_SemiEllipse	0.052	0.087	3.3	5.4
1D_xd_Exp_Exp_IsoscelesTrapezoid	0.037	0.085	2.3	5.3
1D_xd_Exp_Exp_SemiEllipse	0.036	0.084	2.3	5.2
1D_xd_Weib_Power_IsoscelesTrapezoid	0.041	0.067	2.6	4.2
1D_xd_Weib_Power_SemiEllipse	0.034	0.065	2.1	4.1
1D_cd_Power_Power_VariableShape (Han)	0.009	0.162	0.6	10.1
1D_Poisson_IsoscelesTrapezoid	0.033	0.082	2.1	5.1
1D_Poisson_SemiEllipse	0.034	0.080	2.1	5.0
2D_Poisson_TruncatedCone	0.033	0.077	2.1	4.8
2D_Poisson_SemiEllipsoid	0.034	0.080	2.1	5.0
2D_Poisson_Hemisphere	-0.002	0.042	-0.1	2.7
2D_Poisson-Ellipsoid	0.016	0.073	1.0	4.5
2D_Poisson-RightCylinder	0.098	0.098	6.1	6.2
2D_ShiftedRegular _Cuboidal	0.141	0.165	8.8	10.3

5.6 Chapter Summary

The parameters required by the PCLOS models are the absolute cloud fraction N, the aspect ratio β, the parameters characterizing the cloud spacing and size distributions μ, ν, a, b, and the cloud inclination angle η. In this chapter, methods have been developed to infer these parameters from the ARM cloud observations (not including the inclination angle). The absolute cloud fraction is estimated as the frequency of the central portion of the TSI image being covered by clouds. Among all 93 cases, most are fair weather cumulus fields and have $N < 0.7$. The aspect ratio is theoretically defined for every cloud, but we cannot obtain such detailed observations of the clouds in practice. Thus, in this study, β is estimated for every case as the ratio of the average cloud thickness to the median cloud horizontal size. The median is used instead of the mean because the cloud horizontal size is highly asymmetrically distributed. Among all 93 cases, more than 80% have $\beta < 1$, ($\beta = H/D$). The mean value equals 0.65 and the median is 0.43.

Three theoretical distributions, the exponential, the Weibull and the power law distributions are used to model the cloud spacing and size distributions. The distribution parameters for the three distributions are inferred for every case from the time series of the NFOV observations. Several models need the inclination angle η as a model parameter. Without observational information about η, these models are set to have the same performance as their round-top-shape counterparts by specifying a value for η so that the pair (the η-adjustable model and its round-top-shape counterpart) has minimum average difference in the predicted PCLOSs.

We also developed a method to estimate the PCLOS using time series of images from the TSI. Based on this TSI observed PCLOS, the cloud side effect on the downward longwave radiation flux is estimated. For the fair weather cumulus clouds over the ARM CART site, the mean flux departure at the surface due to the cloud side effect is about 3.7 W/m^2 (assuming the cloud height is 1.5 km). The standard deviation among various cases is about 2.5 W/m^2.

Model calculated PCLOS values were compared with those obtained from the TSI. Based on the obtained parameters, the models that assume the clouds are Poisson distributed give better result than those that specify cloud distribution by explicitly specifying the cloud spacing and size distributions. Most PCLOS$_{model}$'s agree with the observations within ±0.2 (Fig. 5.24). All models, especially those models that assume the cloud shape as right cylinder or cuboidal and 1D models tend to underestimate the PCLOS (or overestimate the cloud side effect). This may partly due to the incorrect information about the cloud aspect ratio and inclination angle. For example, the cloud base diameter was assumed to be the measured chord length. This may result in an underestimate of the cloud base diameter and hence an overestimate of the aspect ratio. For a circular cloud base, the real diameter may be 1.5 times longer than the average chord length (Mathai 1999). However, due to the complicated nature of the cloud base shape, there is no exact relationship between the diameter and chord length available. Hence, there is not a good way to correct this bias at present

Among the models listed in Table 5.1, the "2D_Poisson_Hemisphere" model generates the best average results for the cases selected in the present study. The "2D_Poisson_Hemisphere" model is a special case of the "2D_Poisson_SemiEllipsoid"

model when $\beta = 0.5$. This may indicate that the aspect ratio of the fair weather cumulus cloud over the ARM CART site is most probably around 0.5. However, since the hemisphere model assumes a constant aspect ratio, it may not work for other type of clouds or clouds at different geographical locations. The "2D_Poisson_Ellipsoid" model and the "2D_Poisson_TruncatedCone" model are generalizations of the hemisphere model. They may be used in broader conditions.

The cloud aspect ratio and the inclination angle can largely affect the modeled PCLOS. The differences due to the three theoretical distributions used to model the cloud spatial and size distributions are no greater than the differences resulting from the different cloud inclination angles.

Finally, it should be noted that since the fair weather cumulus clouds over the SGP region are relatively small, the cloud side effect is relatively weak. For these small clouds, the goodness of the model results is largely limited by the accuracy of the estimates of the model parameters. As illustrated in Fig. 5.26 and Table 5.6, although some models achieve zero bias, their dispersion is of the same order of magnitude of the *CSE* value itself. We expect that this situation may improve when dealing with cumulus clouds over the ARM Tropical Western Pacific (TWP) site.

Chapter 6

Summary, Conclusion, Discussion and Future work

The Probability of Clear Line Of Sight (PCLOS) is a basic property of 3D cloud fields and is important to the understanding and parameterization of longwave radiative transfer in climate models. One way to incorporate the 3D geometrical effects in the parameterization is through the use of an effective cloud fraction, for which a major component is the PCLOS of the cloud field. The PCLOS also plays an important role in accounting for longwave 3D effects caused by variations of horizontal optical depth and the vertical temperature gradient in heterogeneous cloud fields. Aimed at improving the understanding and parameterization of longwave radiative transfer under cloudy conditions in climate models, this study addressed the formulation, measurement and testing of the PCLOS.

(1) Formulation of the PCLOS

Theoretical formulation of PCLOS models was addressed in a systematic way in the study. Several extensions and improvements were made. Three approaches for modeling the PCLOS were discussed in Chapter 3. They are: (1) computing the ratio of the projected clear area to the total domain area on a horizontal plane; (2) tracing a line of sight through a cloud field; and (3) modeling the PCLOS as the probability of occurrence of a pair of clouds having spacing larger than a threshold value (Han's method). In all, 17 models based on different formulation approaches and different

assumptions about the cloud shape, spatial and size distributions were discussed

(Table 6.1).

Table 6.1. The PCLOS models used in this study. Among them 9 are new and the others are revisions or extensions of the previous studies. Also shown in the table are the equation numbers that appear in the text.

1D_sd_Exp_Exp_SemiEllipse	New	Eq. (3.16)
1D_sd_Exp_Exp_IsoscelesTrapezoid	New	Eq. (3.16)
1D_sd_Power_Power_SemiEllipse	New	Eq. (3.14)
1D_sd_Power_Power_IsoscelesTrapezoid	Revision of the Han and Ellingson (1999) model	Eq. (3.11)
1D_xd_Exp_Exp_SemiEllipse	New	Eq. (3.36)
1D_xd_Exp_Exp_IsosecelesTrapezoid	New	Eq. (3.36)
1D_xd_Weib_Power_SemiEllipse	New	Eq. (3.34)
1D_xd_Weib_Power_IsoscelesTrpezoid	Revision of the Han and Ellingson (1999) model	Eq. (3.34)
1D_cd_Power_Power_VariableShape(Han)	Han and Ellingson (1999)	Eq. (3.38)
1D_Poisson_SemiEllipse	Extension of the Kauth and Penquite (1967) model	Eq. (3.23)
1D_Poisson_IsoscelesTrpezoid	New	Eq. (3.22)
2D_Poisson_SemiEllisoid	Kauth and Penquite (1967)	Eq. (3.29)
2D_Poisson_TruncatedCone	New	Eq. (3.24)
2D_Poisson_Ellipsoid	Kauth and Penquite (1967)	Eq. (3.28)
2D_Poisson_Hemisphere	Kauth and Penquite (1967)	Eq. (3.29)
2D_Poisson_RightCylinder	New	Eq. (3.27)
2D_ShiftRegular_Cuboidal	Naber and Weinman (1984)	Eq. (3.30)

(2) Sampling Strategy

In order to determine an objective sampling strategy and place uncertainty limits on the inference of the PCLOS and other cloud field parameters, an evaluation method was developed and tested with CRM/LES model data. The method is an extension of the one used in geostatistics (Cochran 1977; Matern 1986), stereology (Stoyan et al.

1987) and meteorology (Kagan 1997). It not only applies to the measurement of the cloud parameters at the ARM site, but also has general significance for evaluating the sampling error when one wants to extend local measurements to a larger domain.

The ARM cloud observations produce time series of measurements of the directly overhead cloud field. Area-averaged quantities are inferred from time average ones from a series of data by assuming the frozen turbulence approximation. Under the assumption, a time series of data can be interpreted as a spatial series of observations taken along a single sampling line (a transect) in the cloud field. Depending on the sampling rate, the observations may not be independent of each other. To evaluate the spatial representativeness of the measurement from the line of observations, a random field approach is taken in this study. The approach assumes the cloud field is a homogeneous and isotropic random field. Given the covariance function (= variance × correlation function), the sampling error of the area-averaged quantities can be estimated.

The approach was applied to the measurement of the cloud fraction. A correlation function with a negative exponential form was assumed for the cloud fraction field. The investigation indicates that the sampling error is dependent on several parameters including the covariance function of the cloud fraction field, size of the target area, length of the sampling line, sampling rate of the observations and the position of the sampling line. The e-folding parameter, ρ_0, of the correlation function is an important quantity when evaluating the sampling strategy, as it is a measure of the correlation scale of the random field. Using the data from the NFOV, the average ρ_0 for the fair weather cumulus cloud fields over the ARM SGP site is estimated as 1267 m.

112

For a large target area (the dimensions of the area being larger than $30\rho_0$) with a given ρ_0, the sampling error decreases monotonically with increasing length of the sampling line and sampling rate. The accuracy improvement resulting from increasing the sampling rate is limited because the observations taken within the distance of the correlation scale are not independent. Given a sampling line of $50\rho_0$ in the middle of the target area, one may expect a sampling error of about 30%, assuming a cloud fraction of 0.4.

Please note that, when determining the averaging time, considerations should also be given to such factors as wind speed, cloud development and life span of the cloud field, because these factors affect the validity of the frozen turbulence approximation. The approximation requires statistical properties of the cloud field not to change as the cloud field advects over the observation site.

(3) Measurement of the cloud parameters and test of the PCLOS models

Part of this study was directed at developing a set of automated techniques for estimating PCLOS from the ARM sky imagers and for a variety of important cloud field properties from ARM observational data or previously established cloud products. As such, these techniques may be employed on more extensive cloud data sets to further enhance our understanding the longwave 3D effects for a wider range of cloudiness conditions. The data from these techniques, combined with the sampling strategy outlined above, allow a major extension of previous PCLOS studies, namely the testing of PCLOS models with data with realistic confidence limits.

93 cases of single layer broken cloud fields at the ARM SGP CART site during the period from July 2000 though October 2001 were selected for inferring various cloud field parameters and testing PCLOS models, but only 38 non-streak cases whose cloud thickness has been confirmed with the relative humidity data were used in the comparisons of the modeled with the observed PCLOS. The absolute cloud fraction, cloud thickness, cloud size and spacing distributions were extracted from the TSI, NFOV, RWP915, MMCR, MPL, RL, BBSS and the ARSCL data using the techniques mentioned above. Time series of total sky images were used to infer the PCLOS and its uncertainty for the individual cases.

The absolute cloud fraction of the selected cases ranges from 0.1 to 0.9 with the mode around 0.4. The cloud thickness ranges from 100 m to 3000 m, but most of cases have the thicknesses less than 500 m. For each case, the cloud thickness was taken to be the mean value for a whole field. Thus there is a variation in the thickness for each case. The most frequent size of the variation is about a half of the mean cloud thickness. The aspect ratio ranges from 0.1 to 4 with most less than 1. For most of the cases, the median cloud horizontal size and spacing are less than 1000 m and 2000 m, respectively. The cloud spacing tends to have greater case-to-case variation than the cloud horizontal size.

In all, 15 PCLOS models were compared with the observations. Based on the parameters obtained, most models yield PCLOS values that agree with the observations within ±0.2 for the zenith angle range from 10° to 80°. All models tend to slightly underestimate the PCLOS within the 30° to 70° zenith angle range, but the models that assume the clouds are Poisson distributed give better results than those that explicitly

114

specify the cloud spacing and size distributions.

Cloud aspect ratio and inclination angle have large impacts on the modeled PCLOS, but the inclination angle is not an observable quantity. Among the models, the "2D_Poisson_Hemisphere" model has the best average performance. Since the "2D_Poisson_SemiEllisoid" and the "2D_Poisson_TruncatedCone" models are generalizations of the hemisphere model, we expect that they may have at least the same performance as the hemisphere model if given accurate cloud parameters.

The geometrical effect of 3D clouds on the downward longwave radiation flux at the surface was estimated using both PCLOS model calculations and the TSI observations. Based on the observations, the mean departure from plane-parallel clouds at the surface due to the geometrical effect (CSE) of the clouds is about 3.7 ± 2.5 Wm^{-2} for a cloud height of 1.5 km. Given the obtained cloud parameters, most model estimates tend to overestimate the effect and have standard deviations of the same order as the mean values. This indicates that, confined by the uncertainties in the cloud parameters obtained to date, most models may not be able to generate reliable estimates of the geometrical effect of fair weather cumulus over the SGP site. One exception is the "2D_Poisson_Hemisphere" model, which gives reasonable estimates ($CSE = 3.6 \pm 1.8$ Wm^{-2}). It is interesting to note that the hemisphere model requires the least number of cloud parameters but generates better results than its generalizations, such as the "2D_Poisson_SemiEllipsoid" model and the "2D_Poisson_TruncatedCone" model. This is another indication that the confining factor may be the quality of the cloud parameters.

(4) Future work

All the cases we selected in this study are non-precipitating fair weather cumulus fields. The clouds are relatively small and they are members of a special category of broken cloud fields. To more thoroughly investigate the validity of the PCLOS models and study the impact of the 3D clouds on longwave radiative transfer, it will be necessary to consider more categories of broken clouds in future studies. Such studies are now possible with data from the ARM Tropical Western Pacific (TWP) site.

The airborne clutter problem at the ARM SPG site greatly limits our ability to precisely infer the cloud thickness from the MMCR data. Since the total sky imager is also planned for the TWP site where there is no clutter problem, one may expect a better data set and thus a more solid test of the PCLOS models. In addition, using the TWP data will also give us a chance to test with a new category of broken clouds – tropical fair weather cumulus.

The PCLOS models addressed in this study are all based on Euclidean geometric models of the cloud field. The clouds are modeled as geometric objects with simple shapes and distributed on a common cloud base line or plane regularly or randomly according to relatively simple distribution laws. Recently, some researchers have been modeling the cloud field using the fractal technique. The method generates, at least from the morphological perspective, more realistic cloud fields. Since the PCLOS is mainly a morphological property of the cloud field, a PCLOS model based on fractal theory may be an attractive choice for future studies.

The observations at the ARM CART site can yield empirical PCLOS functions for individual periods. This leads to the question of the sensitivity of climate studies to PCLOS models. Should we use a theoretical or an empirical PCLOS model or any such model at all? Should people place more effort into improving the PCLOS models or observations? To answer the questions one will need more information about the PCLOS and cloud field parameters in various climate regions, seasons and cloud categories. If the PCLOS has large variations at different locations and times, then one may have to put more effort on the models. Otherwise, if the PCLOS doesn't change very rapidly with location and time, or the PCLOS variations are not significant to climate model studies, then an empirical PCLOS may be good enough. Answering these questions is another possible direction for future work.

Figures
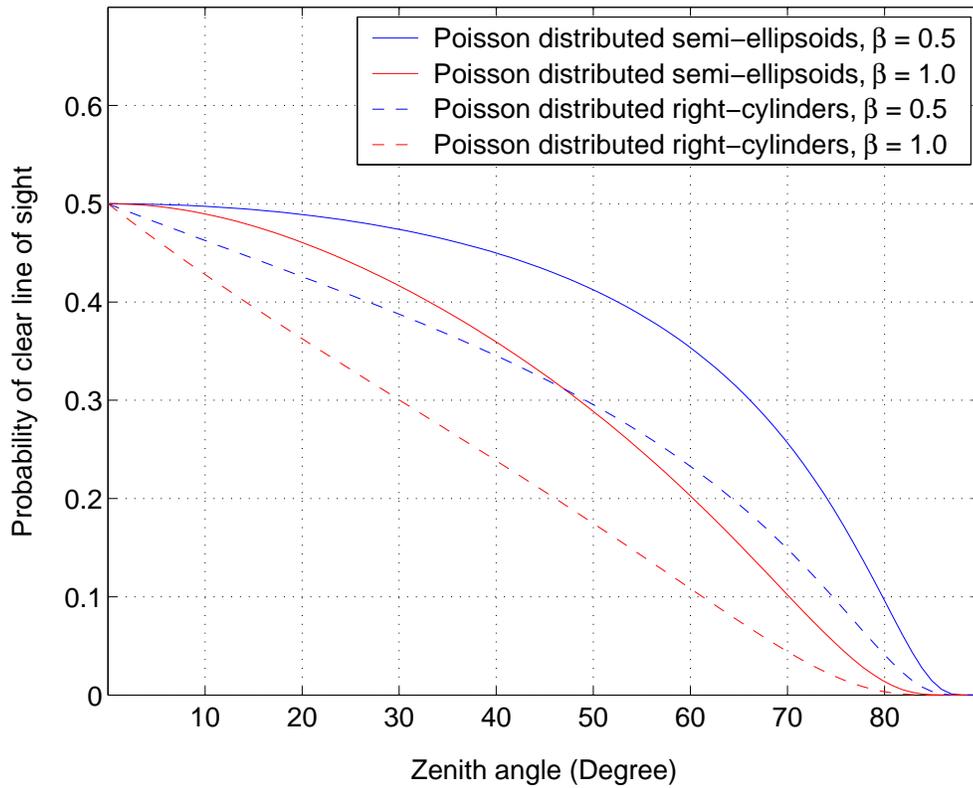
Fig. 1.1 Examples of the Probability of Clear Line Of Sight (PCLOS) for randomly distributed semi-ellipsoids and right-cylinders. Due to the cloud side effect, the PCLOS decreases with increasing zenith angle. Given the same cloud fraction and distribution, the greater the cloud vertical dimensions, the larger the cloud side effect until mutual shading occurs. At the zenith, the PCLOS = (1 - *N*), where *N* is the absolute cloud fraction. The inclination angle of the clouds has large impact on the PCLOS.

Radiation from plane parallel
clouds with homogeneous
optical depth at a level Z and

Non-isothermal cloud, cloud
temperature decreases with

Radiation from vertically extended clouds with variable optical depth at a level Z and
angle θ
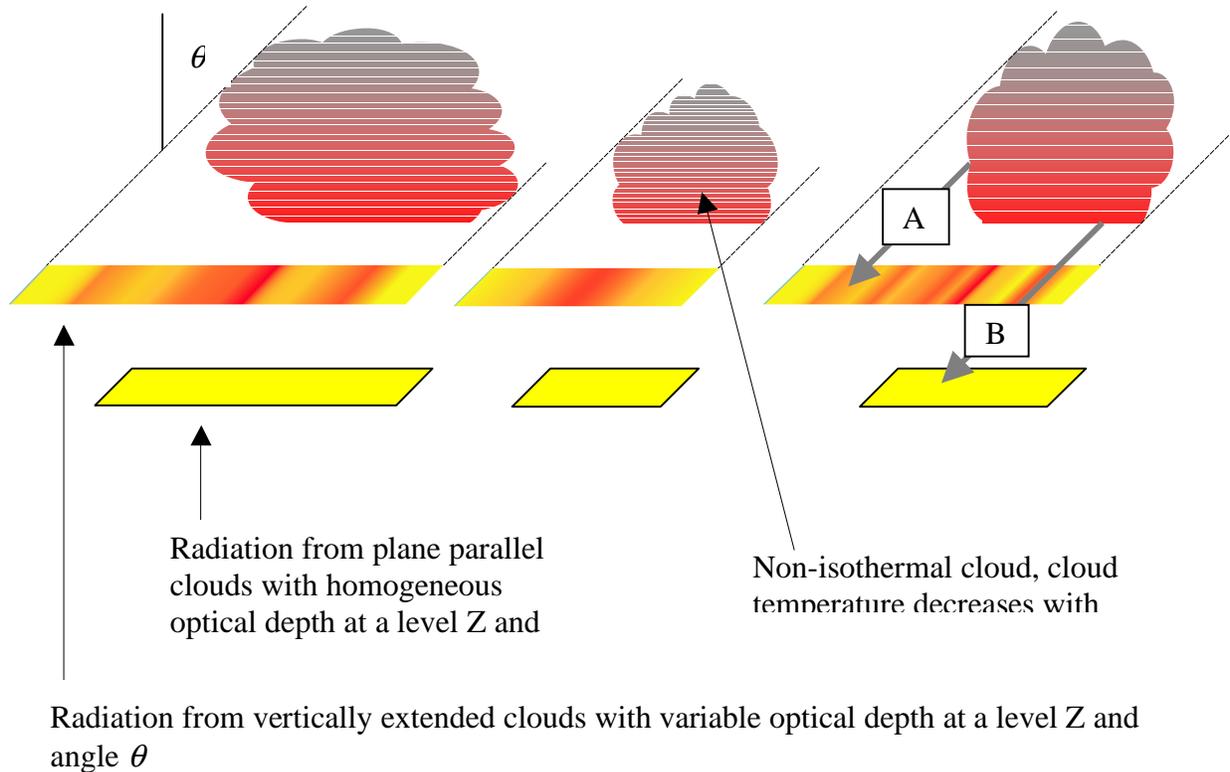
Fig. 2.1 An illustration of three aspects of 3D cloud effects.

(1) Geometric effect. When viewed at a zenith angle θ, vertically extended clouds will project greater lengths than the PPH clouds. The PPH cloud lengths were obtained by projecting the clouds vertically downward and have been displaced here to coincide with the start of the projections of the vertically extended clouds.
(2) Variable optical depth effect: Due to the 3D structure of the cloud field and variation of the optical properties within the clouds, the optical depth seen at an angle θ may vary horizontally. Because of the highly non-linear dependence of the cloud transmission or emission on the cloud optical depth, the domain-averaged radiance may be significantly different from the radiance at the average cloud optical depth.
(3) Non-isothermal cloud effect: Clouds are not isothermal. Temperature may very with height. Due to the existence of brokenness and non-opaque clouds, radiation from the cloud layer may be emitted from various heights and thus from various temperatures.

In the figure:
The pencil of beam (A): Radiance from cloud side, which is neglected by PPH approximation.
The pencil of beam (B): Radiance from PPH approximation.

$T_c(z_t, z_b, \tau(\mu), \mu)$

z_t

z_b

z
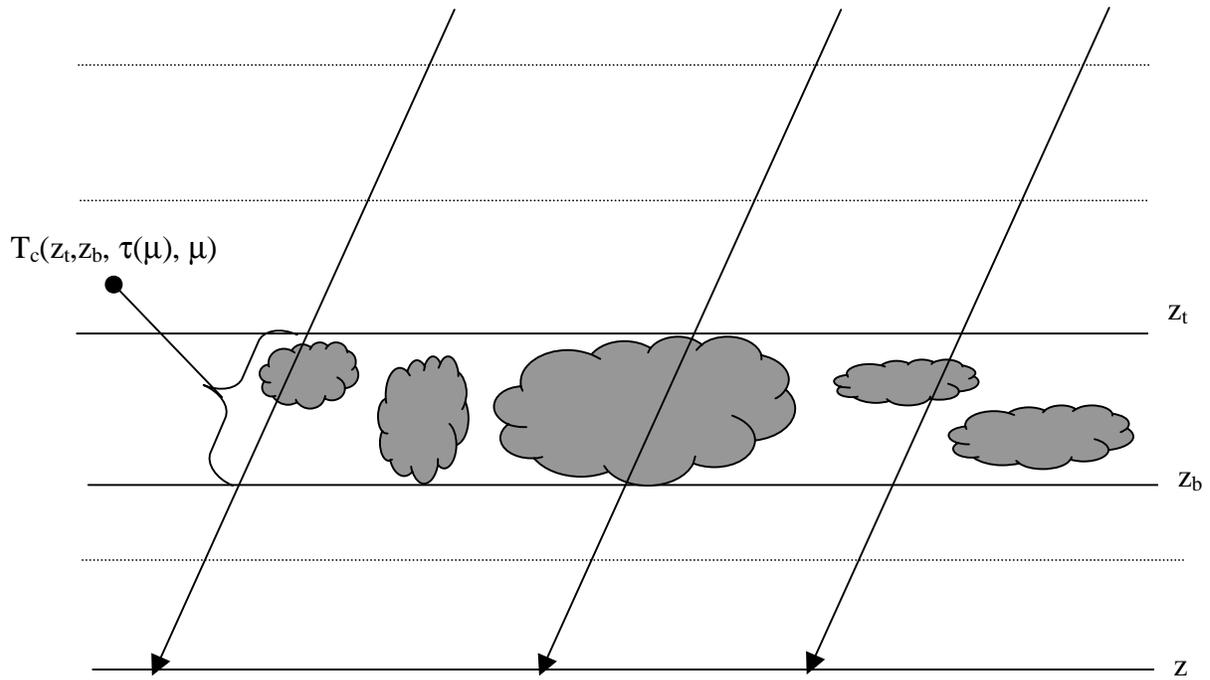
Fig. 2.2 A quasi-3D cloud field.

The atmosphere is horizontally homogeneous. All clouds properties are azimuthally averaged values. There is only one layer of clouds and all clouds are constrained in the layer between z_b and z_t, which denote the cloud base and top height, respectively. Scattering is neglected.

A single cloud element

s_c s_c s_c s_c
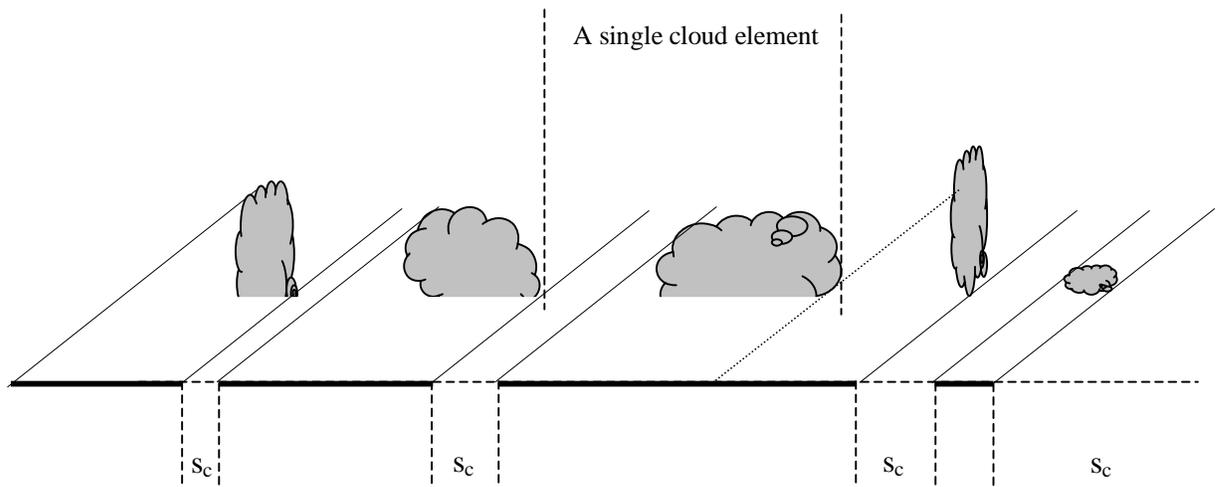
Fig.3.1 A vertical section of a hypothetical cloud field.

s_c is a clear section of the horizontal line (parallel to the line of the cloud base) that is not covered by the projection of the cloud projected at zenith angle θ. A cloud element consists of a cloud and a spacing associated with it.
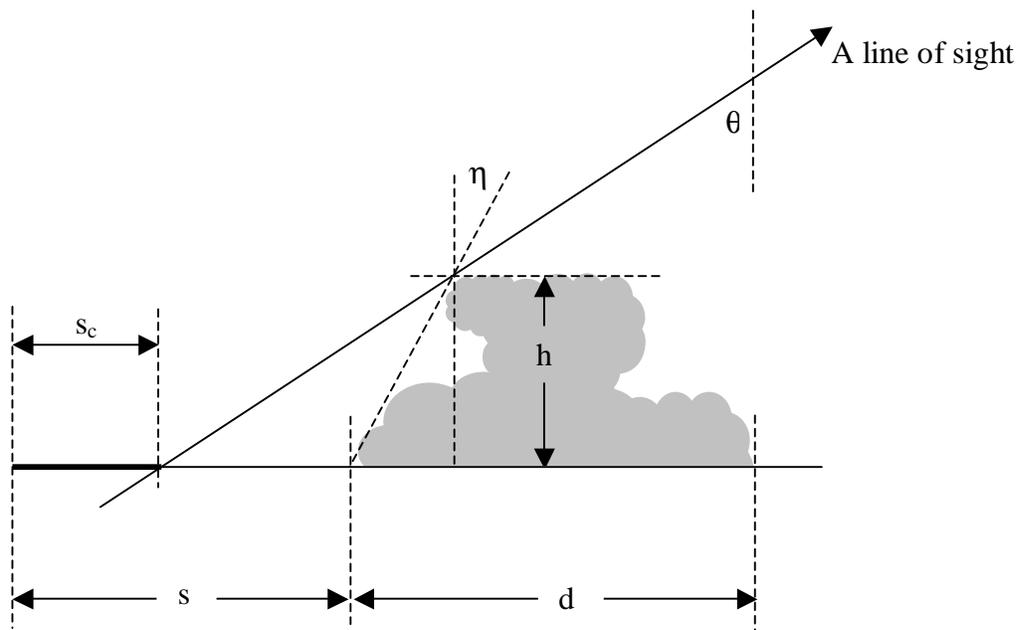
Fig.3.2 Geometrical features associated with a cloud element. In the figure, *d* is the length of the vertical projection of the cloud on the horizontal line; *s* is the spacing between two adjacent vertical projections; *h* is the cloud thickness; η is the inclination angle of the cloud side relative to the zenith.

'sd' type of spacing is defined as the distance between the two nearest edges of two adjacent clouds.

'cd' type of spacing is defined as the distance between two cloud centers of two adjacent clouds.

'xd' type of spacing is defined as the distance between an arbitrary point and its nearest cloud to the right.
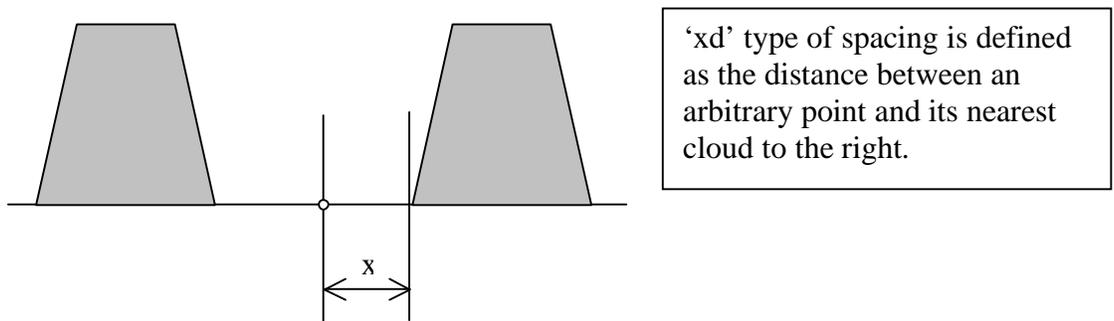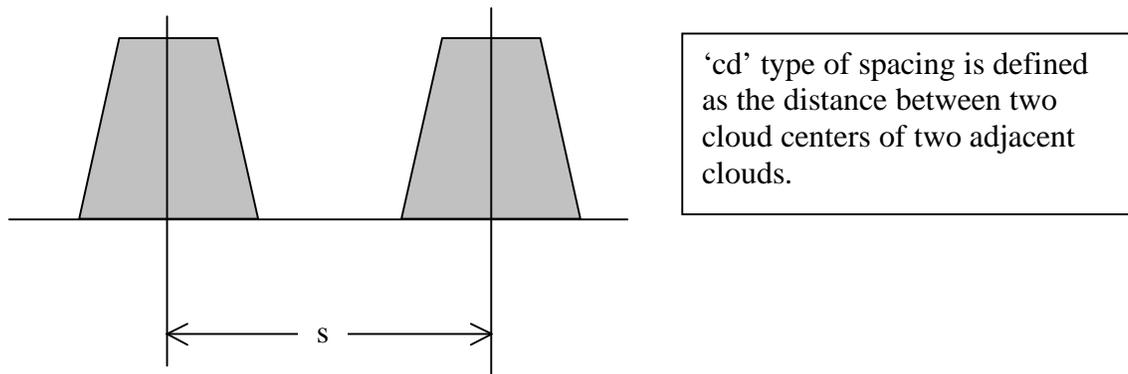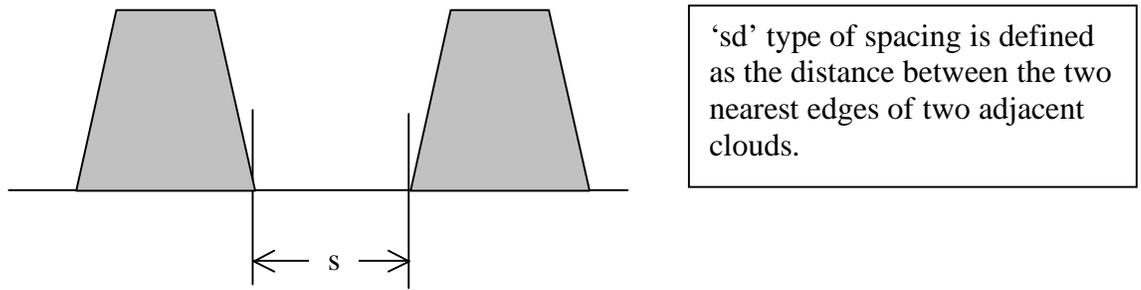
Fig.3.3 Three types of cloud spacing. Different PCLOS

models use different definitions of the cloud spacing.
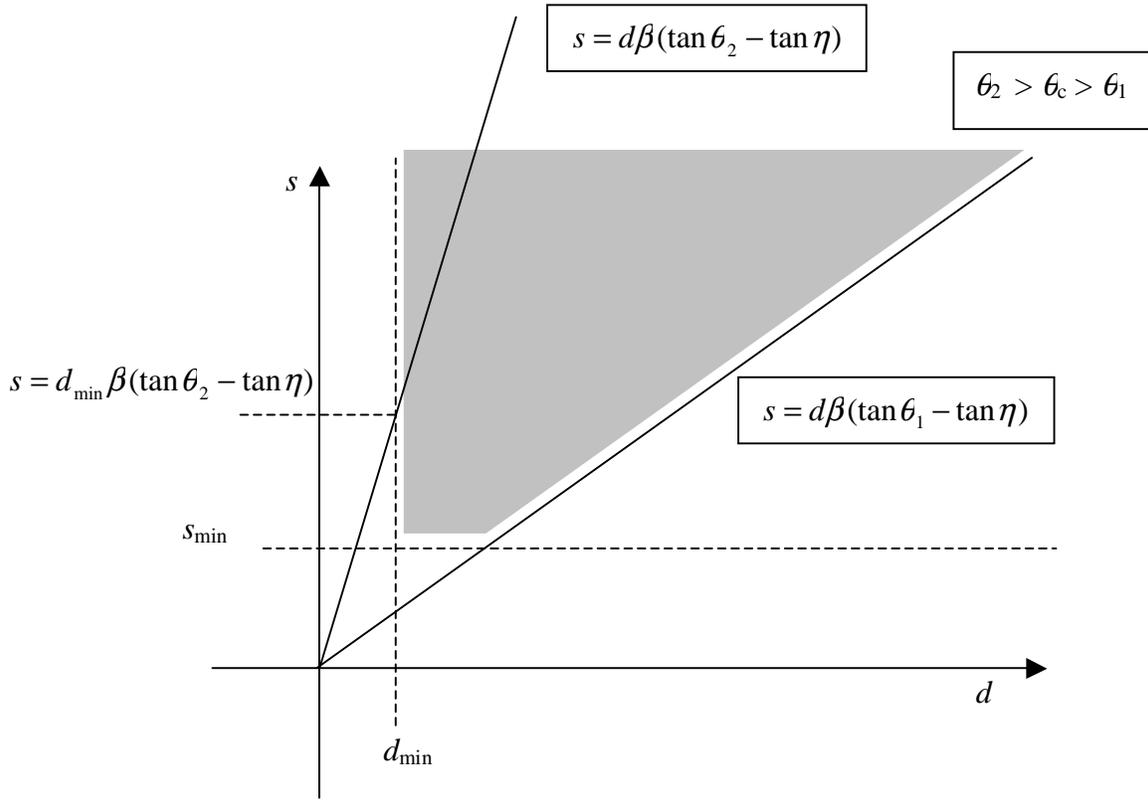
Fig.3.4 Integral domain of $\overline{s_c(\theta)}$. The valid domain is shown in the figure as the shaded area.

$$\begin{cases} d: & d_{\min} \to \dfrac{s}{\beta(\tan\theta - \tan\eta)} \\ s: & d_{\min}\beta(\tan\theta - \tan\eta) \to \infty \end{cases} \qquad \text{for } \theta > \theta_c$$

$$\begin{cases} d: & d_{\min} \to \dfrac{s}{\beta(\tan\theta - \tan\eta)} \\ s: & s_{\min} \to \infty \end{cases} \qquad \text{for } \theta < \theta_c$$

Where s denotes the cloud spacing, d denotes the cloud horizontal size, β is the aspect ratio, $d\beta = h$. The angle η is the slant angle of the isosceles trapezoid cloud.
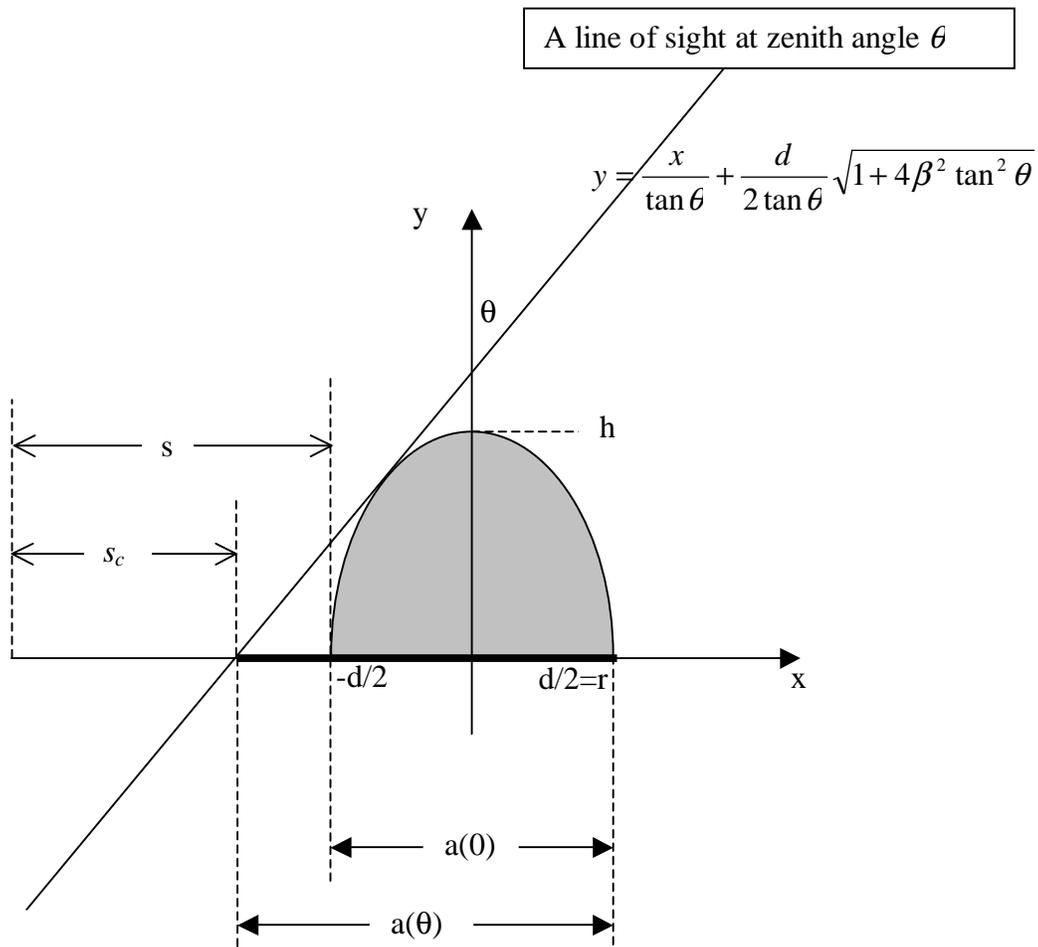
Fig.3.5 $s_c(\theta)$ for a semi-ellipse cloud. The cloud is placed in an x-y plane with the base center located at the origin of the coordinates. The cloud horizontal size is $d=a(0)$. A line of sight tangent to the cloud is also shown on the plot. By setting $x=0$ in the line equation, we can obtain $s_c(\theta)$. (refer to Eq.(3.13)).

$a(\theta) = t(\theta)$, $a(0) = t(0)$ for a single cloud (refer to Eq.(3.23)).
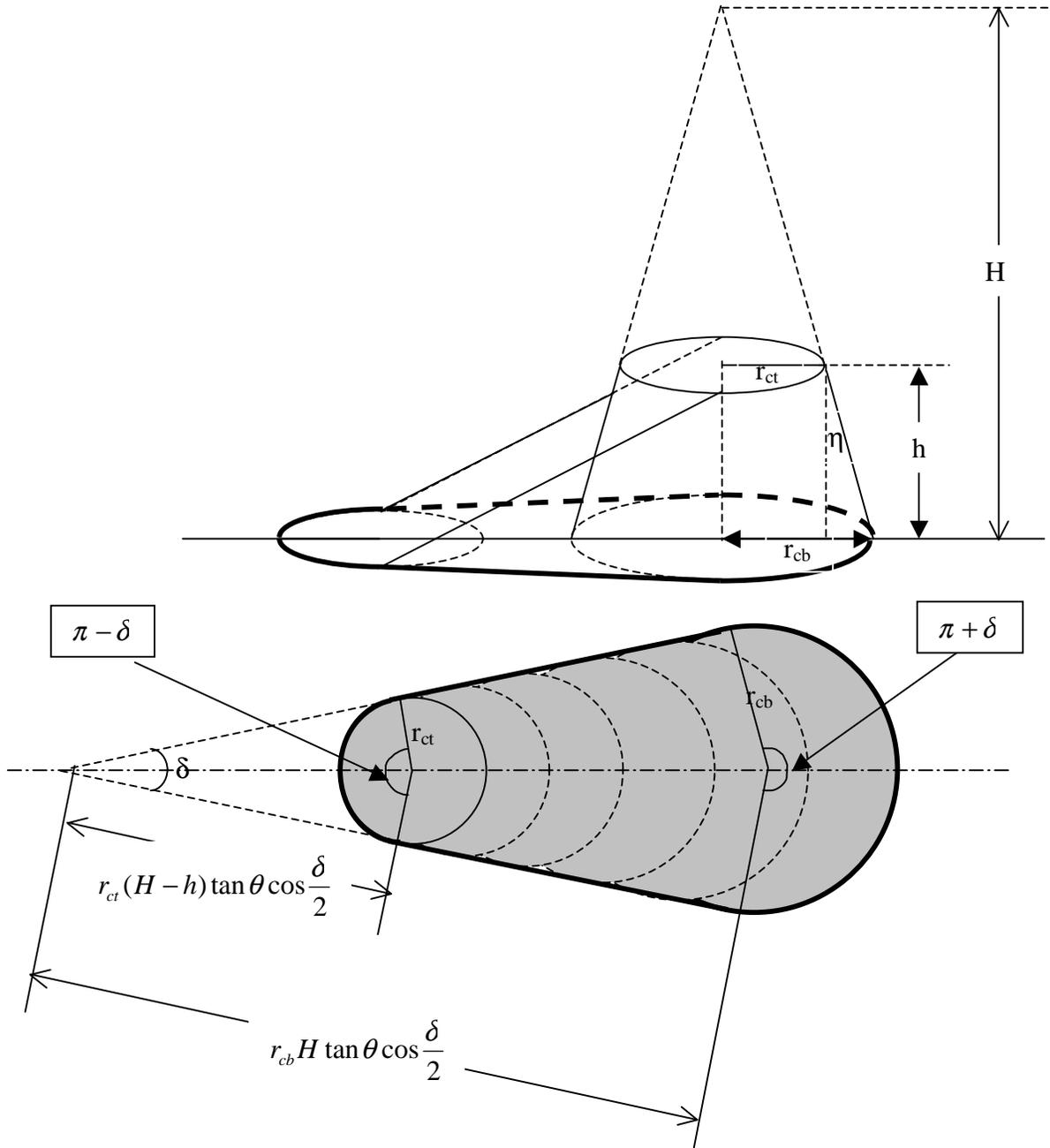
Fig.3.6. $a(\theta)$ for a truncated cone cloud. The shaded area can be seen as a set of circles aligned along a straight line, which is the projection of the central-symmetrical axis of the truncated cone. The area of the shadow is the area within the circumference of the set of circles and can be given as

$$a(\theta) = \left(r_{cb} H \tan\theta \cos\frac{\delta}{2} + \pi r_{cb} \frac{\pi+\delta}{2\pi} \right) - \left(r_{ct}(H-h)\tan\theta\cos\frac{\delta}{2} - \pi r_{ct}\frac{\pi-\delta}{2\pi} \right)$$
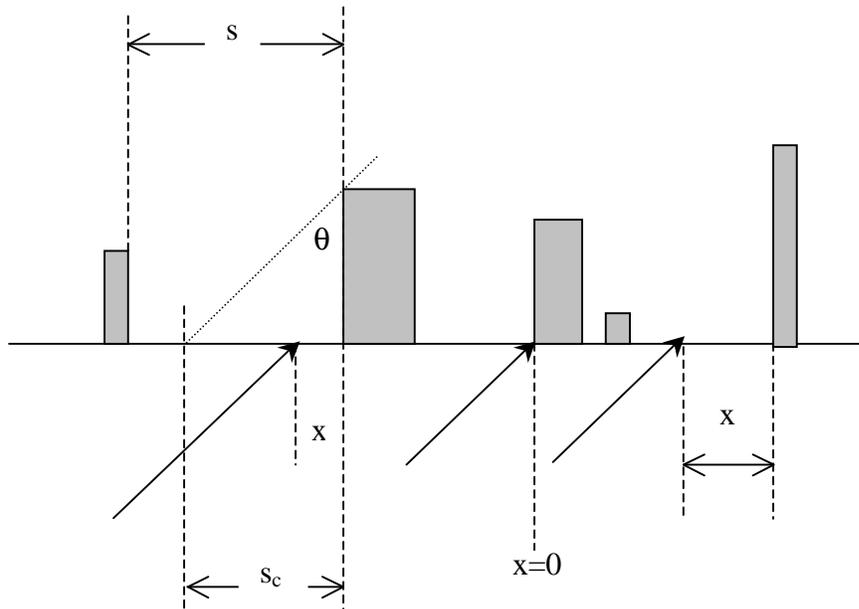
Fig.3.7 Modeling the PCLOS by tracing a line of sight. To pass the cloud field clearly, a line of sight has to penetrate the cloud base in the (1-N) portion of the cloud base plane and the cloud in front of the line has to be far enough away or short enough to not block the line of sight. Note the distance x is measured on the cloud base level between the penetrating point and the nearest cloud to its right.
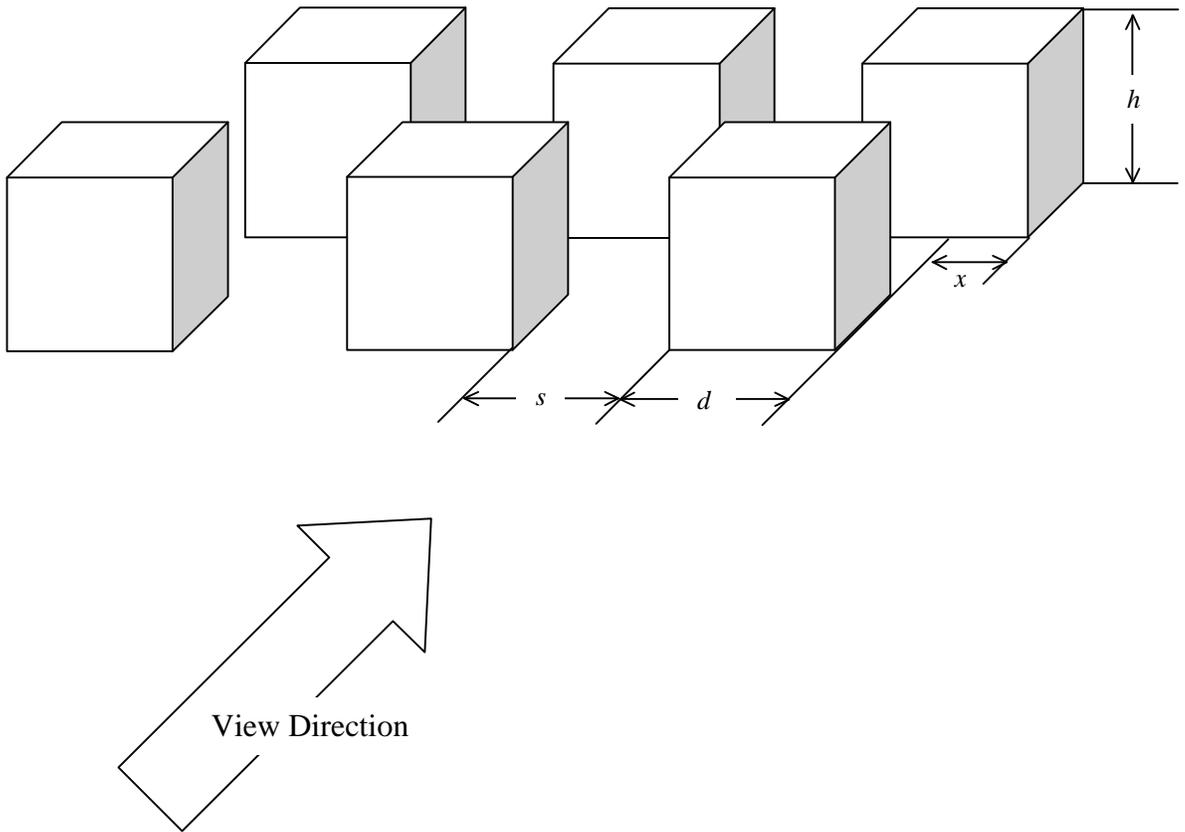
Fig.3.8 Naber and Weinman's ShiftedRegular_Cuboidal model
(After Naber and Weinman 1984). Every row is shifted a distance of *x* with
respect to the adjacent row. Eq. (3.30) applies to the view direction shown in
the figure.
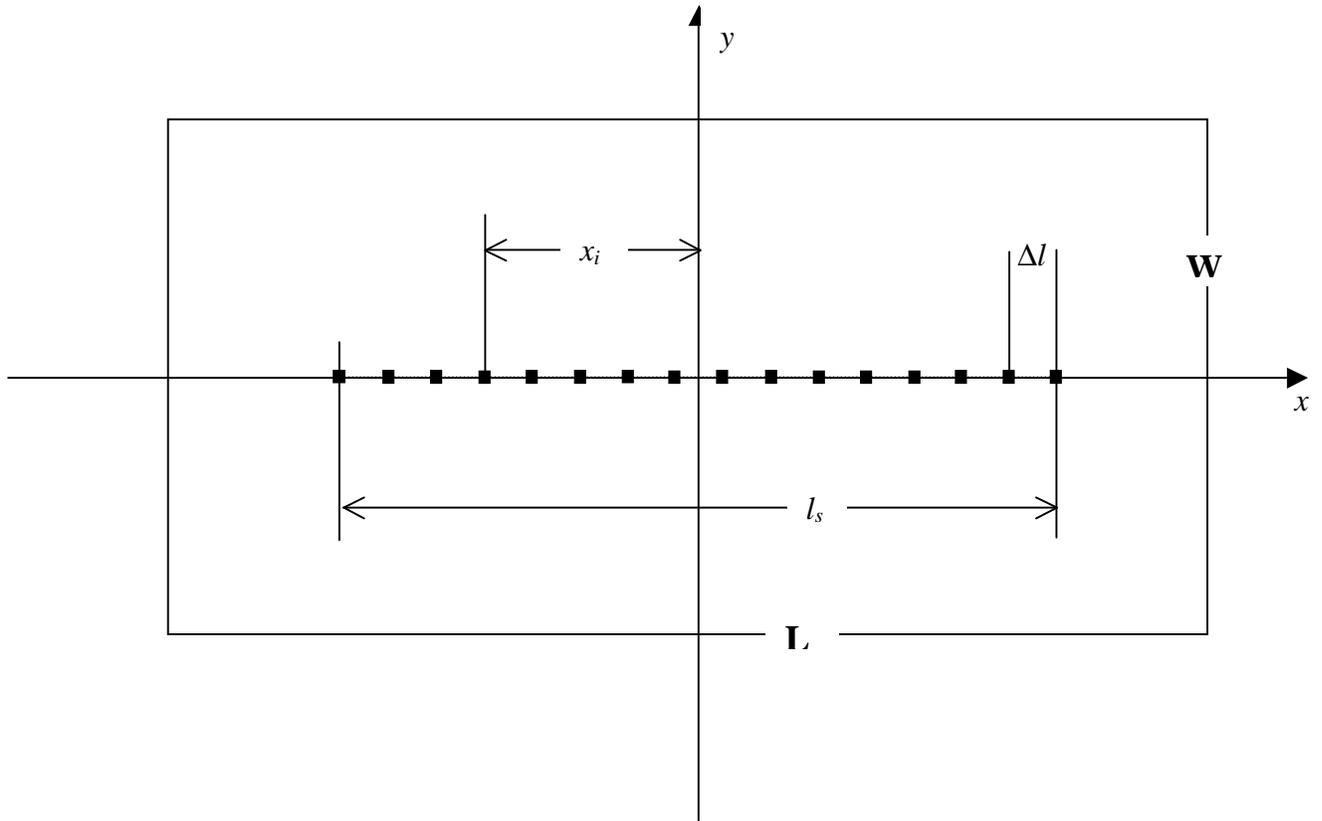
Fig. 4.1 Sampling arrangement for the measurement of the absolute cloud fraction N. Based on the frozen turbulence approximation, observations can be seen as taken along a straight line placed on the center of the domain. In the figure, the domain size is WxL. The length of the sampling line is l_s. Sampling points are regularly spaced on the sampling line.
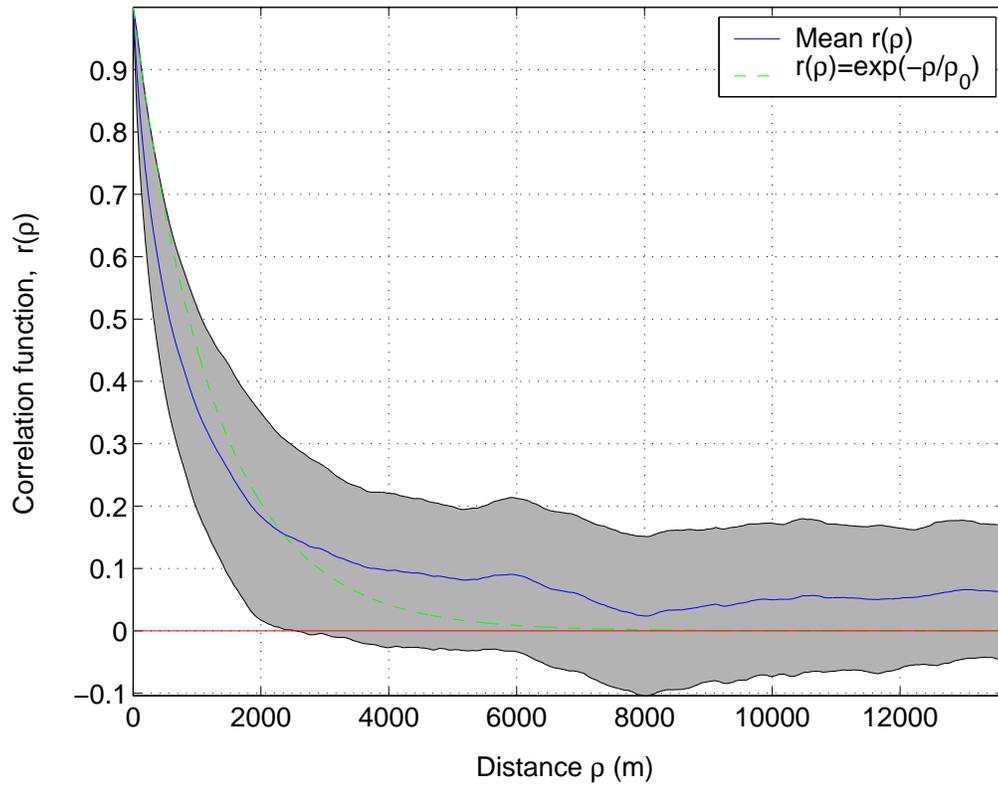
Fig. 4.2, Observed and model correlation functions for cumulus cloud fields over the ARM CART site, derived from 45 days of NFOV data during the spring and summer seasons in the years of 2000 and 2001. Also shown in the figure is the modeled correlation function, $r(\rho) = e^{-\frac{\rho}{\rho_0}}$, with $\rho_0 = 1267m$. The shadowed area represents the standard deviation of the correlation functions.
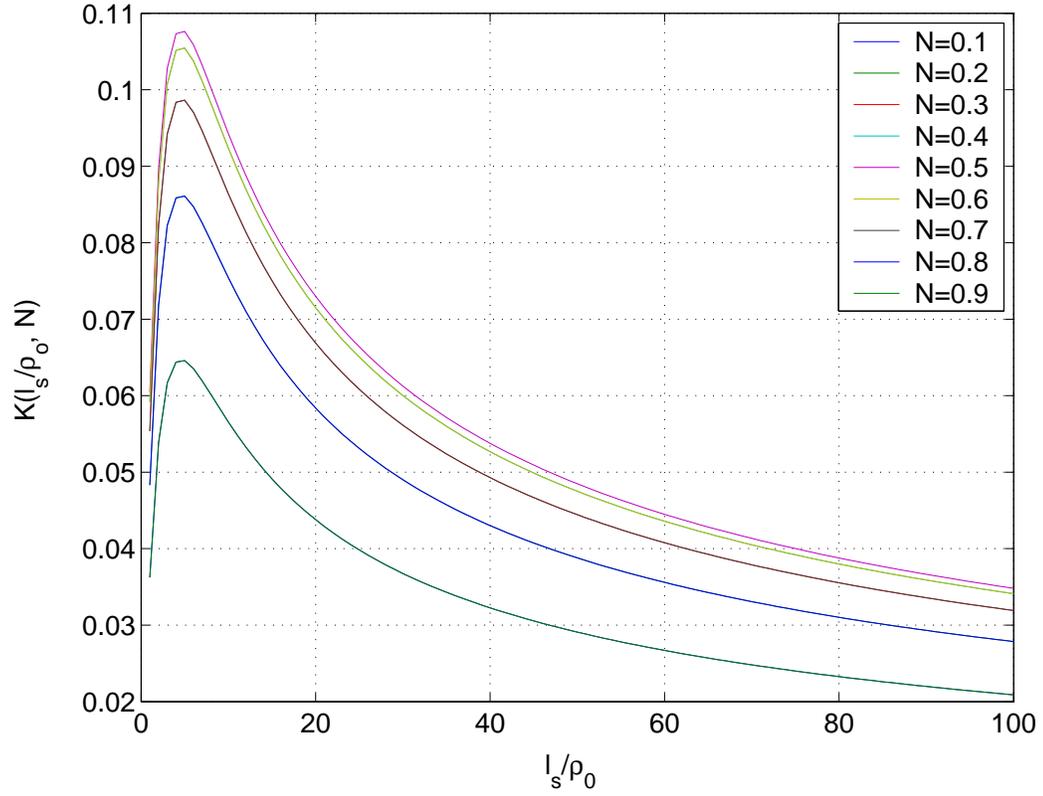
Fig. 4.3. $K(\frac{l_s}{\rho_0}, N)$ as a function of $\frac{l_s}{\rho_0}$ and N. $\frac{l_s}{\rho_0}$ is the relative length of the sampling line. The sensitivity coefficient is written as

$$\frac{d(\text{RMS})}{d\rho_0} \approx \frac{d\sigma_{\hat{N}}}{d\rho_0} = K(\frac{l_s}{\rho_0}, N)\frac{1}{\rho_0} \ .$$

$K(\frac{l_s}{\rho_0}, N)$ has units of cloud fraction and its maximum value occurs when $N = 0.5$.
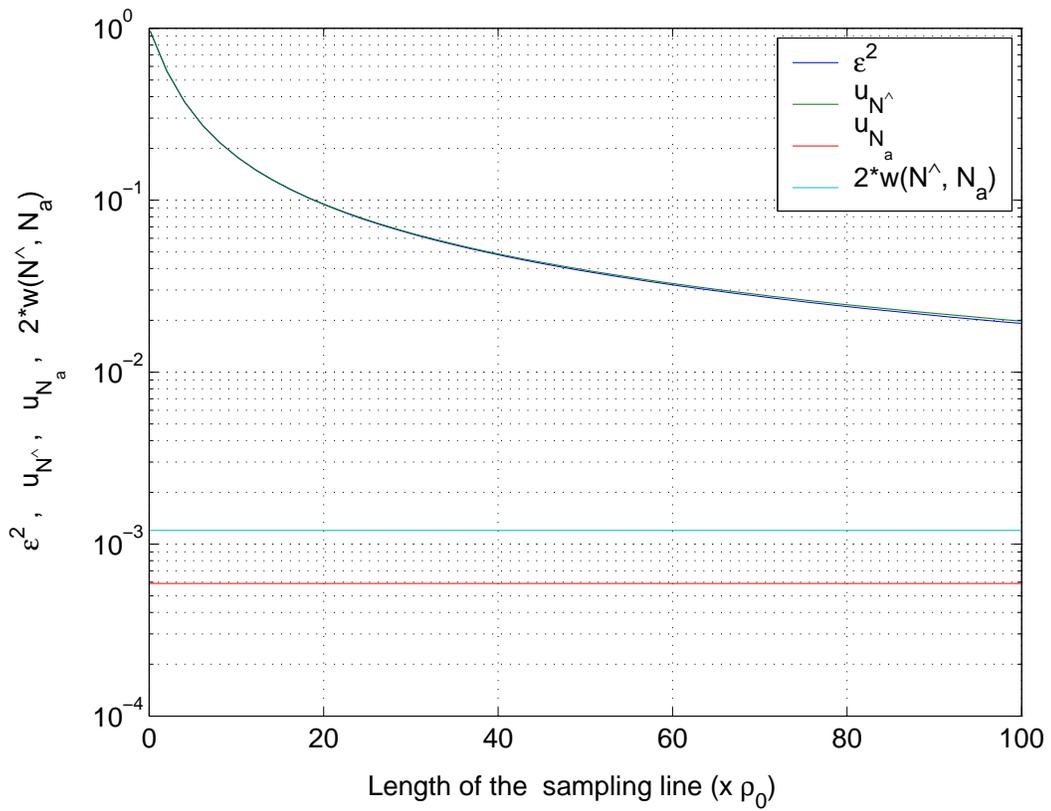
Fig.4.4 ε^2, $u_{\hat{N}}$, u_{N_a} and $w(\hat{N}, N_a)$ as functions of the length of the sampling line, for a domain of $W/\rho_0 = 100$, $L/\rho_0 = 100$. The sampling line is located along L at the center of the domain.
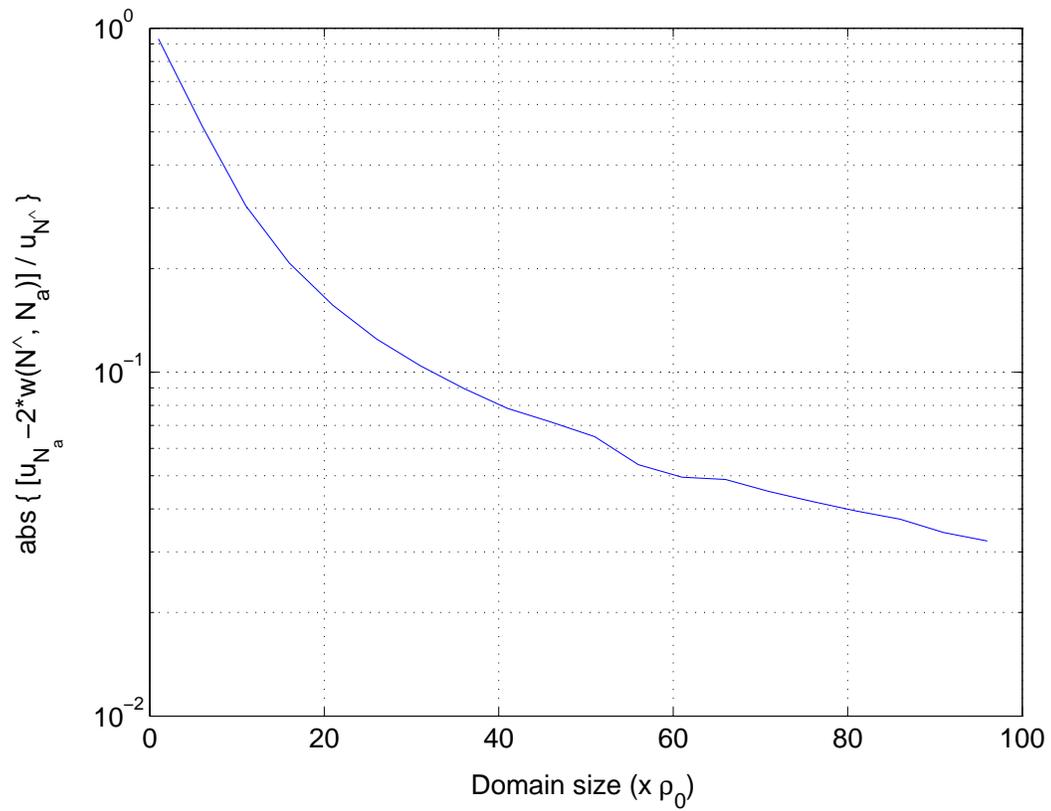
Fig.4.5 The ratio of $\left| u_{N_a} - 2w(\hat{N}, N_a) \right|$ to $u_{\hat{N}}$ as a function of domain size.

The length of the sampling line was set to be the same length as the domain size.
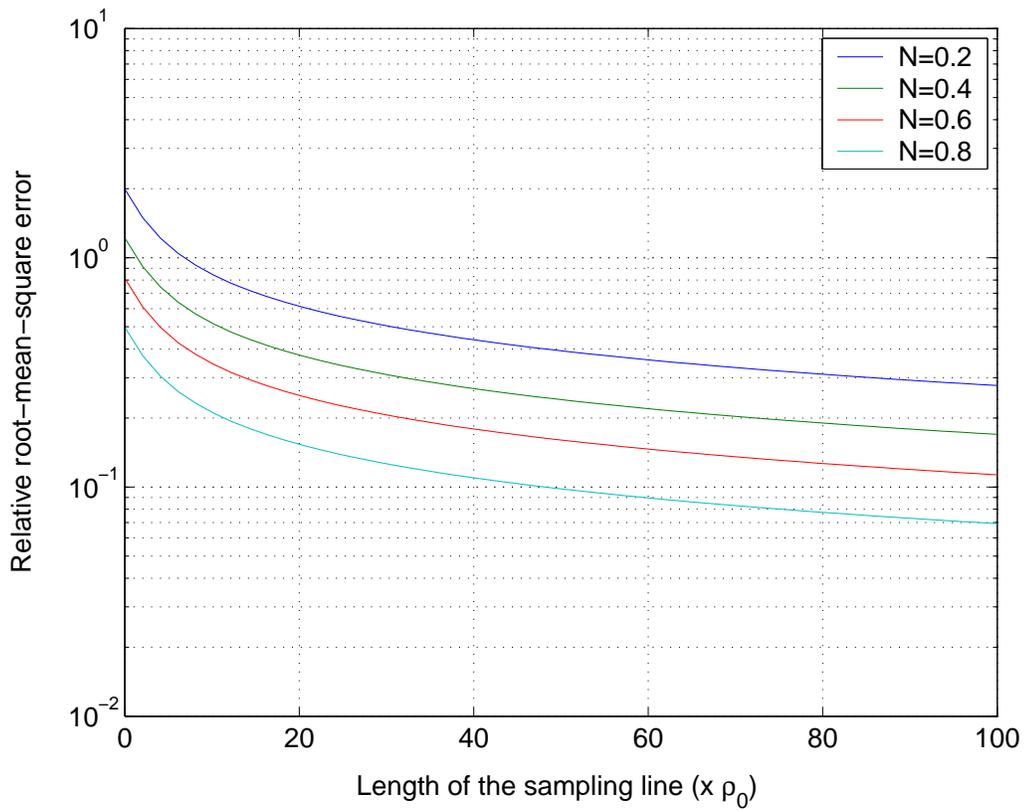
Fig.4.6 The RRMS as a function of the length of the sampling line for different cloud fractions. The domain size is $W = L = 100\rho_0$. The sampling line is located at the center of the domain.
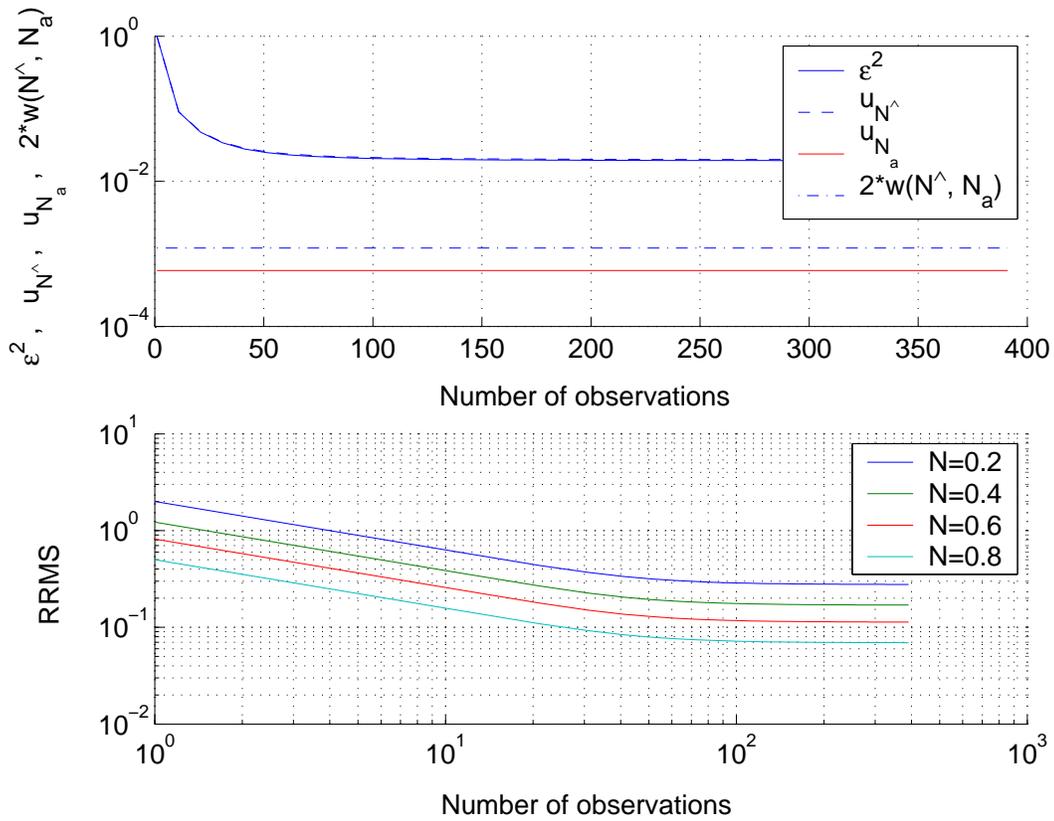
Fig.4.7 Sampling error as a function of the number of observations. Upper panel: ε^2, $u_{\hat{N}}$, u_{N_a} and $w(\hat{N}, N_a)$ as functions of the number of observations. Lower panel: RRMS as a function of the number of observations for various cloud fractions. The domain size is $W = L = 100\rho_0$. The sampling line is positioned at the center of the domain and its length is the same as L. The observation points are regularly distributed on the sampling line with interval $\Delta l = 100\rho_0/n$, where n denotes the number of observations.
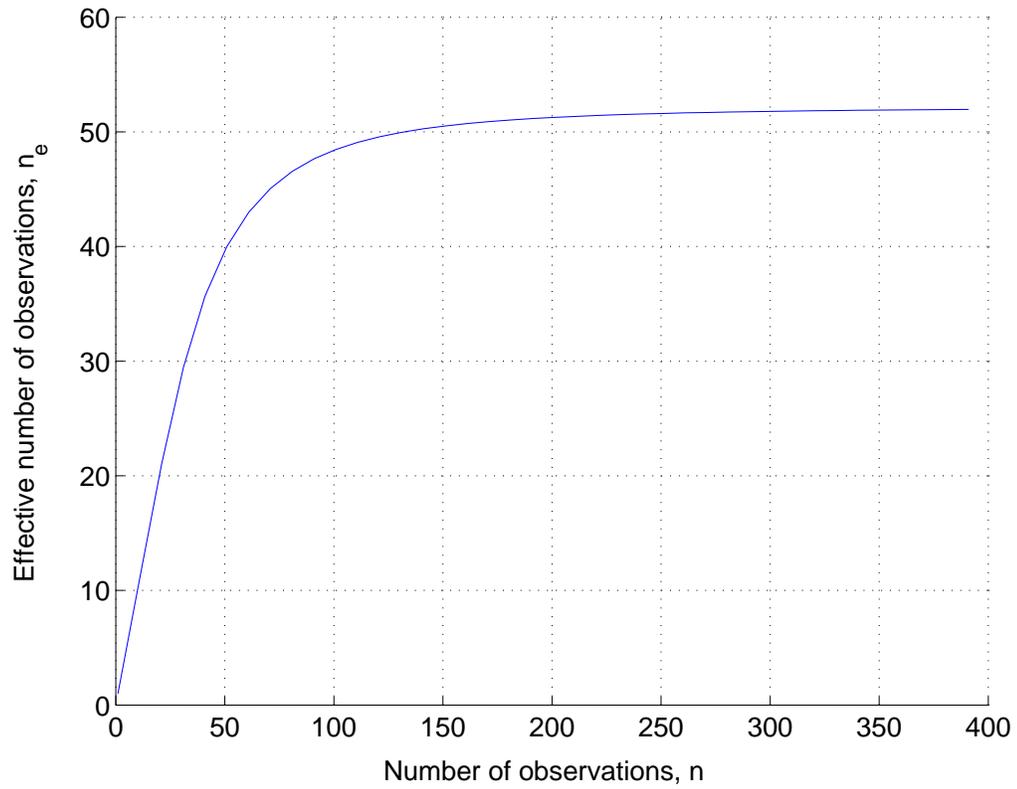
Fig. 4.8 The relationship between the effective number of random observations and the actual number of observations. The effective number is defined as $n_e = \dfrac{\sigma_N^2}{D^2} = \dfrac{1}{\varepsilon^2}$ (Eq. (4.15)).
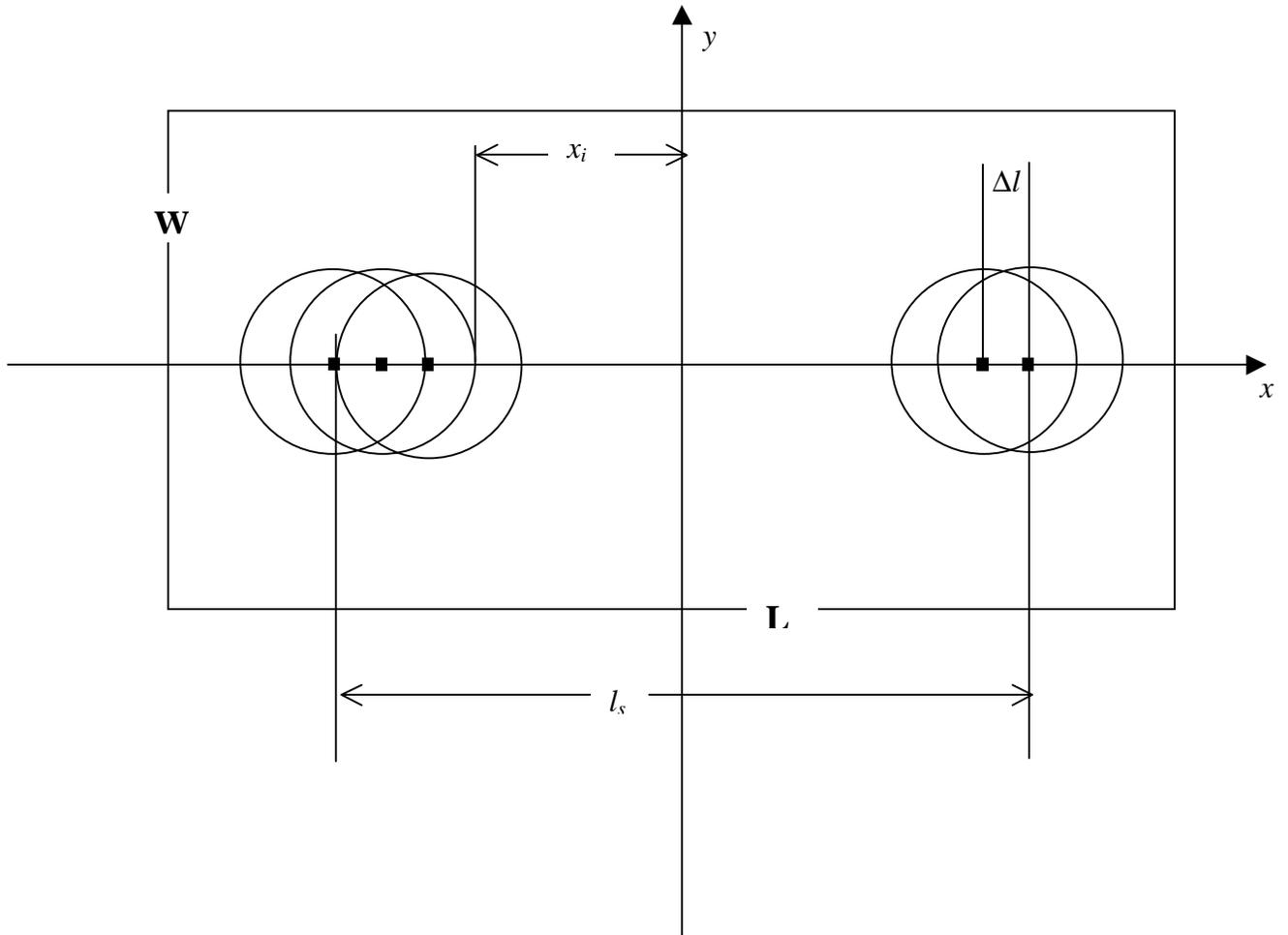
Fig. 4.9 Sampling arrangement for the PCLOS. The PCLOS is a function of, θ, the zenith angle. The estimation of the PCLOS(θ) is made by averaging over a set of circles centered on the sampling line. The sampling error here refers to the difference between the domain ($W \times L$) averaged PCLOS(θ) and the one averaged over the set of circles.
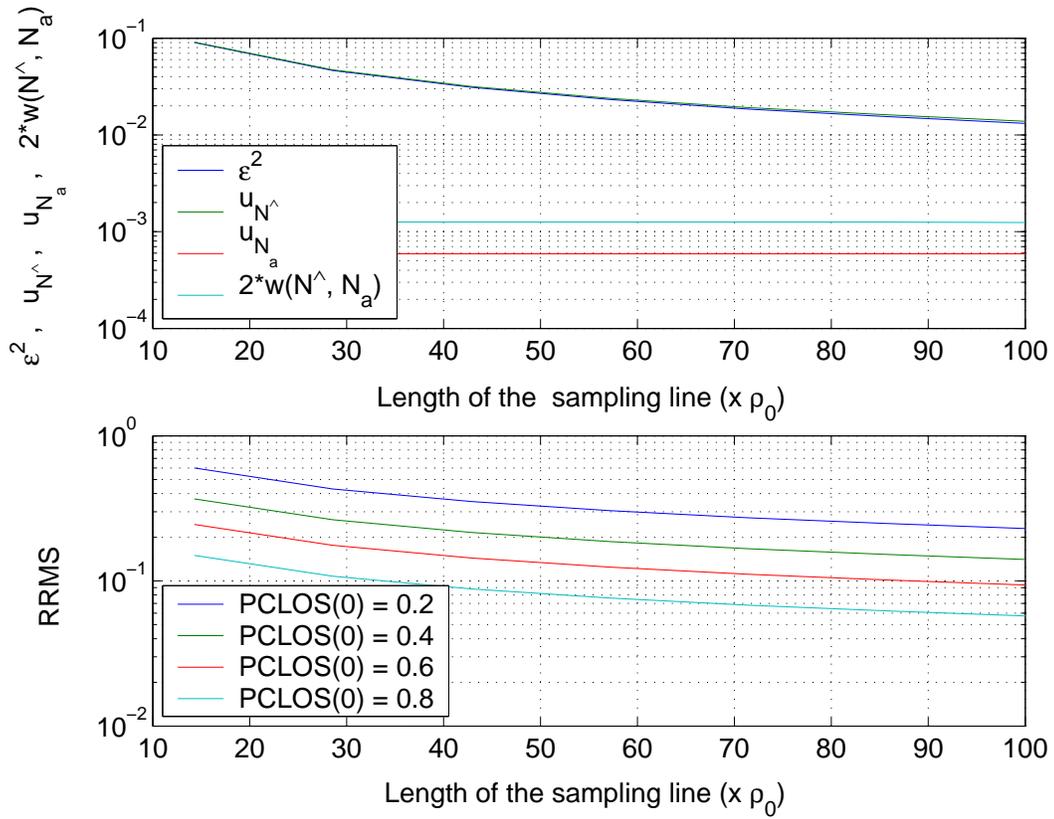
Fig. 4.10 Samping error for the measurement of PCLOS for a $100\rho_0 \times 100\rho_0$ domain. The circle radius $R = \rho_0$, which corresponds to a zenith angle of 45° for a cloud base of height ρ_0. The set of circles are regularly aligned along the centerline of the domain with interval $\Delta l = 0.6\rho_0$. Upper panel: ε^2, $u_{\hat{N}}$, u_{N_a} and $w(\hat{N}, N_a)$ as functions of the length of the sampling line. Lower panel: the RRMS as a function of the length of the sampling line.
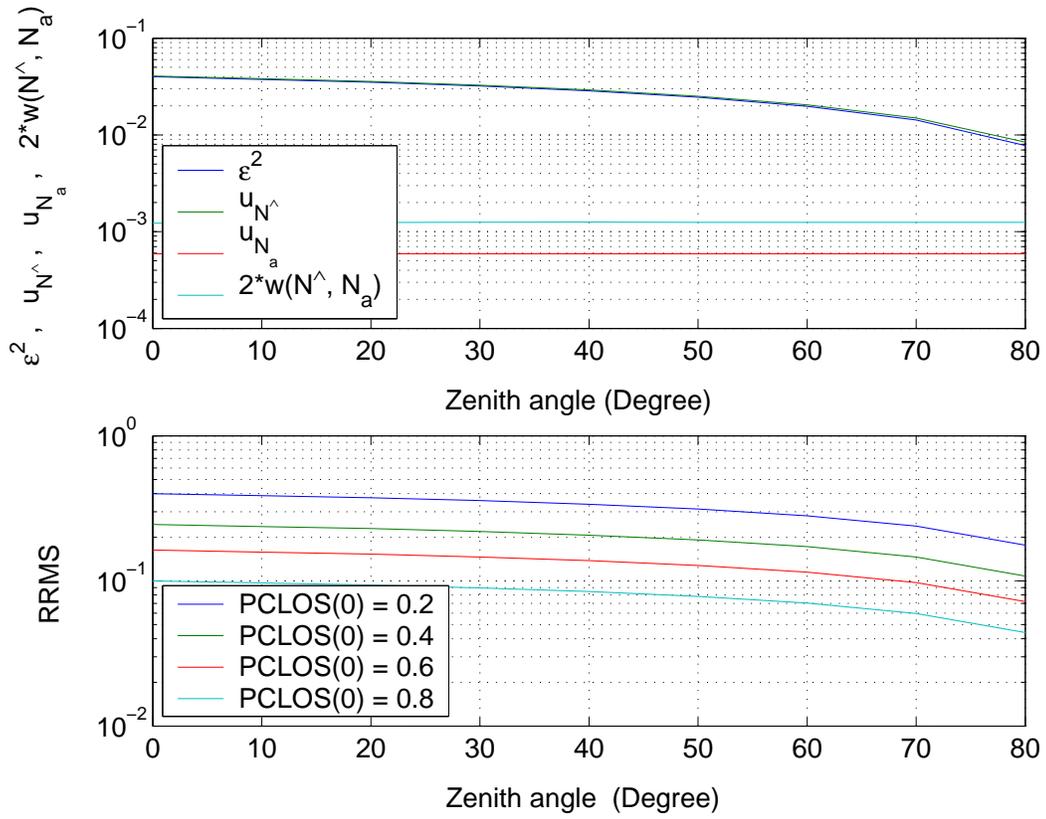
Fig. 4.11. Upper panel: model parameters ε^2, $u_{\hat{N}}$, u_{N_a} and $w(\hat{N}, N_a)$ as functions of zenith angle. Lower panel: the relationship between the RRMS and the zenith angles for the cloud base height H $= \rho_0$. The set of circles are regularly spaced along a sampling line of length $l_s = 50\rho_0$, and with the interval $\Delta l = 0.6\rho_0$.

BOMEX, N=0.16

Area=6.4 km^2, Δ=0.05 km, (128x128)

ATEX, N=0.57

Area=6.8 km^2, Δ=0.1 km, (68x68)

OPENCEll, N=0.92

Area=50 km^2, Δ=0.4 km, (128x128)

GATE, N=0.46

Area=400 km^2, Δ=2 km, (201x201)

(a) (b) (c) (d)
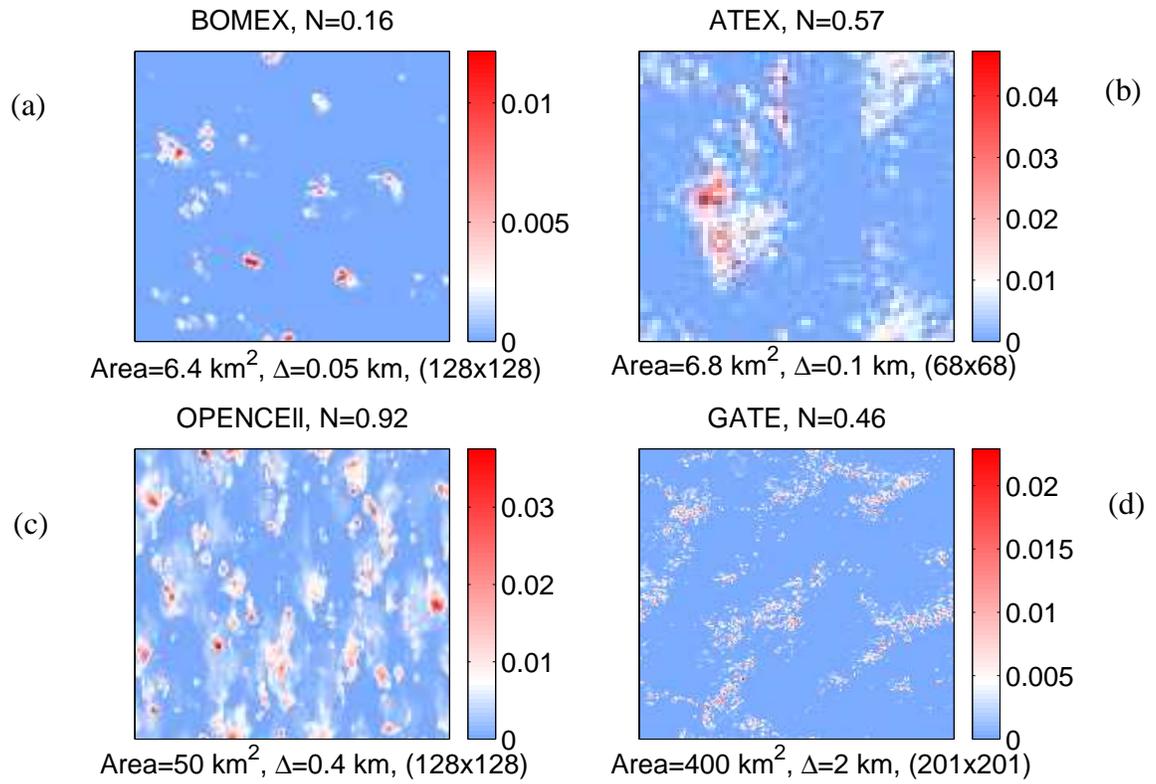
Fig. 4.12. The LES/CRM simulated cloud fields. (a) BOMEX; (b) ATEX; (c) OPENCELL; (d) GATE. The color scales shown in the figure represent the Liquid Water Path (LWP) of the fields in the unit of g/m^2.
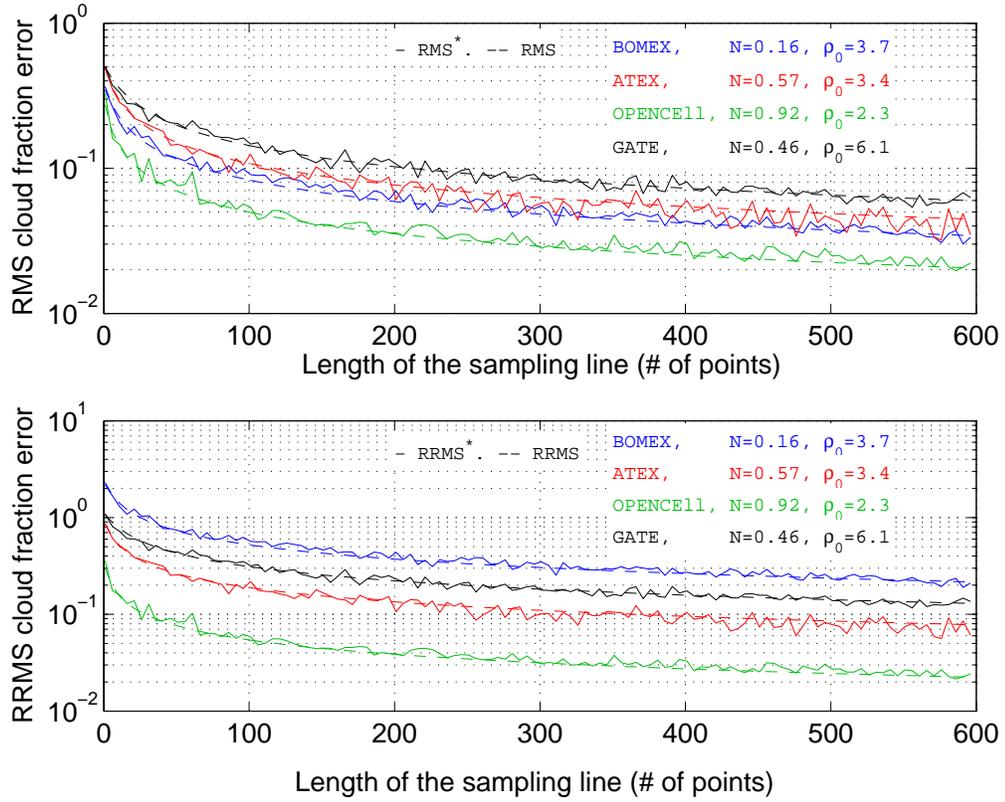
Fig. 4.13. Application to four LES/CRM generated cloud fields. Upper panel: RMS[*] and RMS changing with the length of the sampling line and the cloud fraction *N*. Lower panel: RRMS[*] and RRMS changing with the length of the sampling line and *N*. The RMS and the RRMS are calculated as:

$$RMS = \sqrt{N(1-N)u_{\hat{N}}^2} \ , \qquad RRMS = \frac{RMS}{N} = \frac{\sqrt{N(1-N)u_{\hat{N}}^2}}{N}$$

The RMS[*] and RRMS[*] are calculated as:

$$\text{RMS}^*(l_s) = \sqrt{\frac{1}{n}\sum_{i=1}^{n}(\hat{N}_{l_s,i} - N)^2} \qquad\qquad \text{RRMS}^*(l_s) = \text{RMS}^*(l_s)/N$$

where, N is the desired domain-averaged cloud fraction, *n* is the number of simulations for each sampling line length l_s. $\hat{N}_{l_s,i}$ (*i*=1, *n*; l_s=1, 600) is the estimated cloud fraction from the *i*[th] single-line measurement of length l_s.
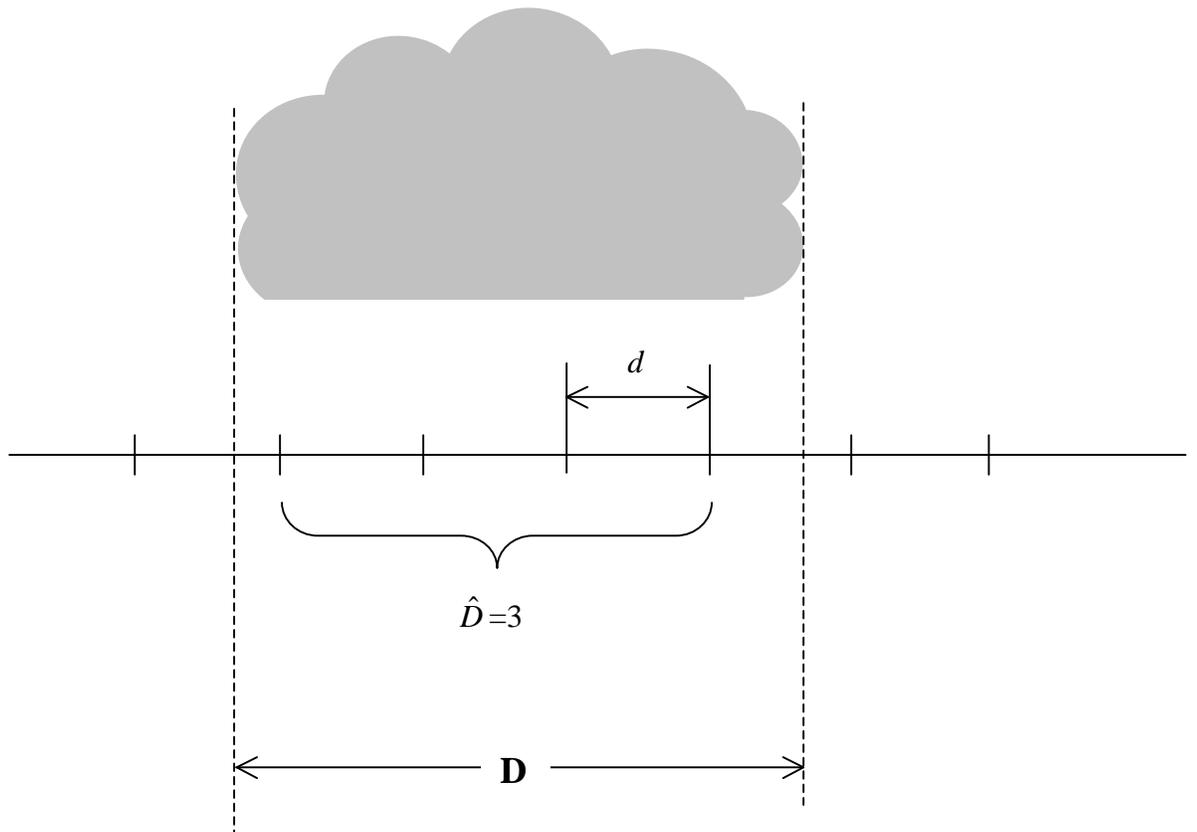
Fig. 4.14 Illustrations of the terms associated with the measurement of the cloud horizontal size or spacing with limited sampling rate. Only the integer part of D will be reported by the instrument. In the above case, the instrument will report the cloud size to be $\hat{D}=3$. Randomly placing the "ruler" with respect to the position of the cloud, the variance of the measurement would be $\sigma^2 = [d - rem(D,d)]\, rem(D,d)$, where $rem(D,d)$ represents the remainder of D divided by d.
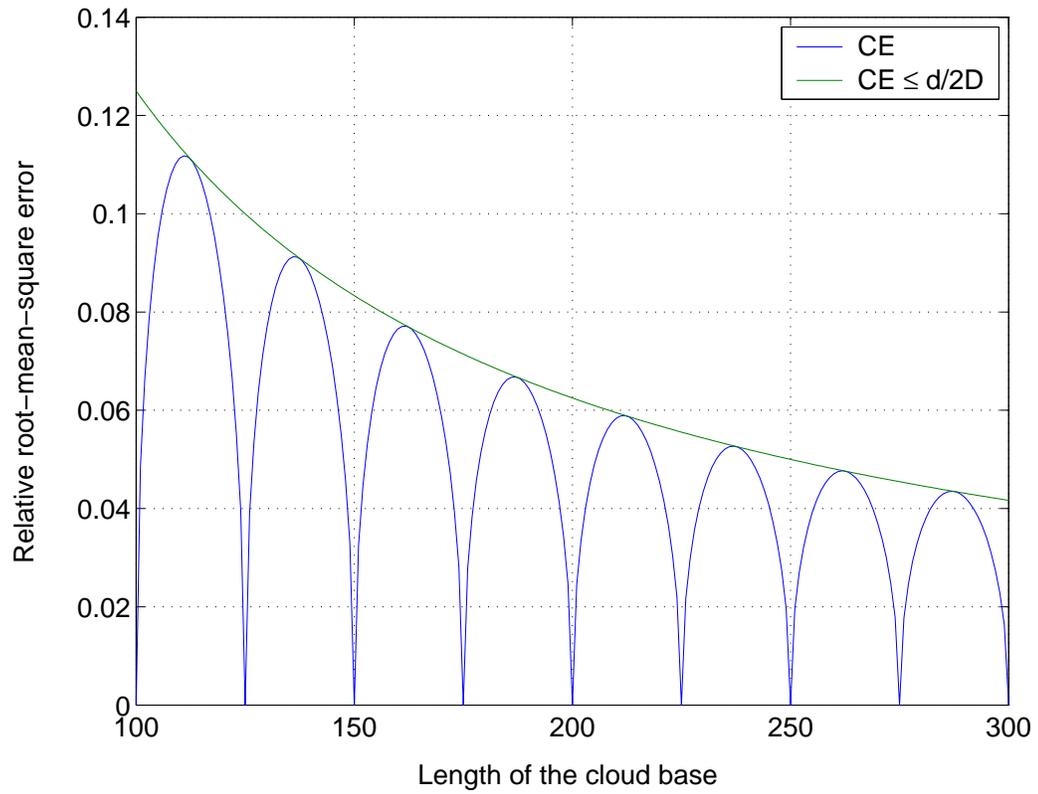
Fig. 4.15 Relative error due to the limited sampling rate when measuring the cloud base length. *d* denotes the sampling interval and *D* is the real length of the cloud base.
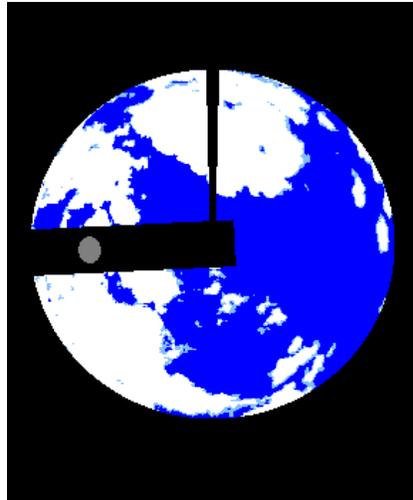
1: clear sky,
2: thin cloud,
3: thick (opaque) cloud,
4: ignored (masked) pixels.

(a)

1	2	3	4	5	6	7
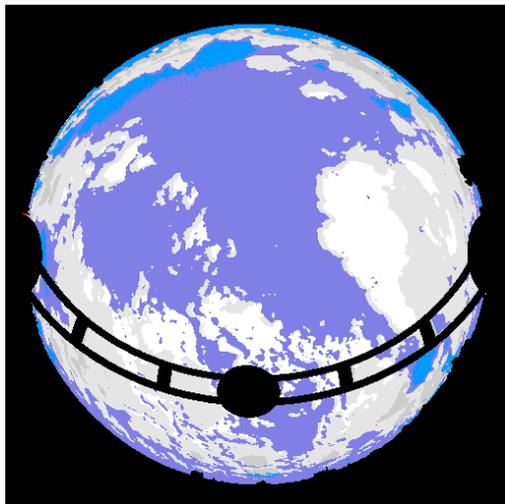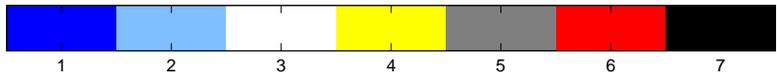
1: clear (spectral and density);
2: aerosol (spectral);
3: mixed aerosol and cloud (spectral);
4: bright cloud (spectral);
5: intermediate cloud (spectral);
6: dark cloud (spectral);
7: translucent (density);
8: opaque (density);
9: indeterminate (spectral and density);
10: undefined.

(b)

1	2	3	4	5	6	7	8	9	10
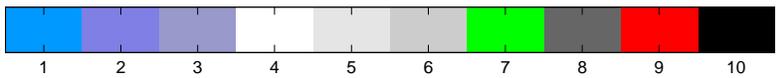
Fig. 5.1 The TSI (a) and the WSI (b) cloud decision images.
Zenith is at the picture center.

$$\theta = 1.2^{-5}r^3 - 1.4^{-3}r^2 + 0.6r - 0.49$$
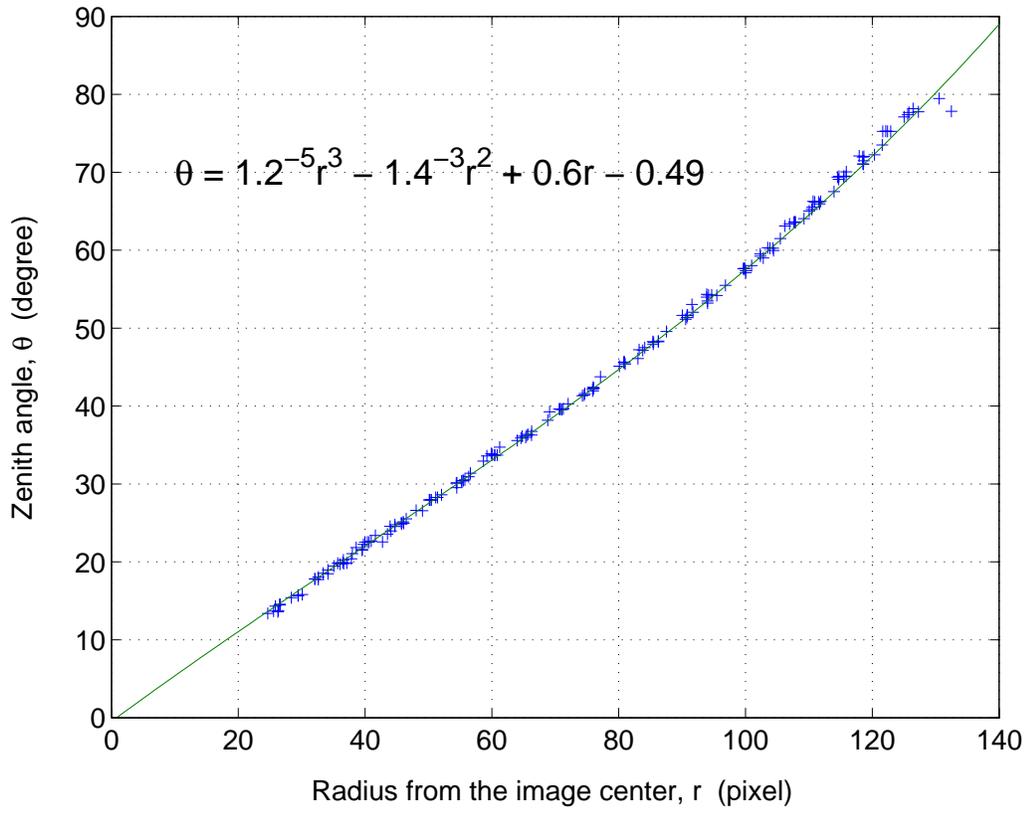
Fig. 5.2 Mapping function between the zenith angle and the radial distance of a TSI pixel.
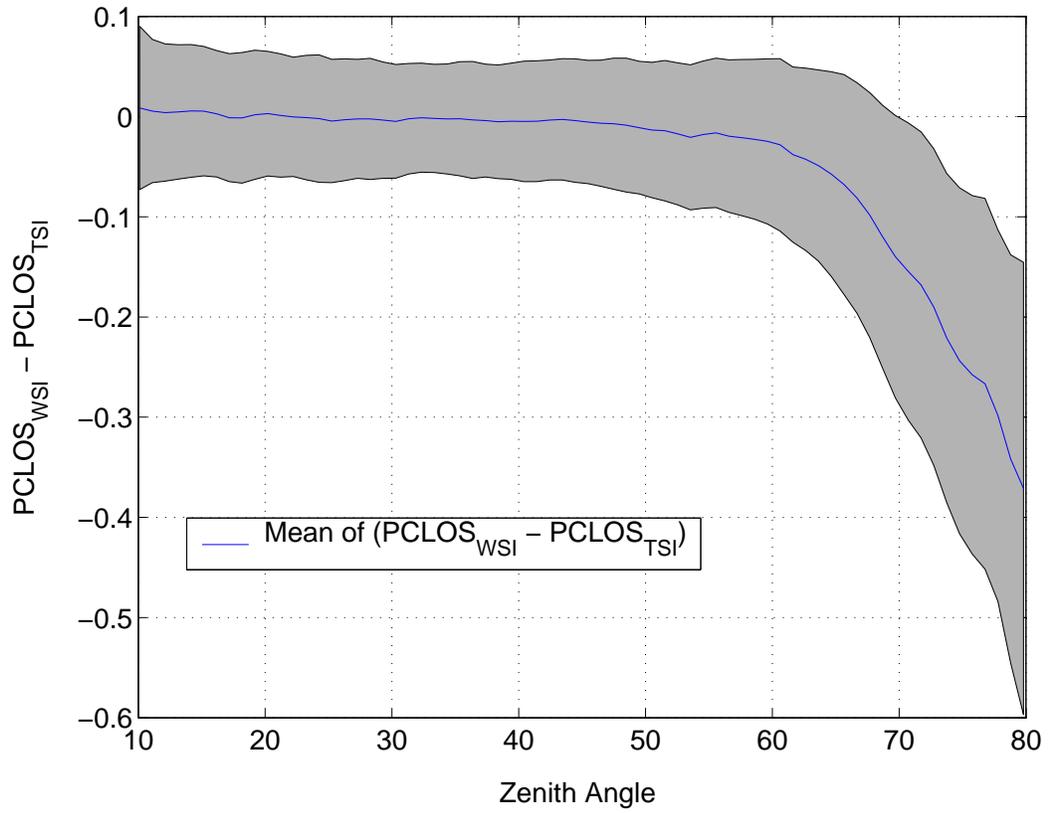
Fig. 5.3 The difference between the PCLOS values estimated from the WSI and the TSI. The blue line is the average of ($PCLOS_{WSI}$ – $PCLOS_{TSI}$) over 77 cases. The shadowed region represents the standard deviation of the differences.
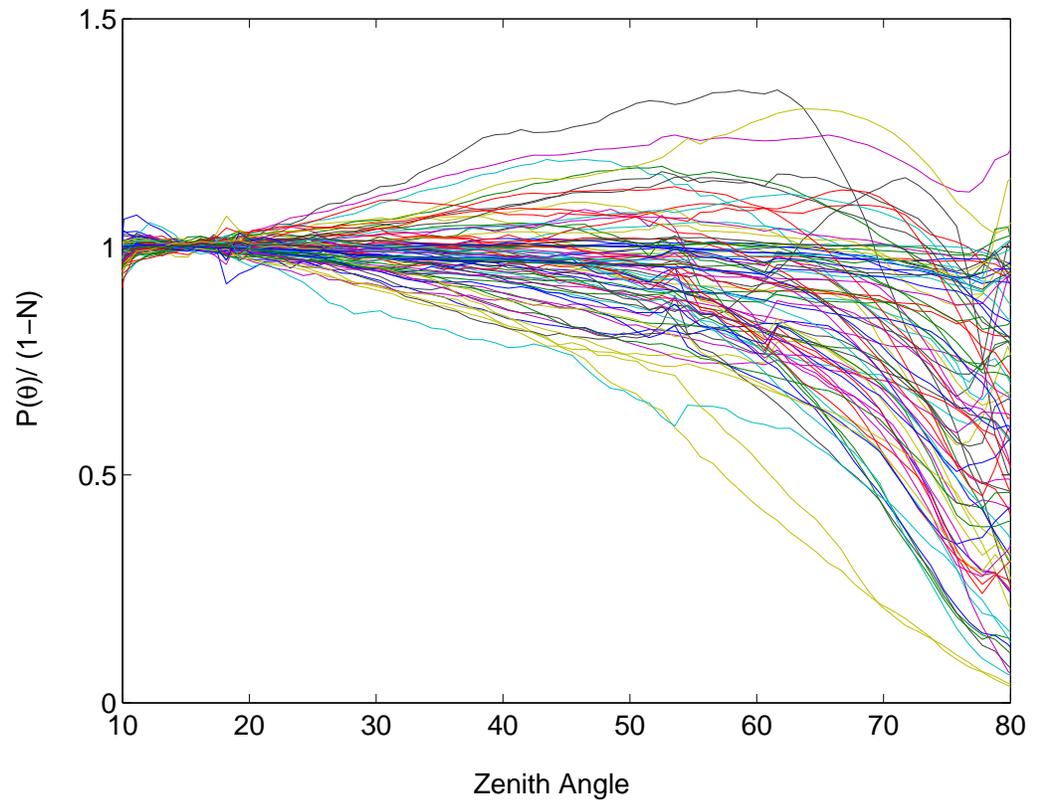
Fig. 5.4 The PCLOS inferred from the TSI. The curves have been normalized as PCLOS(θ)/(1-N), which represents the conditional probability of a clear line of sight given the line of sight starting from the (1-N) portion of the cloud base plane.
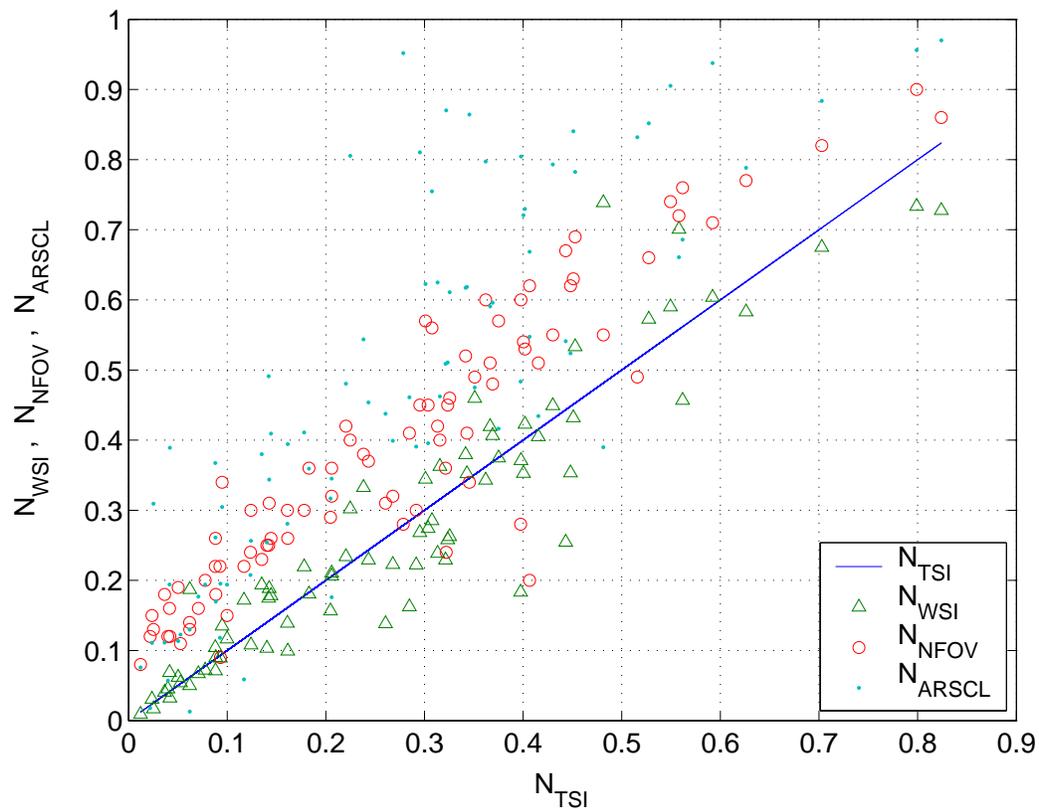
Fig.5.5 A comparison of the absolute cloud fractions estimated from the TSI, WSI, NFOV and the ARSCL cloud base data. (86 cases for the TSI, NFOV and ARSCL; 77 cases for the WSI.)
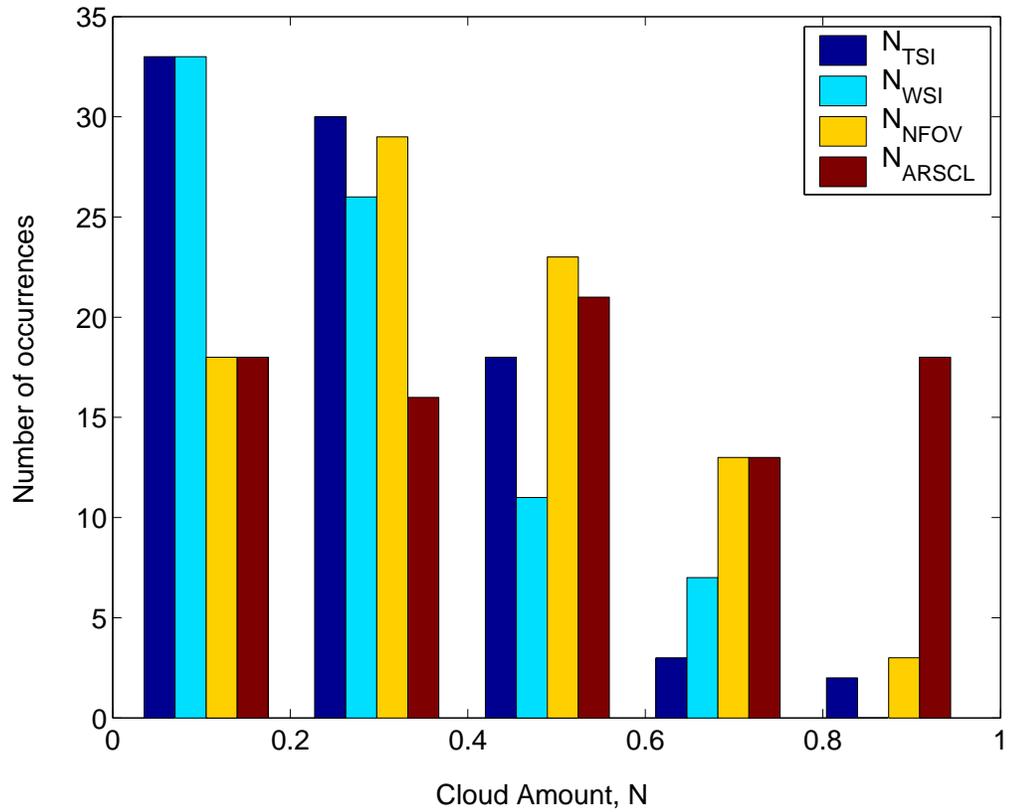
Fig. 5.6 Histogram of the absolute cloud amount, *N*, from different instruments for cases selected during the spring and summer seasons in 2000 and 2001. (86 cases for the TSI, NFOV and ARSCL; 77 cases for the WSI.)
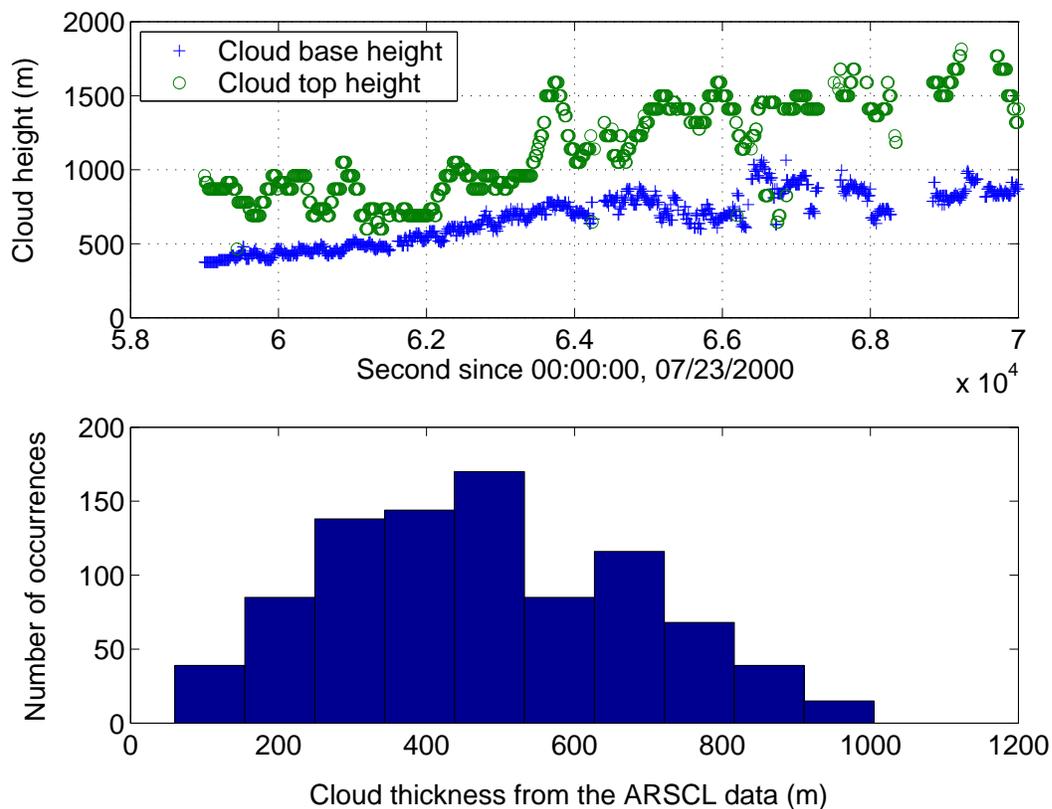
Fig. 5.7 An example of ARSCL cloud thickness data from 23 July 2001. The upper panel: cloud base and top height from the MPL, VCEIL, and MMCR. The lower panel: histogram of the cloud thickness, which is evaluated by subtracting the base heights from the corresponding top heights for every observation moment.
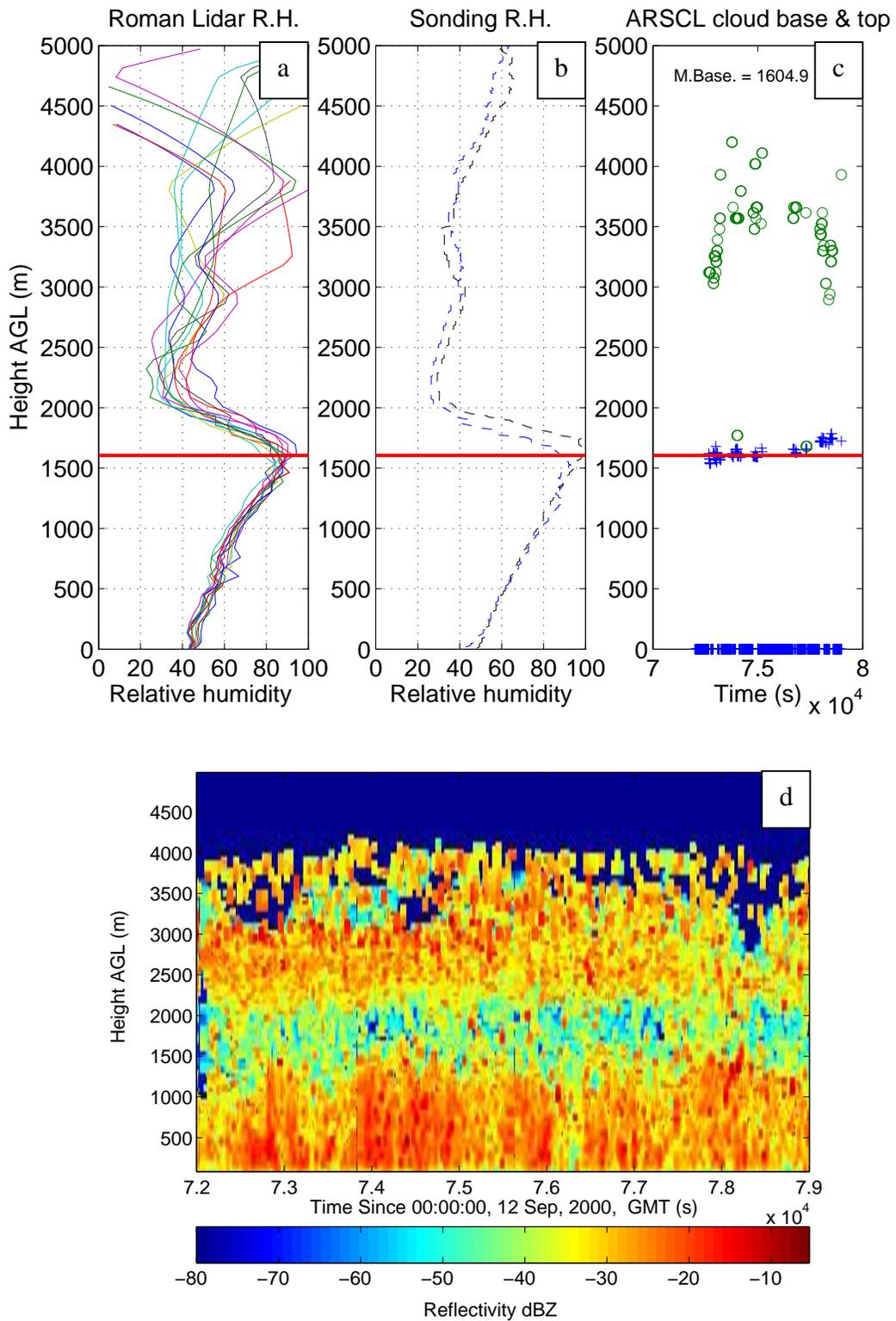
Fig.5.8 Determining the cloud thickness with the aid of relative humidity profiles from Raman Lidar (RL) and soundings. Panel (a) and (b) are relative humidity (R.H.) profiles from the RL and soundings. Panel (c) is the cloud base and top heights from the ARSCL data. Panel (d) is the MMCR reflectivity data obtained at the same period as the profiles.
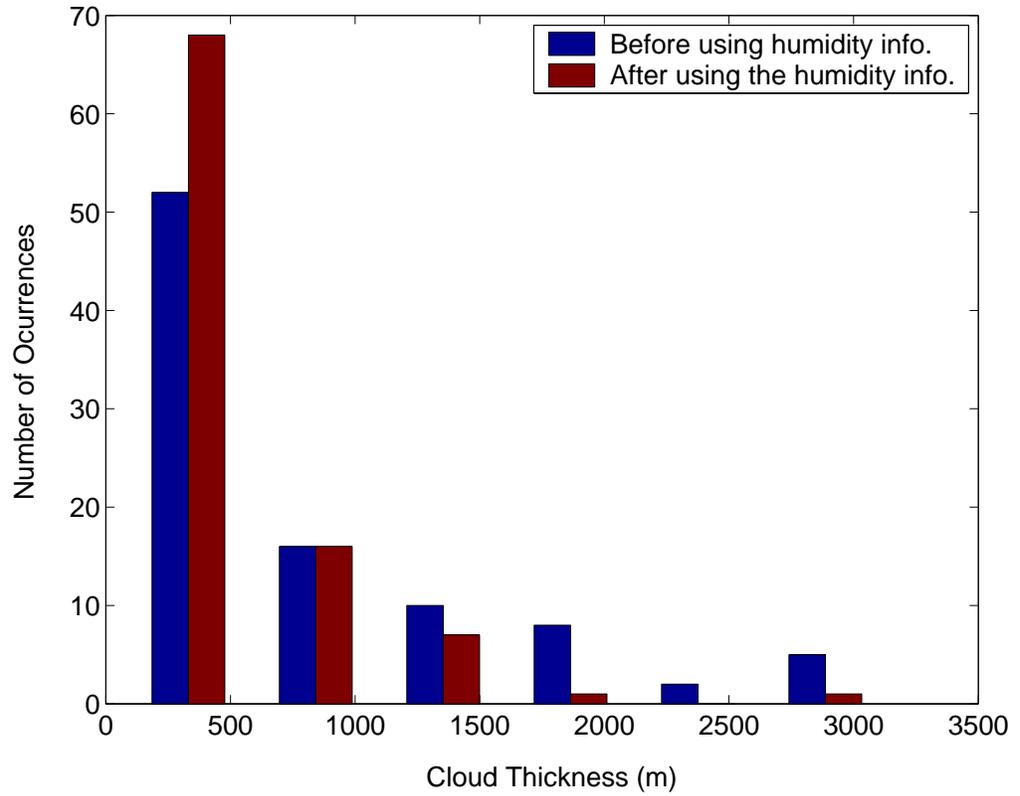
Fig.5.9 Histograms of the cloud thicknesses determined before and after taking into account the relative humidity information, for all 93 cases.
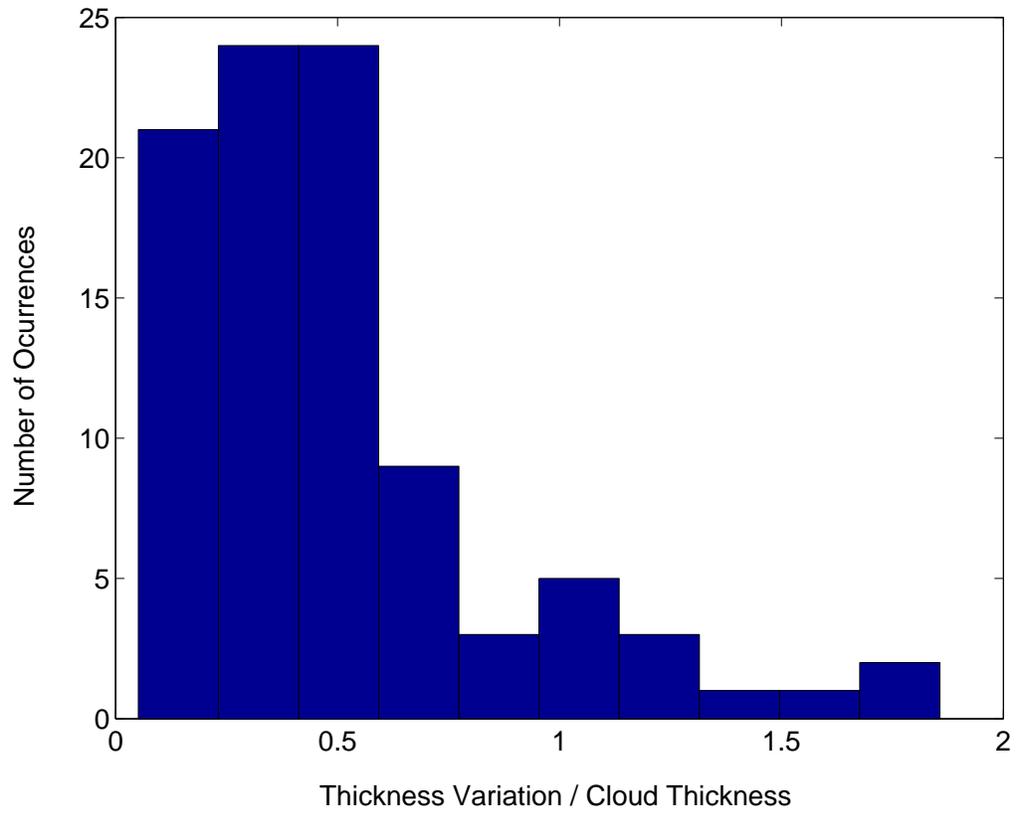
Fig. 5.10 Histogram of the relative cloud thickness variation (thickness variation to cloud thickness) for all 93 cases selected from July 2000 to 2001.
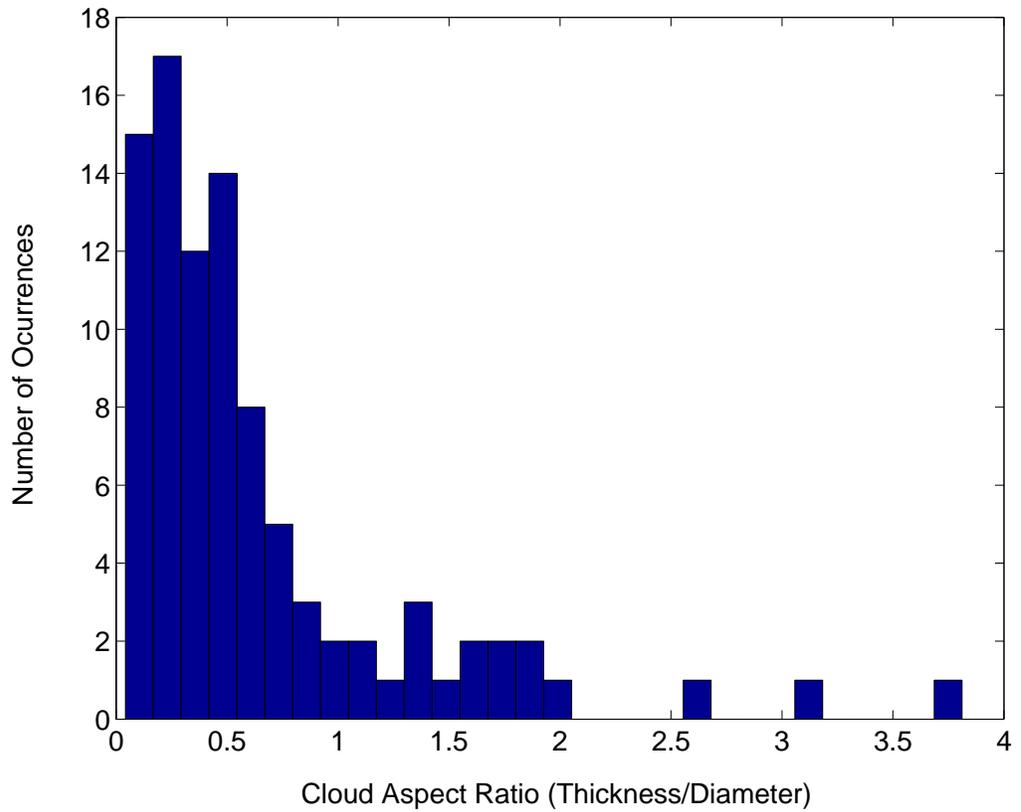
Fig. 5.11 Histogram of the aspect ratios (= cloud thickness over cloud diameter) for all 93 cases selected from July 2000 through 2001.
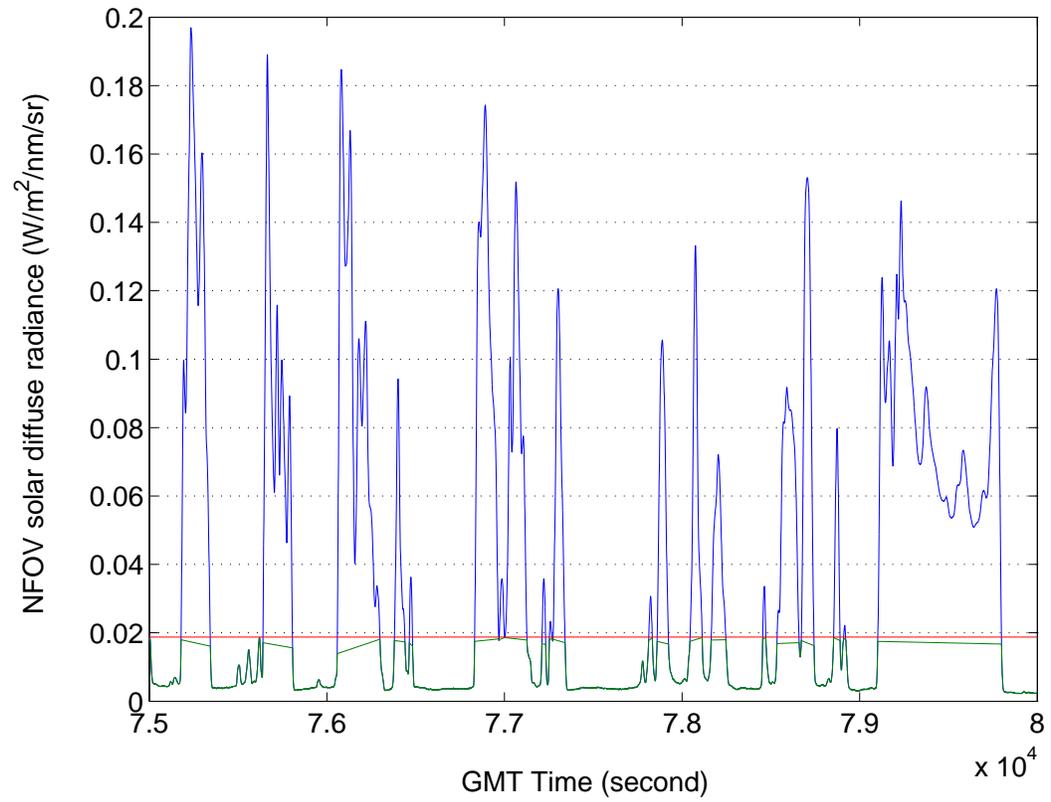
Fig. 5.12 A time series of NFOV radiance data at 869 nm for 22 July 2000. The red line is the threshold.
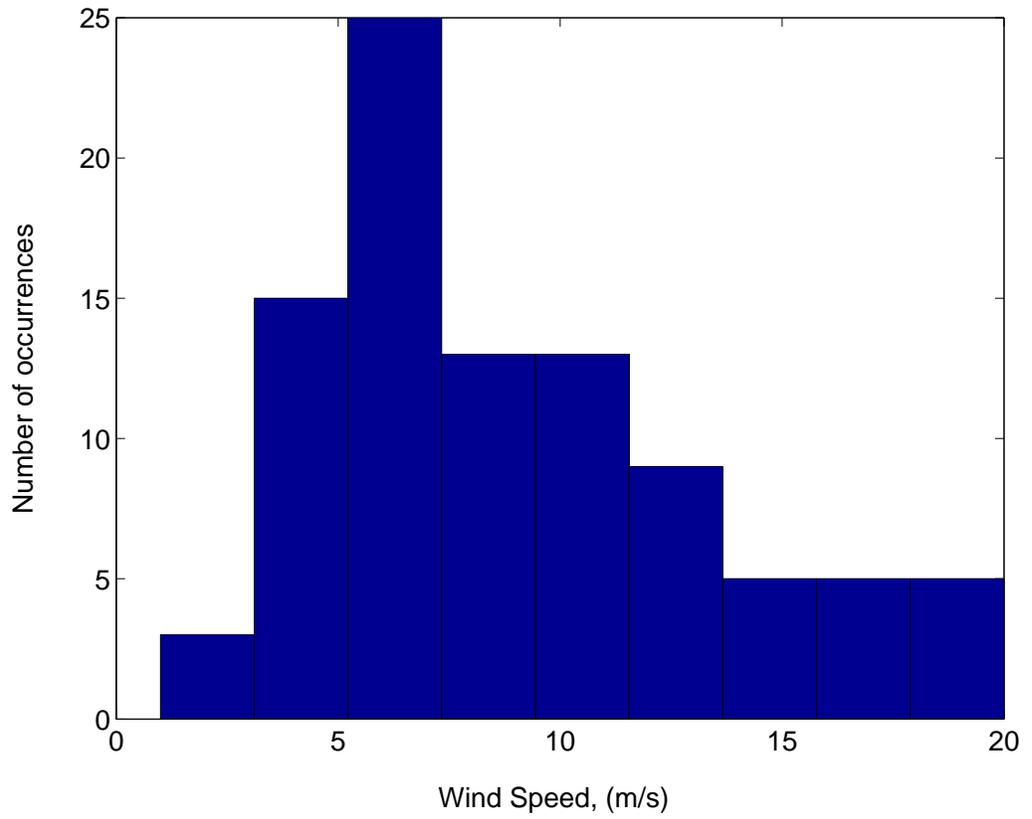
Fig. 5.13 Histogram of the wind speeds obtained from the 915 MHz Radar Wind Profiler (RWP915) for all 93 cases selected from July 2000 to October 2001.
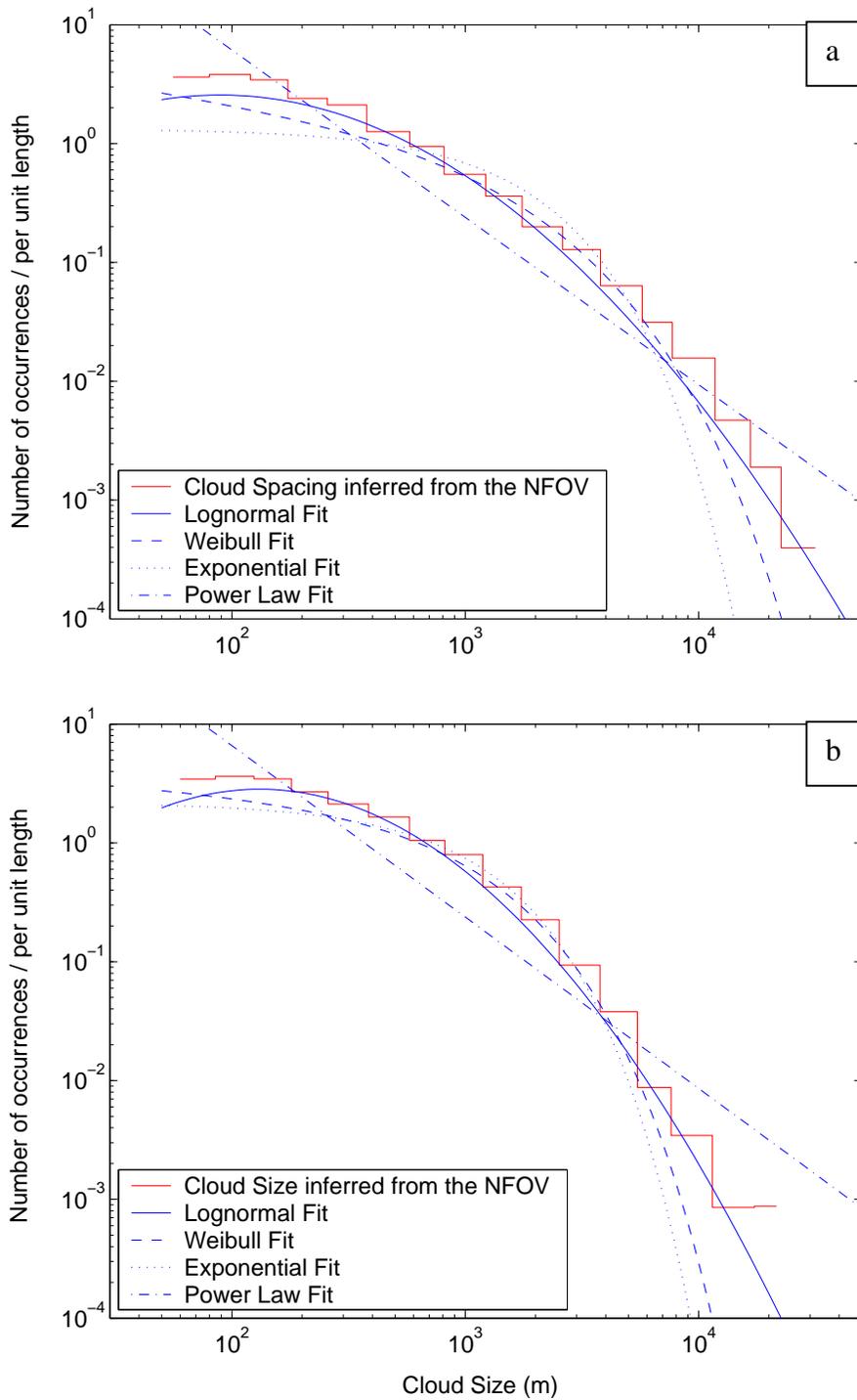
Fig. 5.14 The cloud spacing (a) and cloud size (b) distributions for all cases selected from July 2000 through October 2001. The spacing and size are inferred from the NFOV data. Also shown in the figures are four theoretical distributions.
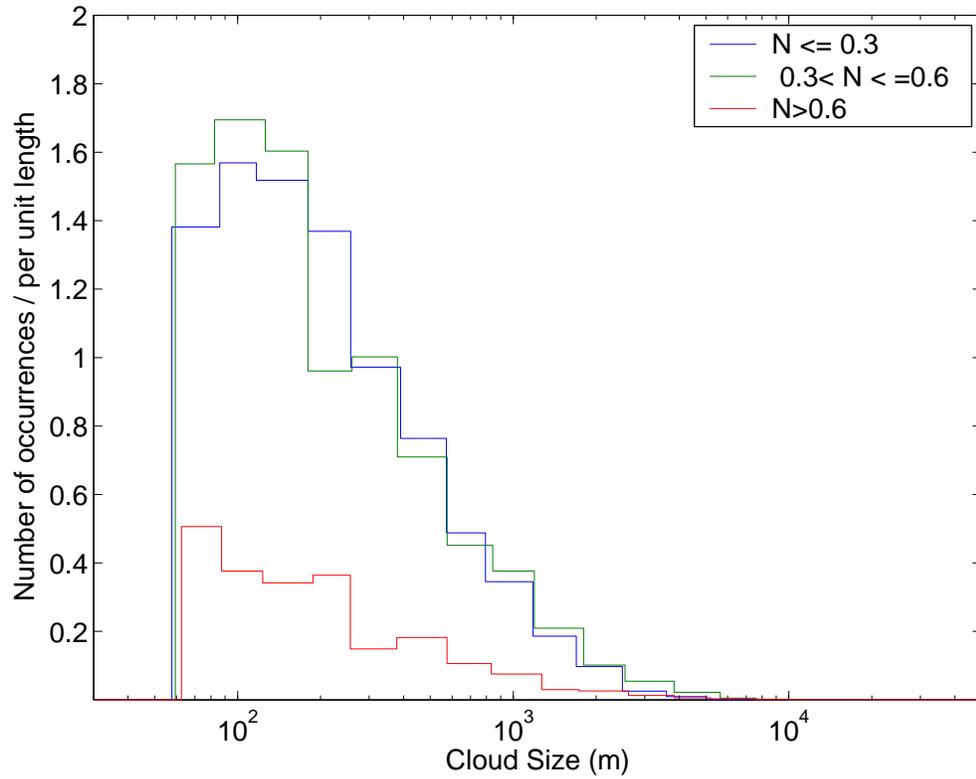
Fig.5.15, Histograms of cloud size distributions as a function of the cloud fraction. The cloud fractions are grouped into three groups, 0 – 0.3, 0.3 – 0.6, 0.6 – 1.
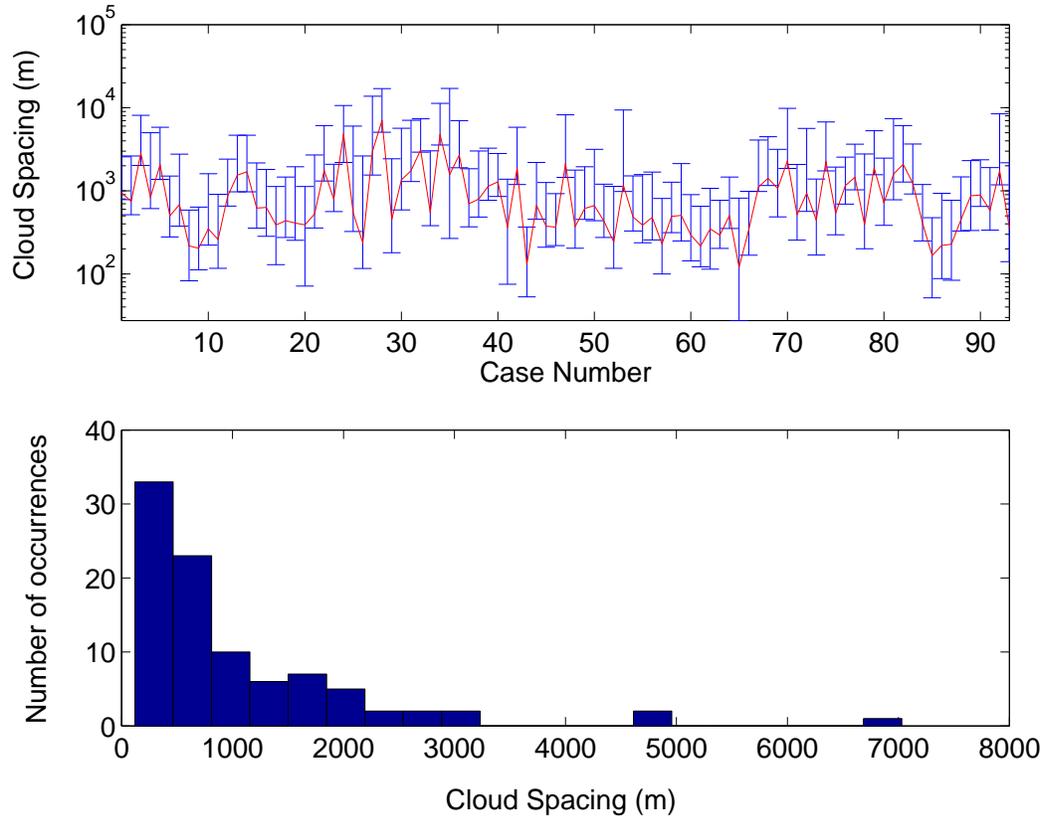
Fig. 5.16 The range of variation of the cloud spacings for the data used in this study. The upper panel shows the range of variations of the cloud spacings; The lower panel is the histogram of the obtained cloud spacings. The red line in the upper panel represents the median values of the cloud spacing.
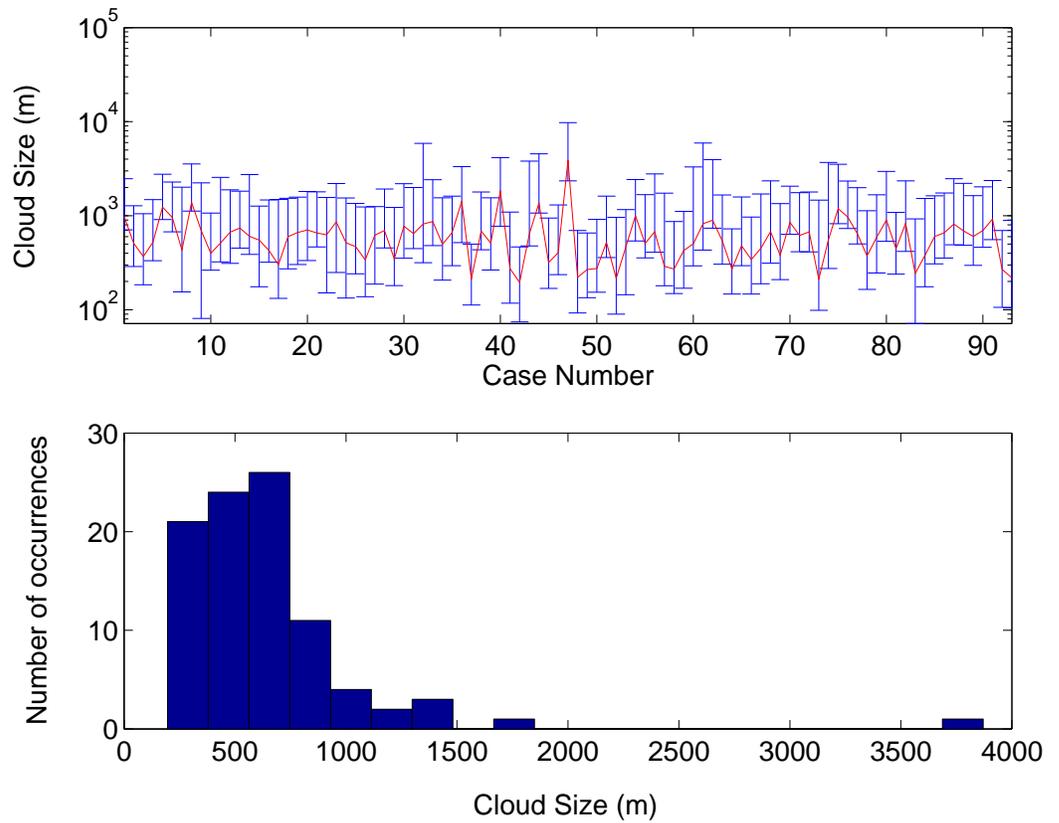
Fig. 5.17 The range of variation of the cloud horizontal sizes. The upper panel shows the range of variations of the cloud sizes; the lower panel is the histogram of the obtained cloud sizes. The red line in the upper panel represents the median values of the cloud size.
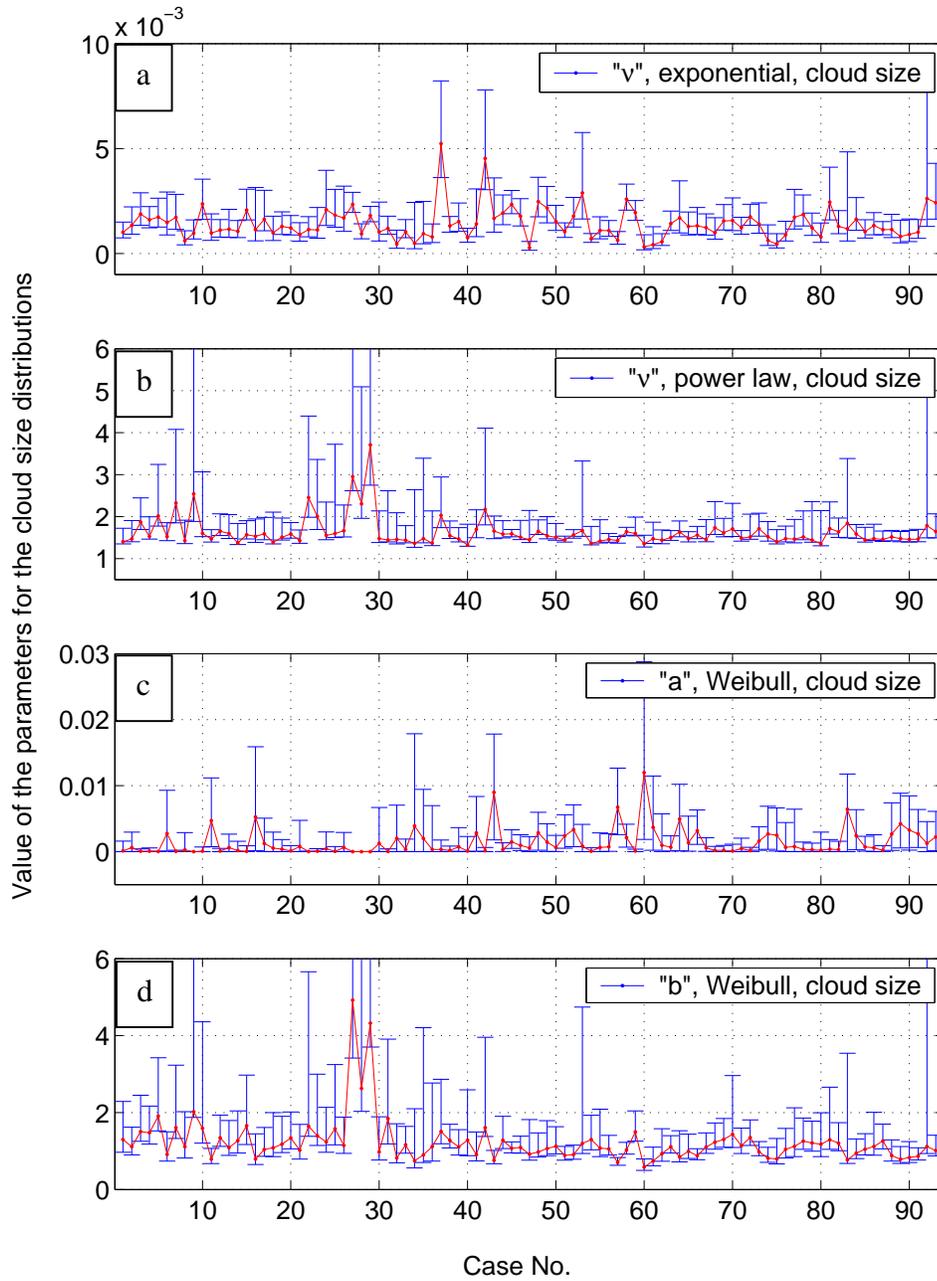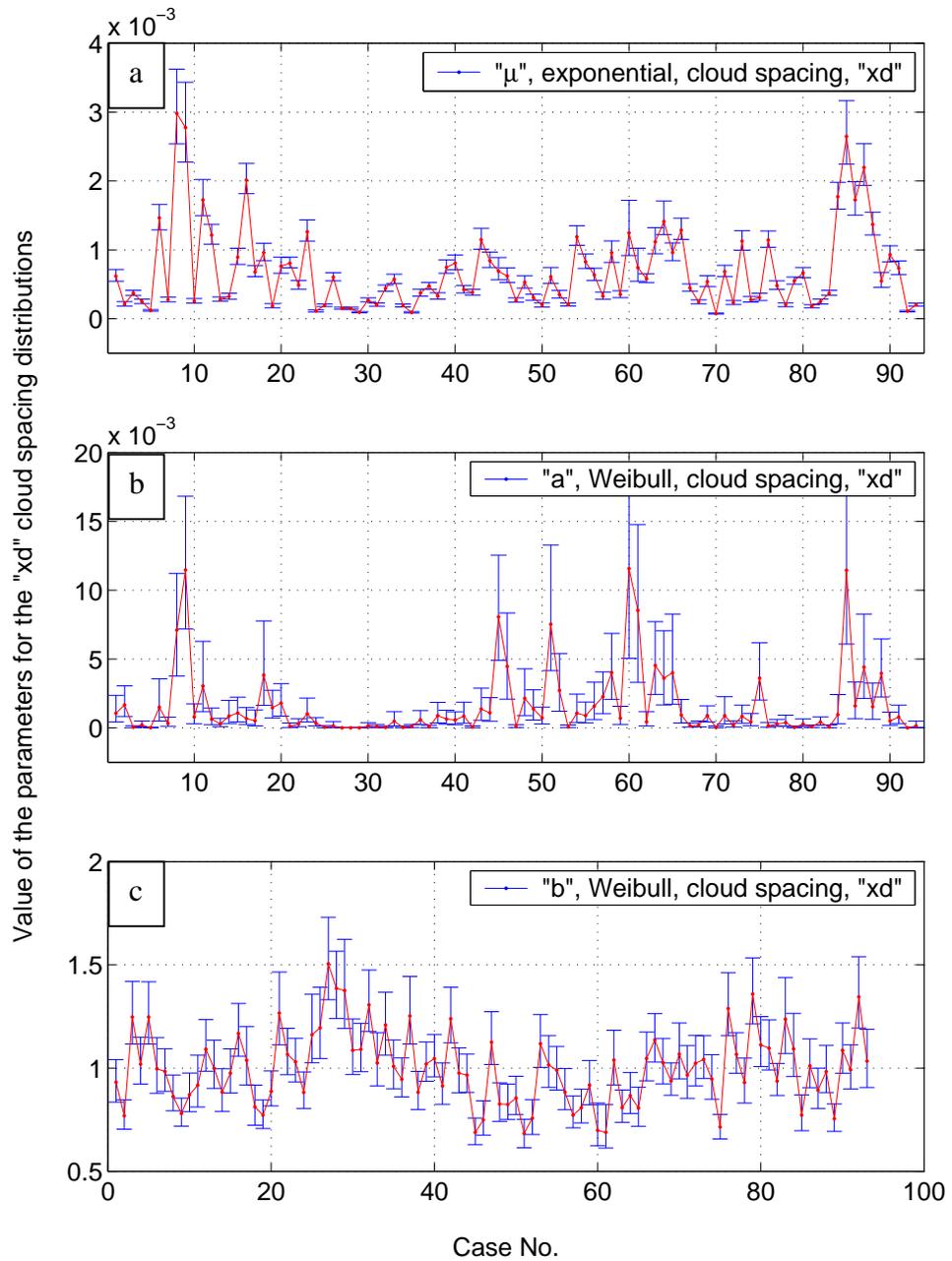
Fig. 5.18 Estimates of the cloud size distribution parameters.

(a) Parameter ν for the exponential distribution: $p(d) = \nu e^{-\nu d}$

(b) Parameter ν for the power law distribution: $p(d) = (\nu - 1)d_{min}^{\nu-1} d^{-\nu}$

(c) and (d) Parameters a and b, respectively, for the Weibull distribution: $p(d) = abd^{b-1}e^{-ad^b}$

where d denotes the cloud horizontal size.
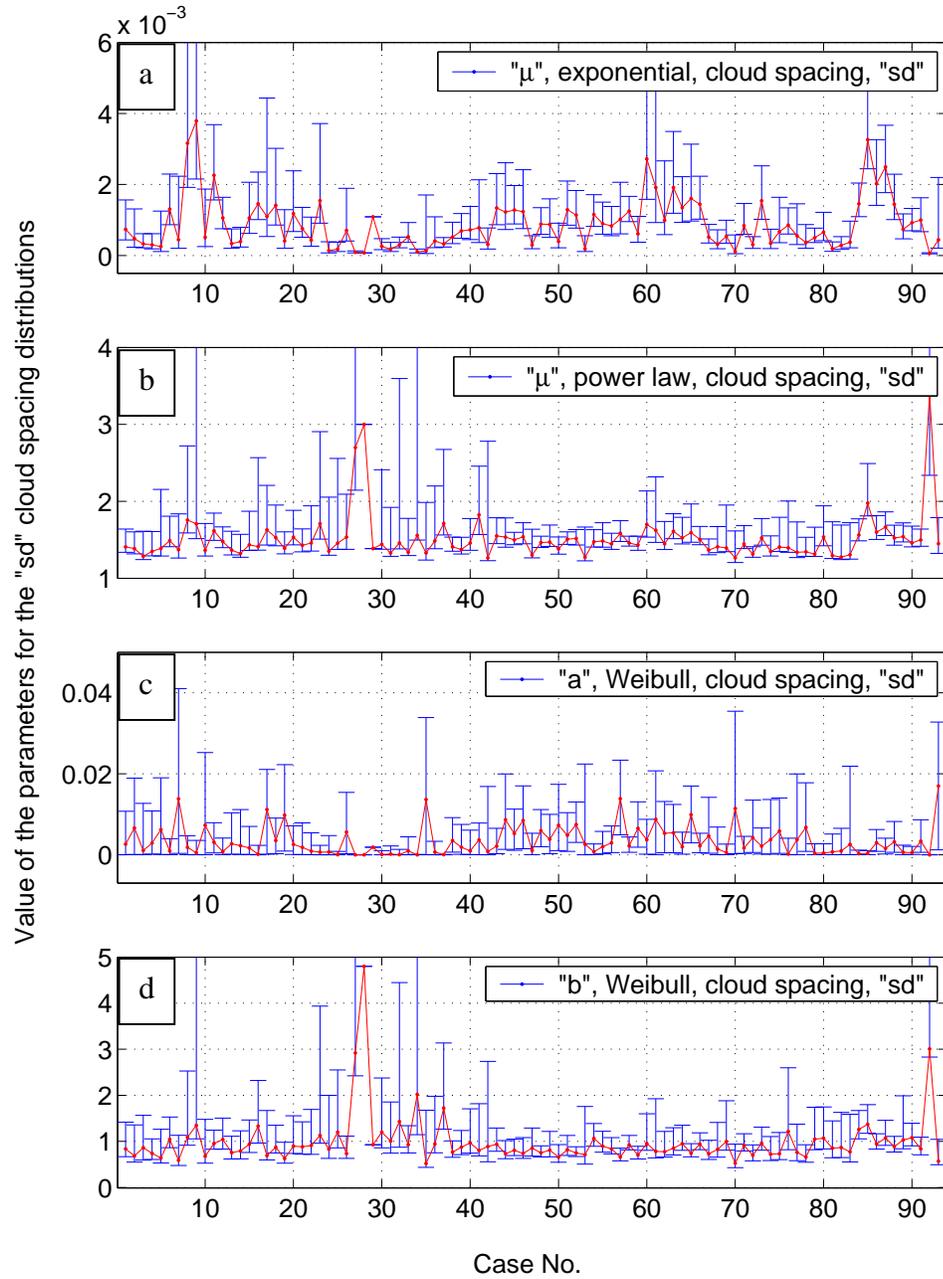
Fig. 5.19 Estimates of the cloud spacing distribution parameters for "sd" type.

(a) Parameter μ for the exponential distribution: $p(s) = \mu e^{-\mu s}$

(b) Parameter μ for the power law distribution: $p(s) = (\mu - 1)s_{\min}^{\mu-1} s^{-\mu}$

(c) and (d) Parameters a and b, respectively, for the Weibull distribution: $p(s) = abs^{b-1}e^{-as^b}$

where s denotes the cloud spacing of the "sd" type.
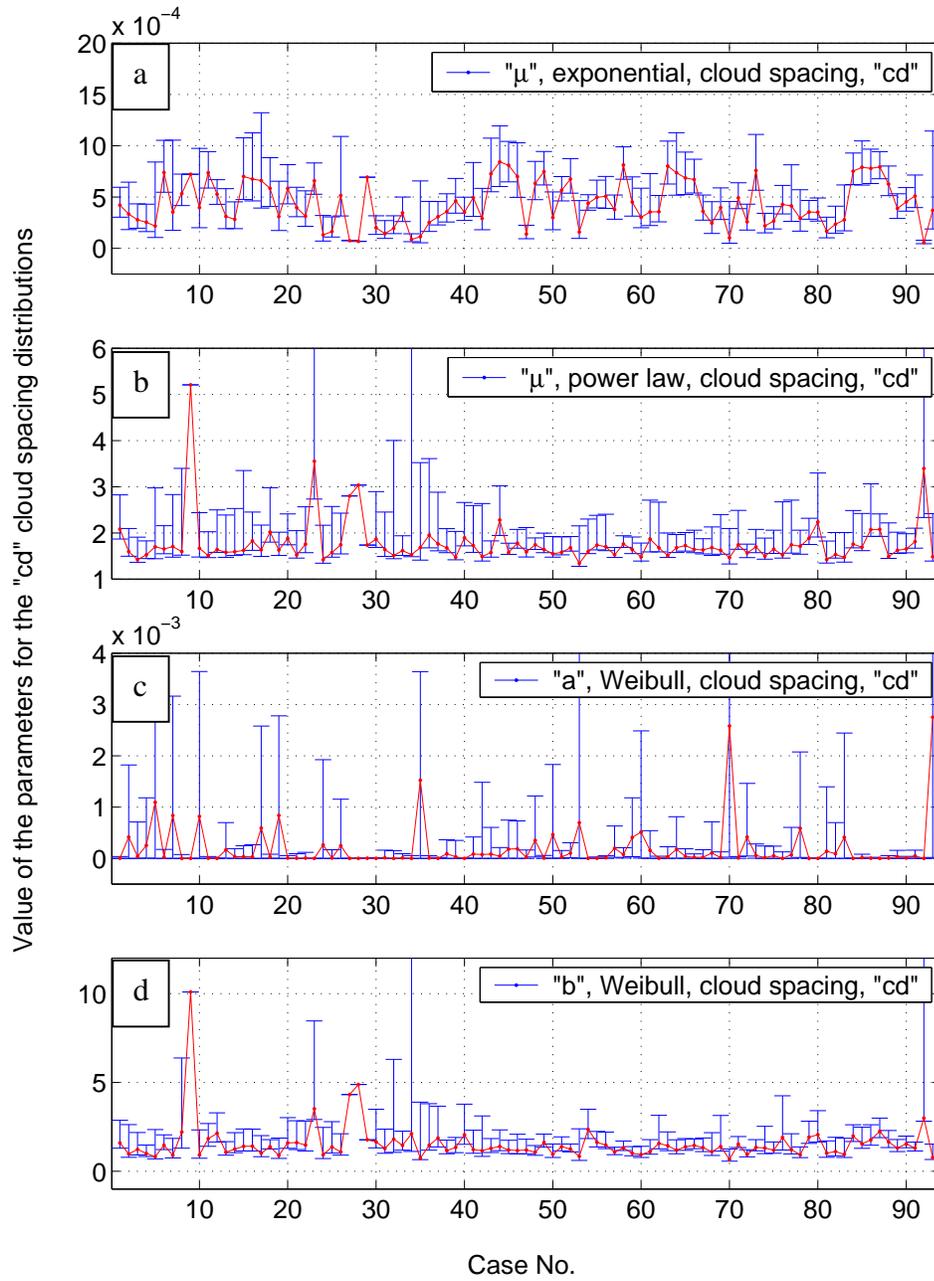
Fig. 5.20 Estimates of the cloud spacing distribution parameters for "cd" type.

(a) Parameter μ for the exponential distribution: $p(s) = \mu e^{-\mu s}$

(b) Parameter μ for the power law distribution: $p(s) = (\mu - 1)s_{min}^{\mu-1} s^{-\mu}$

(c) and (d) Parameters a and b, respectively, for the Weibull distribution: $p(s) = abs^{b-1}e^{-as^b}$

where s denotes the cloud spacing of the "cd" type.

Fig. 5.21 Estimates of the cloud spacing distribution parameters for the "xd" type.

(a) Parameter μ for the Exponential distribution: $p(x) = \mu e^{-\mu x}$

(b) and (c) Parameters *a* and *b*, respectively, for the Weibull distribution: $p(x) = abx^{b-1}e^{-ax^b}$

where *x* denotes the cloud spacing of the "xd" type.
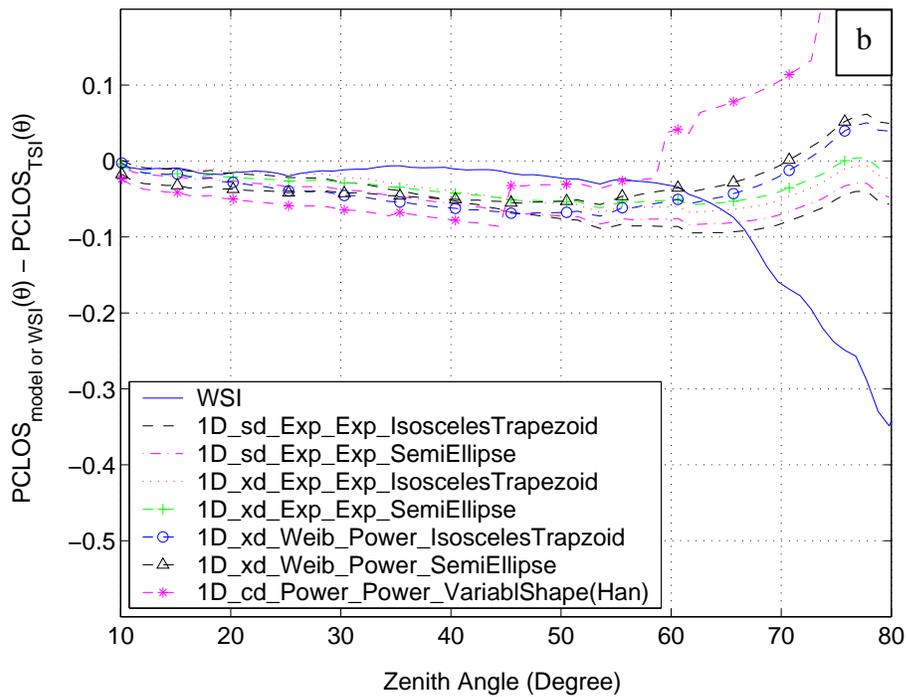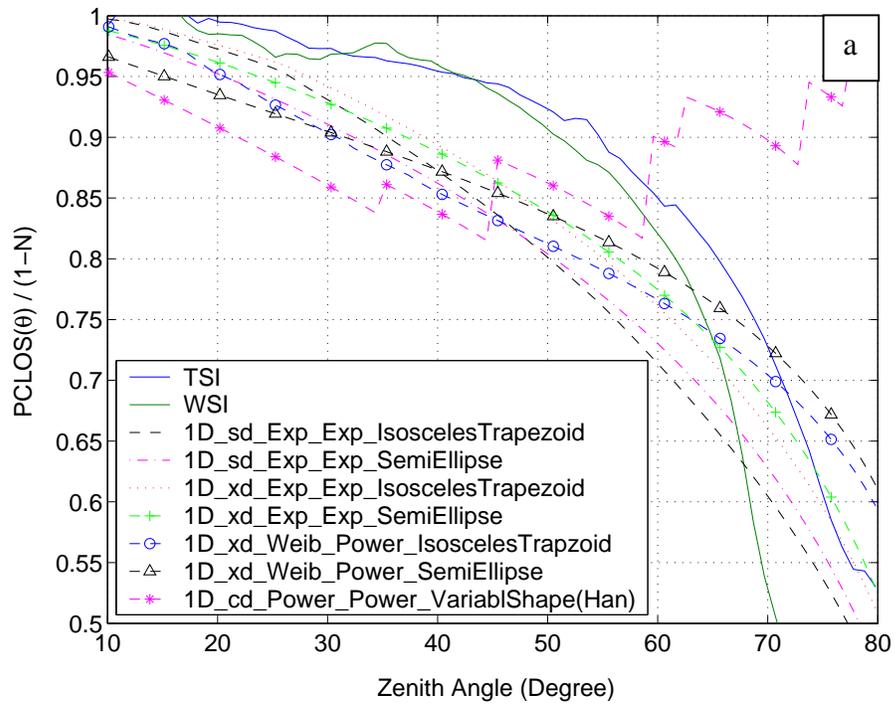
Fig. 5.22 (a) PCLOS$_{model}$/(1-N) compared with PCLOS$_{TSI}$/(1-N); (b) PCLOS$_{model}$ − PCLOS$_{TSI}$; for group-1 models. The results are the averages over 38 non-streak cases whose cloud thicknesses were confirmed with the relative humidity data.
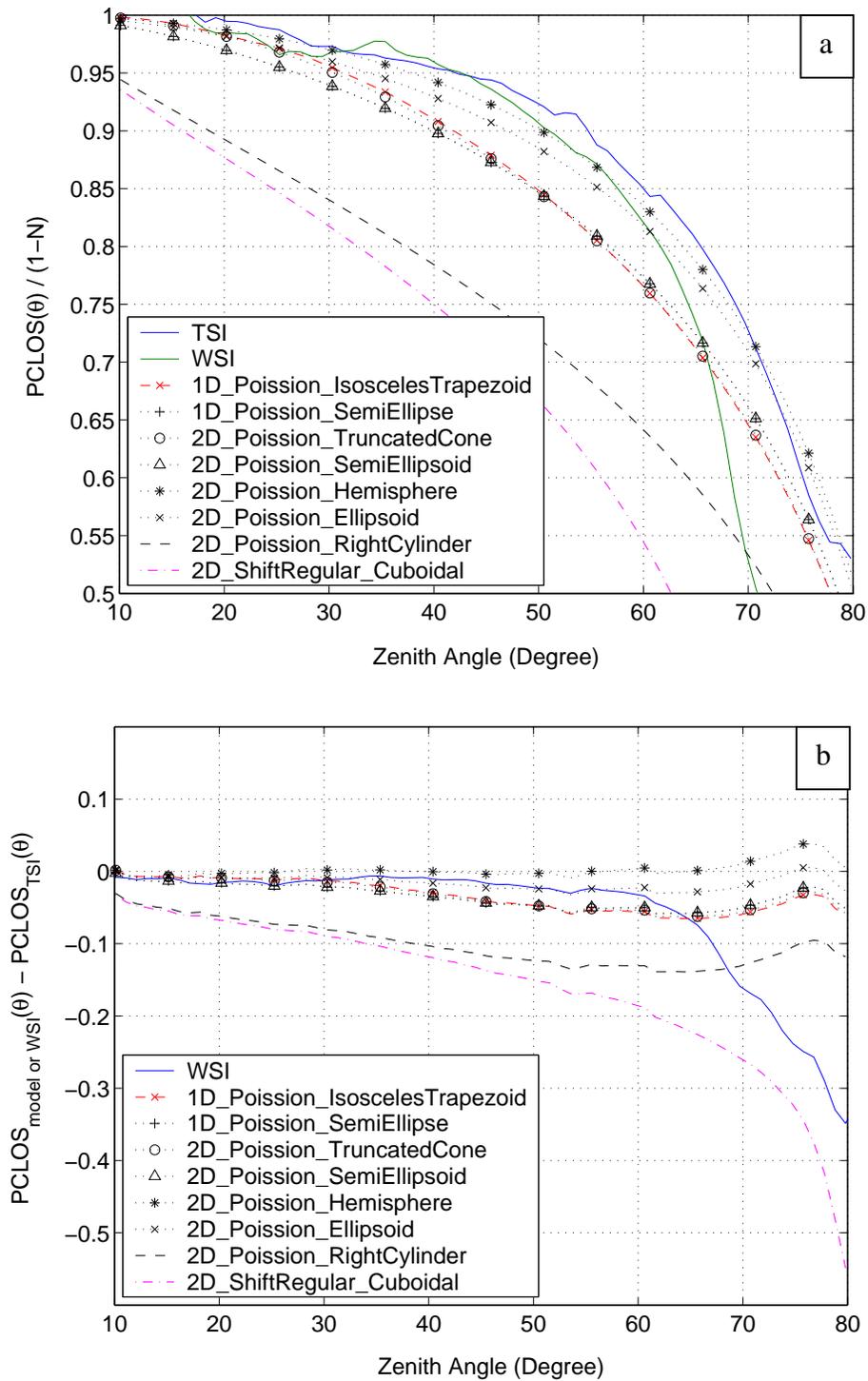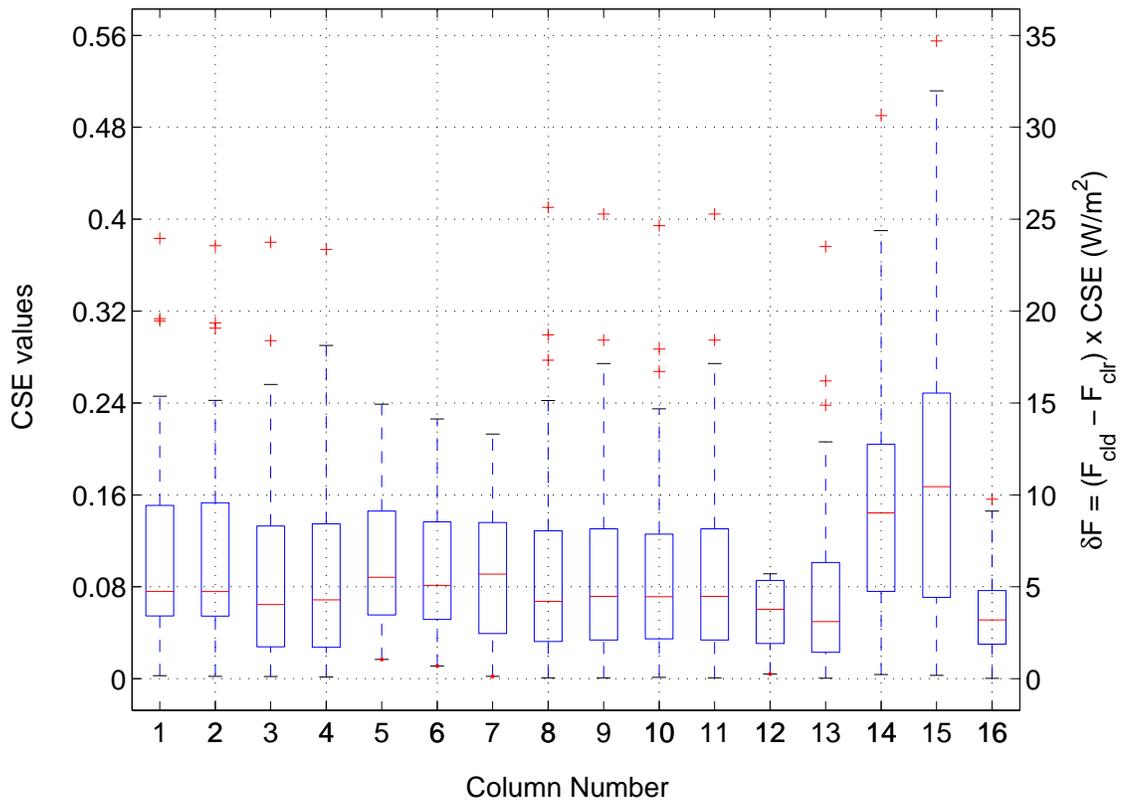
Fig. 5.23 (a) PCLOS$_{model}$/(1-*N*) compared with PCLOS$_{TSI}$/(1-*N*);
(b) PCLOS$_{model}$ - PCLOS$_{TSI}$; for group-2 models. The results are the
averages over 38 cases.
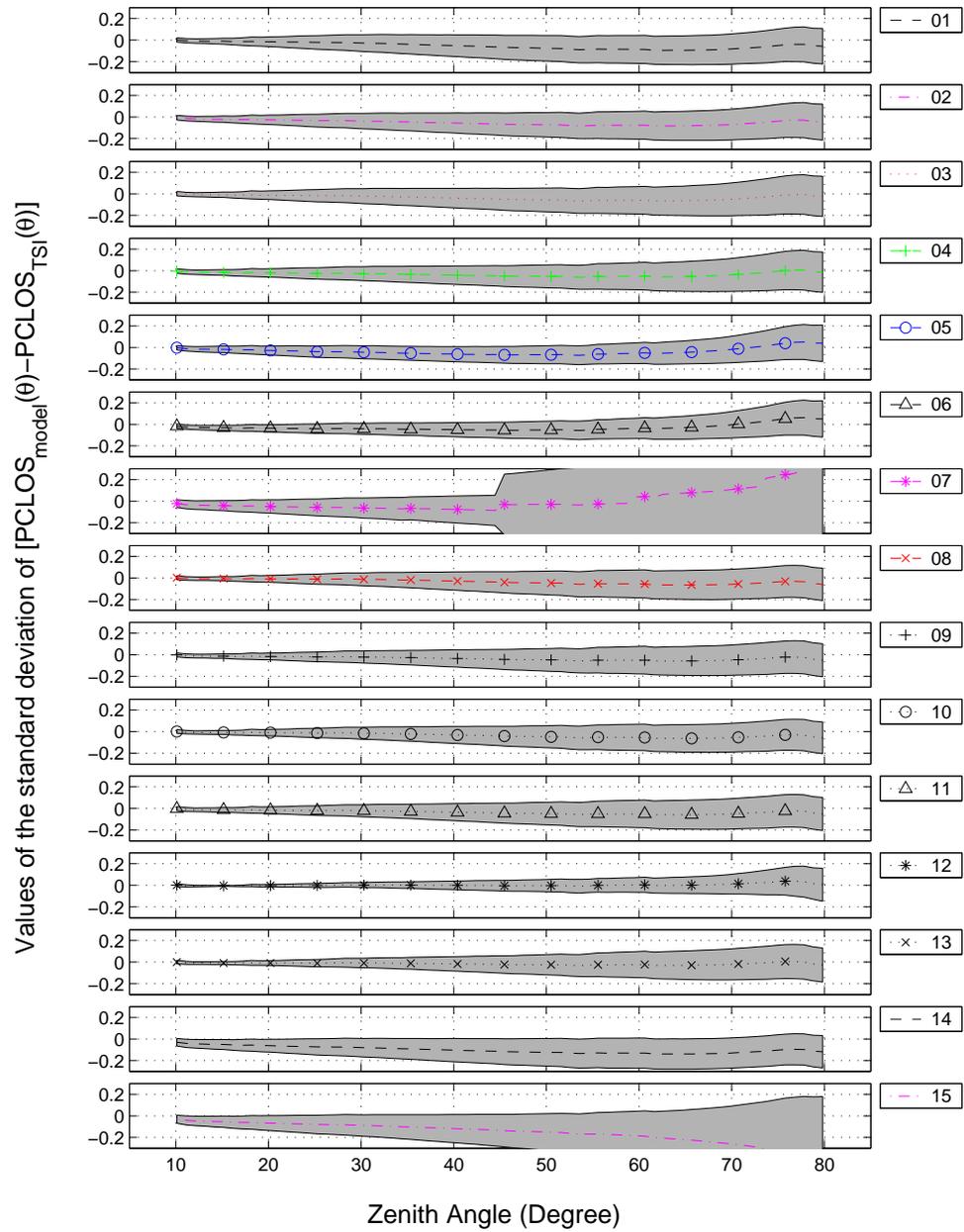
Fig. 5.24 Standard deviation of the difference between the models and the TSI observations as a function of zenith angle. The various panels are as follows:

1 1D_sd_Exp_Exp_IsoscelesTrapezoid
2 1D_sd_Exp_Exp_SemiEllipse
3 1D_xd_Exp_Exp_IsosecelesTrapezoid
4 1D_xd_Exp_Exp_SemiEllipse
5 1D_xd_Weib_Power_IsoscelesTrpezoid
6 1D_xd_Weib_Power_SemiEllipse
7 1D_cd_Power_Power_VariableShape(Han)

8 1D_Poisson_IsoscelesTrpezoid
9 1D_Poisson_SemiEllipse
10 2D_Poisson_TruncatedCone
11 2D_Poisson_SemiEllisoid
12 2D_Poisson_Hemisphere
13 2D_Poisson_Ellipsoid
14 2D_Poisson_RightCylinder
15 2D_ShiftRegular_Cuboidal

Fig. 5.25 Statistics of the model predictions of the *CSE* values and those inferred from the TSI observations. In the figure, the bottom and the top of the box indicated the 25th and 75th percentiles of the sample. The line in the middle of the box is the sample median. The plus sign in the figure is an indication of an outlier in the data. An outlier is a value that is more than 1.5 times the box length away from the top or bottom of the box. The last column in the figure is the *CSE* computed using the TSI observations.

1	1D_sd_Exp_Exp_IsoscelesTrapezoid	8	1D_Poisson_IsoscelesTrpezoid
2	1D_sd_Exp_Exp_SemiEllipse	9	1D_Poisson_SemiEllipse
3	1D_xd_Exp_Exp_IsosecelesTrapezoid	10	2D_Poisson_TruncatedCone
4	1D_xd_Exp_Exp_SemiEllipse	11	2D_Poisson_SemiEllisoid
5	1D_xd_Weib_Power_IsoscelesTrpezoid	12	2D_Poisson_Hemisphere
6	1D_xd_Weib_Power_SemiEllipse	13	2D_Poisson_Ellipsoid
7	1D_cd_Power_Power_VariableShape(Han)	14	2D_Poisson_RightCylinder
		15	2D_ShiftRegular_Cuboidal
		16	**TSI**
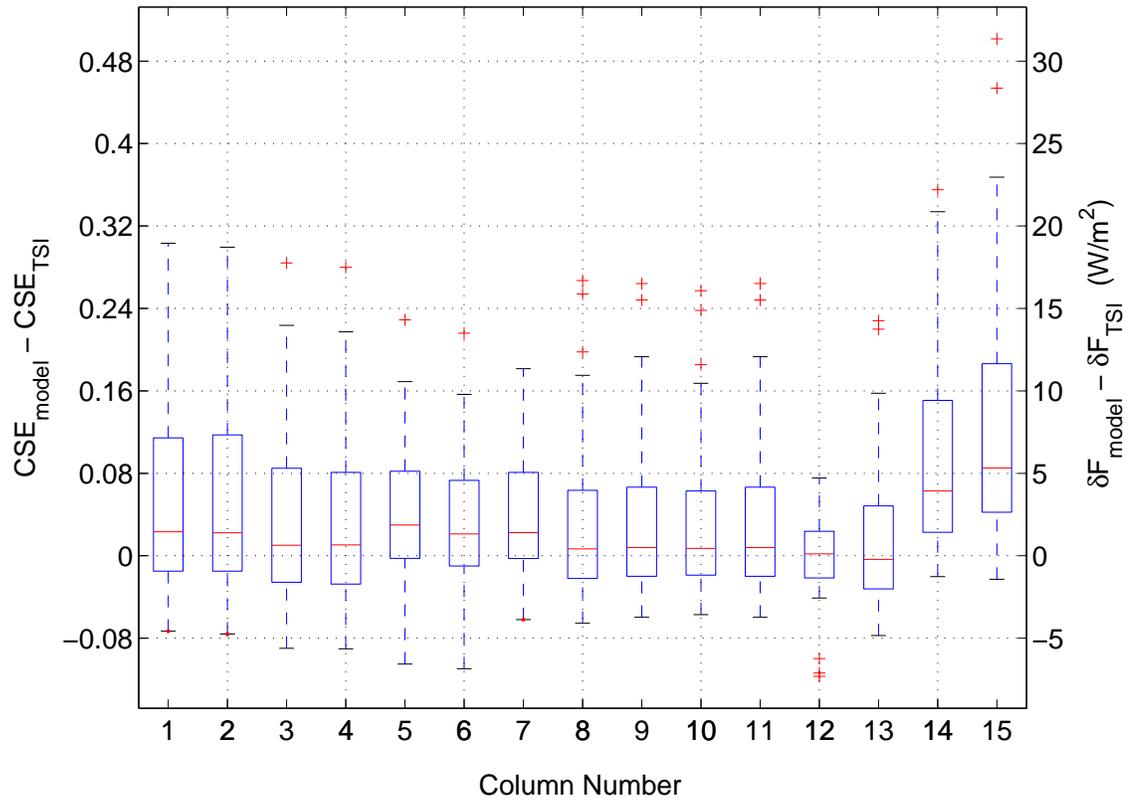
Fig. 5.26 Differences between the *CSE* values predicted by the models and those obtained from TSI. Box plot properties follow those in Fig 5.25. The individual boxes correspond as follows:

1   1D_sd_Exp_Exp_IsoscelesTrapezoid
2   1D_sd_Exp_Exp_SemiEllipse
3   1D_xd_Exp_Exp_IsosecelesTrapezoid
4   1D_xd_Exp_Exp_SemiEllipse
5   1D_xd_Weib_Power_IsoscelesTrpezoid
6   1D_xd_Weib_Power_SemiEllipse
7   1D_cd_Power_Power_VariableShape(Han)

8   1D_Poisson_IsoscelesTrpezoid
9   1D_Poisson_SemiEllipse
10   2D_Poisson_TruncatedCone
11   2D_Poisson_SemiEllisoid
12   2D_Poisson_Hemisphere
13   2D_Poisson_Ellipsoid
14   2D_Poisson_RightCylinder
15   2D_ShiftRegular_Cuboidal

References

Avaste, O.A., Yu. R. Mullamaa, Kh. Yu. Niylisk, and M. A. Sulev, 1974: On the coverage of the sky by clouds, in heat transfer in the atmosphere. NASA Tech. Transl., NASA TT-F-790, 173-181.

Barker, H. W., and B. A. Wielicki, 1997: Parameterizing grid-averaged longwave fluxes for inhomogeneous marine boundary layer clouds. *J. Atmos. Sci.*, **54**, 2785-2798.

Bell, T. L., P. K. Kundu, and C. D. Kummerow, 2001: Sampling errors of SSM/I and TRMM rainfall averages: Comparison with error estimates from surface data and a simple model. *J. Appl. Meteor.*, **40**, 938-954.

Cahalan, R. F., and J. H. Joseph, 1989: Fractal Statistics of cloud fields. *Mon. Wea. Rev.*, **117**, 261-272.

Cess , R.D., Potter, G.L., Blanchet, J.P., Boer, G.J., Del Genio, A.D., Déqué, M., Dymnikov, V., Galin, V., Gates, W.L., Ghan, S.J., Kiehl, J.T., Lacis, A.A., Le Treut, H., Li, Z.-X., Liang, X.-Z., McAvaney, B.J., Meleshko, V.P., Mitchell, J.F.B., Morcrette, J.-J., Randall, D.A., Rikus., L., Roeckner, E., Royer, J.F., Schlese, U., Sheinin, D.A., Slingo, A., Sokolov, A.P., Taylor, K.E., Washington, W.M., Wetherald, R.T., Yagai, I. & Zhang, M.-H.,1990. Intercomparison and interpretation of climate feedback processes in nineteen atmospheric general circulation models. *J. Geophys. Res.*, **95**, 16601-16615.

Clothiaux, E. E., M.A. Miller, R.C. Perez, D.D. Turner, K.P. Moran, B.E. Martner, T.P. Ackerman, G.G. Mace, R.T. Marchand, K.B. Widener, D.J. Rodriguez, T. Uttal, J.H. Mather, C.J. Flynn, K.L. Gaustad, and B. Ermold, 2001: The ARM Millimeter Wave Cloud Radars (MMCRs) and the Active Remote Sensing of Clouds (ARSCL) Value Added Product (VAP). U.S. Department of Energy, Tech. Memo. ARM VAP-002.1, 56 pp.

Cochran, W. G., 1977: *Sampling Techniques*. 3d ed. Wiley, 427 pp.

DeHoff, R. T. and F. N. Rhines, 1968: *Quantitative Microscopy*. McGraw-Hill, 422 pp.

Ellingson, R. G., and J. C. Gille, 1978: An infrared radiative transfer model. Part 1: Model description and comparison of observations with calculations. *J. Atmos. Sci.*, **35**, 523-545.

_____, 1982: On the effects of cumulus dimensions on longwave irradiance and heating rate calculations. *J. Atmos. Sci.*, **39**, 886-896.

Grabowski, W. W., X. Wu, M. W. Moncrieff, and W. D. Hall, 1998: Cloud resolving modeling of tropical cloud systems during Phase III of GATE. Part II: Effects of resolution and the third spatial dimension. *J. Atmos. Sci.*, **55**, 3264-3282.

Hahn, C. J., and S. G. Warren, 1999: Extended edited cloud reports from ships and land stations over the globe, 1952-1996. Numerical Data Package NDP-026C, Carbon Dioxide Information Analysis Center (CDIAC), Department of Energy, Oak Ridge, Tennessee, 79 pp.

Han, D., 1996: Studies of longwave radiative transfer under broken cloud conditions: Cloud parameterizations and validations. Ph.D. dissertation, University of Maryland at College Park, 163 pp.

_____, and R. G. Ellingson, 1999: Cumulus cloud formulations for longwave radiation calculations. *J. Atmos. Sci.*, **56**, 837-851.

_____, and _____, 2000: An experimental technique for testing the validity of cumulus cloud parameterization for longwave radiation calculations. *J. Appl. Meteor.*, **39**, 1147-1159.

Harshvandhan, 1982: The effect of brokenness on cloud-climate sensitivity. *J. Atmos. Sci.*, **39**, 1863-1861.

_____, and J. A. Weinman, 1982: Infrared radiative transfer through a regular array of cuboidal clouds. *J. Atmos. Sci.*, **39**, 431-439.

Heidinger, A. K., and S. K. Cox, 1996: Finite-cloud effects in longwave radiative transfer. *J. Atmos. Sci.*, **53**, 953-963.

Joseph, J. H., and R. F. Cahalan, 1990: Nearest neighbor spacing of fair weather cumulus clouds. *J. Appl. Meteor.*, **29**, 793-805.

Kagan, R. L, 1997: *Averaging of Meteorological Fields*. Translated from Russian. Ed. by L. S. Gandin and T. M. Smith. Kluwer Academic, 279 pp.

Kauth, R. J., and J. L. Penquite, 1967: The probability of clear lines of sight through a cloudy atmosphere. *J. Appl. Meteor.*, **6**, 1005-1017.

Killen, R., and R. G. Ellingson, 1994: The effect of shape and spatial distribution of cumulus clouds on longwave irradiance. *J. Atmos. Sci.*, **51**, 2123-2136.

Li, J., and H. W. Barker, 2002: Accounting for unresolved clouds in a 1D infrared radiative transfer model. Part II: horizontal variability of cloud water path. *J. Atmos. Sci.*, **59**, 3321-3339.

Lopez, R. E., 1977: The lognormal distribution of cumulus cloud population. *Mon. Wea. Rev.*, **105**, 865-872.

Lovejoy, S., 1982: Area-perimeter relation for rain and cloud areas. *Science*, **216**, 185-187.

Lund, I. A., and M. D. Shanklin, 1972: Photogrammetrically determined cloud free line-of-sight through the atmosphere. *J. Appl. Meteor.*, **11**, 773-782.

⎯⎯⎯⎯, and ⎯⎯⎯⎯, 1973: Universal methods for estimating probabilities for cloud free line-of-sight through the atmosphere. *J. Appl. Meteor.*, **12**, 28-35.

Masunaga, H., and T. Nakajima., 2001: The effective cloud fraction of broken clouds obtained by multistream radiative transfer. Part I: Longwave radiation. *J. Atmos. Sci.*, **58**, 2455-2467.

Matern, B., 1986: *Spatial Variation*. 2d ed. Spring-Verlag, 151pp.

Mathai, A. M., 1999: *An introduction to geometrical probability: distributional aspects with applications*. Gordon & Breach Science Pub., 554 pp.

Mattfeldt, T., 1989: The accuracy of one-dimensional systematic sampling. *J. Microscopy*, **153**, 301-313.

Naber, P. S., and J. A. Weinman, 1984: The angular distribution of infrared radiances emerging from broken fields of cumulus clouds. *J. Geophys. Res.*, **89**, 1249-1257.

Niylisk, 1972: Cloud Characteristics in problems of radiation energetic in the earth's atmosphere. *Izv. Acad. Sci. USSR, Atmos. Oceanic Phys.*, **8**, 270-281.

Plank, V. G., 1969: The size distribution of cumulus clouds in representative Florida populations. *J. Appl. Meteor.*, **8**, 46-67.

Ramanathan, V., R. D. Cess, E. F. Harrison, P. Minnis, B. R. Barkstrom, E. Ahmad, and D. Hartmann, 1989: Cloud-radiative forcing and climate: Results from the Earth Radiation Budget Experiment. *Science*, **243**, 57-63.

Rapp, R. R., C. Schutz, and E. Rodriguez, 1973: Cloud-free line-of-sight calculations. *J. Appl. Meteor.*, **12**, 484-493.

Sengupta, S. K., R. M. Welch, M. S. Navar, T. A. Berendes, and D. W. Chen, 1990: Cumulus cloud field morphology and spatial patterns derived from high spatial resolution Landsat imagery. *J. Appl. Meteor.*, **29**, 1245-1267.

Siebesma, A. P., and J. W. M. Cuijpers, 1995: Evaluation of parametric assumptions for shallow cumulus convection. *J. Atmos. Sci.*, **52**, 650-666.

Slingo, J. M., 1980: A cloud parameterization scheme derived from GATE data for use with a numerical model. *Quart. J. Roy. Meteor. Soc.*, **106**, 747-770.

_____, 1987: The development and verification of a cloud prediction scheme for ECMWF model. *Quart. J. Roy. Meteor. Soc.*, **113**, 899-927.

Stokes, G. M., and S. E. Schwartz, 1994: The Atmosphere Radiation Measurement (ARM) program: Programmatic background and design of the cloud and radiation test bed. *Bull. Amer. Meteor. Soc.*, **75**, 1201-1221.

Stoyan, D., Kendall, W. S., and J. Mecke, 1987: *Stochastic Geometry and its Applications*. Wiley, 436 pp.

Takara, E. E., and R. G. Ellingson, 1996: Scattering effects on longwave fluxes in broken cloud fields. *J. Atmos. Sci.*, **53**, 1464-1476.

_____, and _____, 2000: Broken cloud field longwave-scattering effects. *J. Atmos. Sci.*, **57**, 1298-1310.

Taylor, G. I., 1922: Diffusion by continuous movement. *Proc. London Math. Soc. (2)*, **20**, 196-212.

Vanmarke, E., 1983: *Random Fields: Analysis and Synthesis*. The MIT Press, 382 pp.

Weibel, E. R., 1979: *Practical Methods for Biological Morphometry*. Vol. 1, *Stereological Methods*. Academic Press, 415 pp.

Yu, S., K. E. Case, J. Chernick, 1986: Methodologies and comparisons for Lund's two methods for calculating probability of cloud-free line-of-sight. *J. Climate and Appl. Meteor.*, **25**, 389-397.

Zhu, T., J. Lee, R. C. Weger, and R. M. Welch, 1992: Clustering, Randomness and Regularity in Cloud Fields: 2. Cumulus Cloud Fields. *J. Geophys. Res.*, **97**, 20537-20558.